Institut für Ionenstrahlphysik und Materialforschung

Helmholtz-Zentrum Dresden-Rossendorf

Optoelectronic applications of heavily doped GaAs and MoSe$_2$/FePS$_3$ heterostructures

Dissertation

zur Erlangung des akademischen Grades
Doctor rerum naturalium (Dr. rer. nat.)

vorgelegt der Fakultät Mathematik und Naturwissenschaften
der Technischen Universität Dresden

von

Juanmei Duan

geboren am 21.02.1992 in China

Eingereicht am 04. 08. 2021
Verteidigt am 14. 01. 2022

Gutachter:

1. Prof. Dr. Manfred Helm (TU-Dresden and HZDR)
2. Prof. Dr. Dietrich R. T. Zahn (TU-Chemnitz)

Abstract

Optoelectronics is quickly becoming a fast emerging technology field. It refers to detect or emit electromagnetic radiation, and convert it into a form that can be read by an integrated measuring device. These devices can be a part of many applications like photodiodes, solar cells, light emitting diode (LED), telecommunications, medical equipment, and more. Due to their different applications, the semiconductor optoelectronic devices can be divided by their operating wavelength and working mechanisms.

In this work, I have focused on semiconductor plasmonic systems operating in the mid-infrared and on the optical detectors made of 2D materials operating in the UV-visible spectral range. Mid-infrared plasmonic devices are very attractive for chemical sensing. Our results show that ultra-doped n-type GaAs is ideal for mid-infrared plasmonics, where the plasmon wavelength is controlled by electron concentration and can be as short as 4 μm. Ultra-doped n-type GaAs is achieved using ion implantation of chalcogenides like S and Te followed by nonequillibrium thermal annealing, namely ns-range pulsed laser melting or ms-range flash lamp annealing. I have shown that the maximum electron concentration in our GaAs layer can be as high as 7×10^{19} cm^{-3}, which is a few times higher than that obtained by alternative techniques. In addition to plasmonic applications, the ultra-doped n-type GaAs shows negative magnetoresistance, making GaAs potential material for quantum devices and spintronic applications.

UV-visible optical detectors are made of 2D materials based on van der Waals heterostructures, i.e. transition metal dichalcogenides (TMDCs) e.g. MoSe$_2$ and transition metal chalcogenophosphates (TMCPs) with a general formula MPX$_3$ where M=Fe, Ni, Mn and X=S, Se, Te. The external quantum efficiency of a self-driven broadband photodetector made of a few layers of MoSe$_2$/FePS$_3$ van der Waals heterojunctions is as high as 12 % at 532 nm. Moreover, it is shown that multilayer MoSe$_2$ on FePS$_3$ forms a type-II band alignment, while monolayer MoSe$_2$ on FePS$_3$ forms a type-I heterojunction. Due to the type-I band alignment, the PL emission from the monolayer MoSe$_2$ is strongly enhanced.

Zusammenfassung

Zügig entwickelte sich die Optoelektronik zu einem rasant wachsenden Technologiesektor. In der Optoelektronik werden elektromagnetische Strahlungen ausgesendet oder detektieren und in eine von integrierten Messgeräten lesbare Form umgewandelt. Solche Bauteile sind unteranderem der essenziellen Bestandteile von vielen Anwendungen im Bereich der Telekommunikation, der medizinischen Gerätetechnik, Fotodioden, Solarzellen oder Leuchtdioden (LED). Aufgrund ihrer vielfältigen Anwendungsgebiete können die optoelektronischen Halbleiterbauelemente anhand ihrer Betriebswellenlänge oder ihren Arbeitsmechanismen unterteilt werden.

Diese Arbeit konzentriert sich auf plasmonische Halbleitersysteme im mittleren Infrarot-Spektralbereich und auf 2D-Materialien basierende optische Detektoren, die im UV-und sichtbaren Spektralbereich arbeiten. Plasmonische Bauteile, die mittleren Infrarot Bereich arbeiten, sind für die chemische Sensorik sehr attraktiv. Die nachfolgenden Ergebnisse zeigen, dass extrem hoch dotiertes (ultra-dotiertes) n-Typ GaAs sehr gut für die Mittelinfrarot-Plasmonik geeignet ist, weil die Plasmonen-Wellenlänge durch die Elektronenkonzentration gesteuert werden kann. Damit ist es möglich Wellenlängen im Bereich von 4 µm zu erreichen. Ultra-dotiertes n-Typ-GaAs wird durch Ionenimplantation von Chalkogen-Elementen wie S oder Te und einer nachfolgenden Nichtgleichgewichts-Wärmebehandlung, wie Pulslaserschmelzen im ns-Bereich oder Blitzlampentemperung im ms-Bereichs, erreicht. Es wurde gezeigt, dass die maximale Elektronenkonzentration der ultra-dotierten GaAs-Schicht bis zu $7 \times 10^{19} \, \mathrm{cm}^{-3}$ betragen kann. Dies liegt deutlich über den erreichbaren Elektronenkonzentrationen bei konventionellen Wärmebehandlungsmethoden wie Ofenglühen. Zusätzlich zu den plasmonischen Anwendungen zeigt das ultra-dotierte n-Typ GaAs einen negativen Magnetowiderstand, was GaAs zu einem potentiellen Material für Quantenbauelemente und spintronische Anwendungen macht.

UV-visuelle optische Detektoren werden aus 2D-Materialien, die auf Van-der-Waals-Heterostrukturen basieren, hergestellt. 2D-Materialien bestehen aus Übergangsmetall-Dichalkogeniden (TMDCs), wie zum Beispiel $MoSe_2$, und Übergangsmetall-Chalcogenophosphaten (TMCPs) mit der allgemeinen Formel MPX_3, wobei M für Fe, Ni oder Mn und X für S, Se oder Te stehen. Die externe Quanteneffizienz eines selbstgesteuerten Breitband-Photodetektors aus wenigen $MoSe_2/FePS_3$ Schichten mit Van-der-Waals-Heteroübergängen beträgt bis zu 12 % bei 532 nm. Außerdem wird gezeigt, dass mehrschichtiges $MoSe_2$ auf $FePS_3$ eine Typ-II-Bandausrichtung ausbildet, während sich bei einem einlagigen $MoSe_2$ auf $FePS_3$ ein Typ-I-Heteroübergang ausbildet. Aufgrund der Typ-I-Bandausrichtung ist die PL-Emission von der Monoschicht $MoSe_2$ stark erhöht.

Contents

Chapter 1 Introduction

1.1 Motivation

Light detection in the spectral range from UV to infrared has important applications, e.g. spectroscopic biosensing, infrared thermal imaging, photodetector, etc. For spectroscopic sensing, molecular vibrations in the mid-infrared enable the identification of biomolecules. Gases and biomolecules can be detected via their characteristic absorption spectra. Photoemissive metal-semiconductor hot-electron photodetectors, whose metal electrodes are shaped as metallic nanoantennas, have recently attracted interest in the context of plasmon-enhanced photodetection. In metallic nanoparticles, collective electronic oscillations, so-called particle plasmons, can be excited by light and are detectable as a pronounced optical resonance. At the resonance wavelength, the metallic nanoparticle acts as an antenna for light, with a strong near-field enhancement of electric fields in the vicinity of the nanoparticle surface. Incident light with the resonance frequency of the metallic nanoantennas can excite particle plasmons and the resulting local field enhancement can also serve to boost the internal photoemission if the metallic nanoantenna is placed on the top of a semiconductor. Since the probability of photon absorption is proportional to the square of the amplitude of the local electric field, the enhancement of the electric fields at the metal-semiconductor interface leads to an increase in the hot carrier generation (plasmon-induced hot electrons) and, consequently to an improvement in the photodetection performance.

In this work, we propose the use of plasmonic resonances in highly doped GaAs to enhance the light absorption. The advantage of using GaAs compared to noble metals for the plasmonic application is that, i) the carrier concentration in GaAs suitable for mid-infrared operation is several orders of magnitude lower than in metals; ii) the high quality of the material; iii) the advanced manufacturing technology. Moreover, compared to other group IV semiconductors, e.g. Si or Ge, GaAs has a higher electron mobility, which means lower plasmonic losses. Those superior features make GaAs an excellent candidate for mid-infrared plasmonic applications. However, the key challenge of this project is to achieve ultra-high doping levels in GaAs. It has already been shown that the maximum electron concentration in GaAs is of the order of 10^{19} cm^{-3} for both in-situ doped samples grown by molecular beam epitaxy and ex-situ doped samples followed by conventional thermal annealing. In order to overcome the doping limit in III-V compound semiconductors, we propose to use ion implantation of chalcogenides for n-type doping or Zn for p-type doping followed by sub-second annealing, namely ms-range flash

lamp annealing or ns-range pulsed laser annealing. By applying the proposed procedure, the hyperdoped GaAs with carrier concentration up to 7×10^{19} cm^{-3} can be fabricated.

The continuous scaling down in nanoelectronics has pushed the technology to its limits and inspired scientist to develop a new class of materials consisting of one or a few atomic layers. The great success of graphene has motivated the development of other 2D materials. Transition metal dichalcogenides (TMDCs) are one of these versatile materials due to their interesting properties, e.g. the existence of neutral and charged excitons, spin-valley coupling [1], and transitions from indirect-to-direct bandgap when reducing the thickness to a single monolayer [2-4]. Those exceptional features make them attractive candidates for applications in next generation nanoelectronics, photonics, and optoelectronics. In addition, van der Waals heterostructures (vdWHs) with atomically sharp and near-defect-free interfaces exhibit novel physics and possess versatile properties [5-7]. TMDCs based vdWHs have excellent optoelectronic properties and can be used, for example, in solar cells [8], light emitting diodes [9], and photodetectors [10]. Inspired by this, I have investigated the optoelectronic properties of MoSe$_2$ and FePS$_3$ which are naturally n- and p-type semiconductors, respectively. MoSe$_2$ exhibits efficient valley polarization when excited with circularly polarized light, while FePS$_3$ is an antiferromagnetic wide-band gap semiconductor. Taking into account the unique properties of both 2D materials, it is expected that heterostructures made of MoSe$_2$ and FePS$_3$ may reveal previously unknown phenomena in the field of optoelectronics.

1.2 Organization of this thesis

This dissertation presents optical and optoelectronic studies of heavily doped GaAs and the van der Waals heterostructure MoSe$_2$/FePS$_3$. The thesis is organized as follows:

In Chapter 2, I give a brief introduction on heavily doped GaAs: why GaAs is attractive for mid-infrared plasmonics and why it is difficult to achieve high doping level in GaAs; the feasibility of using ion implantation followed by subsecond annealing to prepare heavily doped GaAs; and the effects of high doping in GaAs. In addition, a general introduction about the optical and electrical properties of transition metal dichalcogenides and metal phosphorus trisulfide is given.

In chapter 3, sample fabrication techniques and characteristic setups, i.e. ion implantation, flash lamp, pulsed laser annealing and the theory about Hall effect are presented. Moreover, the preparation processes for the fabrication of the van der Waals heterostructures for optoelectrical study are also given.

Chapter 4 presents the optoelectronic and magneto-transport properties of hyperdoped GaAs. The samples are fabricated by Zn, S or Te implantation followed by sub-second flash lamp annealing. The electron concentration in implanted and annealed GaAs is as high as 5×10^{19} cm^{-3}, while the hole concentration in Zn doped GaAs is as high as 1×10^{20} cm^{-3}. The plasma frequency of GaAs can be tuned from 1400 and 2700 cm^{-1} by increasing the carrier concentration from 7×10^{18} to 7×10^{19}. In addition, n^{++}-GaAs exhibits negative magnetoresistance up to 80 K, which is attributed to the weak localization suppressed by the magnetic field. It is found that at low temperature, the phase coherence length increases with increasing carrier concentration and it is as large as 540 nm at 3 K.

In chapter 5, the fabrication of MoSe$_2$/FePS$_3$ van der Waals heterostructures is presented. Using the mechanical exfoliation process, monolayer or bilayer MoSe$_2$ is transferred on top of FePS$_3$. The fabricated heterojunctions show type-I band alignment, which was verified by photoluminescence (PL) measurements. At room temperature, PL shows 20-fold enhancement of the emission from the MoSe$_2$ monolayer in MoSe$_2$/FePS$_3$ van der Waals heterostructures (vdWH), which is due to the carrier injection from p-type FePS$_3$ to n-type MoSe$_2$. Furthermore, at low temperatures the intensity ratio between trion and exciton emission increases from 0.44 to about 20. In addition, the heterojunctions exhibit polarization of the trion emission, which makes them attractive for valleytronics.

Chapter 6 presents the fabrication process and characterization of a broadband photodetector made of multilayer MoSe$_2$/FePS$_3$. The operation range of the photodetector ranges from 350 to 900 nm. In contrast to monolayer MoSe$_2$ on FePS$_3$, heterojunctions made of thicker flakes show type-II band alignment. The presented photodetector, operating at zero bias and at room temperature under ambient conditions, exhibits the maximum responsivity (R_{max}) of 52 mA W^{-1} and an external quantum efficiency (EQE$_{max}$) of 12% at 522 nm, which are better than the characteristics of its individual constituents and many other photodetectors made of 2D heterostructures.

Chapter 7 summarizes the thesis and an outlook for future work on heavily doped GaAs and MoSe$_2$/FePS$_3$ heterostructures is given.

Chapter 2 Fundamentals

2.1 Heavily doped GaAs

2.1.1 GaAs aiming for infrared Plasmonics

Plasmonics exploits a new field in photonics, whereby the features of photonics and electronics are combined by coupling the energy and momentum of a photon to a free electron gas in the form of surface plasmons [11]. It manifests a resonance between photons and electrons, which enables light coupling with collective oscillations of free carriers in the subwavelength structure and overcome the diffraction limit of light. Fig. 2-1 shows two classical examples of coupling between photons and electron plasma: (a) localized surface plasmon resonances (LSPR) in metallic nanostructures (usually Ag or Au nanoparticles) with the size of the particle comparable to or smaller than the wavelength of incident light. In resonance, the electron cloud in a metallic nanoparticle oscillates under the forces of the electric field generated by incident light and the restoring force arising from the Columbic attraction between electrons and nuclei. This introduces two important effects: i) a significant enhancement of the electric fields near the particle's surface; ii) the maximum optical absorption at the plasmon resonant frequency for metallic nanoparticles. Note that the oscillation frequency can be tuned by the change of the electron density, the effective electron mass, size and shape of the charge distribution [12]. Fig. 2-1(b) shows surface plasmon polaritons (SPPs) propagating along dielectric/metal interfaces. The surface plasmon propagates back and forth between the ends of the structure, which is of great interest for plasmonic waveguides and nanoscale light sources [13, 14]. Moreover, due to this increased light-matter interaction, it provides a constructive platform for biosensing [15, 16], surface enhanced spectroscopy [17-19], immunoassays [20], and subwavelength imaging [21].
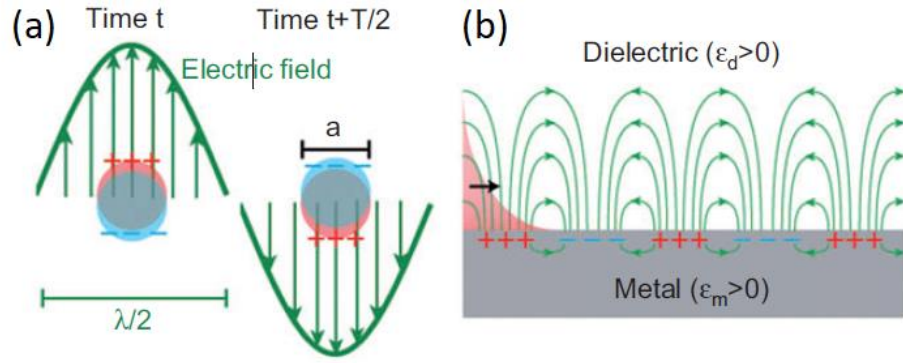
Fig. 2-1. (a) and **(b)** schematics of localized surface plasmon resonance (LSPR) and surface plasmon polariton (SPPs) modes at the metal/dielectric interfaces. From ref. [22].

Metals like Ag and Au are the most commonly used materials in plasmonics and optical metamaterial devices because of their small ohmic losses or high DC conductivity [23]. Fig. 2-2 shows commonly used plasmonic materials from the UV to infrared spectral range. Their plasmonic properties can be affected by carrier concentration, carrier mobility and interband losses in the samples. Note that the spherical bubbles in this figure represent materials with low interband losses, and the elliptical bubbles represent those with larger interband losses in their working electromagnetic spectrum. This clearly indicates that the carrier concentration in the target sample determines the resonant frequencies of the plasmons.

The plasmon theory is briefly introduced here. The interaction between free-electron and photons can be understood in terms of classical coupled harmonic oscillators [22, 24, 25]. The plasmon with one dimension movement can be considered as a driven damped harmonic oscillator, which can described as [22]:

$$m\frac{d^2x}{dt^2} + m\gamma\frac{dx}{dt} = eE_0\exp(-i\omega t) \qquad (2-1)$$

where m is the mass of particle, x is the effective movement of particle, γ is the scattering rate for electrons, ω is the angular frequency of the incident periodic optical field, E_0 is the amplitude of the electric field of the light. Assuming that the deflection of the electron from its equilibrium position can be written in the form $x(t) = Aexp(-i\omega t)$, the amplitude of the electron's oscillation is given by $A = -\frac{e}{m}\frac{1}{\omega^2+i\gamma\omega}$. The polarization can be calculated as $P = enx = \varepsilon_0\chi E$ with n being the density of the free-electron gas, ε_0 is the permittivity of free space and χ is the polarizability. Then the relative permittivity of the plasmonic material ε_m is given by:

$$\varepsilon_m = \varepsilon_b + \chi = \varepsilon_b - \frac{\omega_p^2}{\omega(\omega + i\gamma)} \qquad\qquad (2-2)$$

with the plasma frequency $\omega_p^2 = \frac{\varepsilon^2 n}{\varepsilon_0 m}$, ε_b is the materials background permittivity. Since $\sqrt{\omega_p} \propto n$, the noble metals with the carrier concentration in the order of 10^{22} cm^{-3} have the pronounced plasmonic properties in visible range. However, extending the LSPR to infrared (IR) becomes a challenge. That is because the permittivity of most noble metals at IR become extremely large, and the large imaginary permittivity means a strong extinction coefficient. It results in weak, nonresonant scattering from the metal nanoparticle, preventing strong field enhancement or subwavelength localization [19]. Sensors operated in IR made of such metallic nanoparticles will have low sensitivity. Thus, the discovery of suitable plasmonic materials with low-losses and low magnitude of negative real part of permittivity in the IR region is required. Transparent conducting oxides (TCO) such as indium tin oxide, zinc oxide doped with aluminum or gallium with carrier concentrations below10^{20} to 10^{21} cm^{-3} are favorable materials to operate in near-IR range [26].

Moreover, the applications in the mid-IR wavelength range is attracting immense attentions of research groups and industries due to potential applications in thermal detection, imaging applications and sensors for explosive gases. Since a large number of molecules with fundamental vibrational absorption resonances or named 'molecular fingerprint' is in the mid-IR range [22], mid-IR plasmonics is of great interest for the molecular sensor applications. Plasmonics can greatly facilitate the enhancement coupling between long wavelength light and molecular species. This can improve the efficiency and responsivity of these devices and aim for the miniaturization of devices. Heavily doped semiconductors such as silicon, germanium, and III-V compounds are very promising as low-losses plasmonic materials in the mid-IR range (Fig. 2-2). These semiconductors can be tuned from dielectric to metallic by increasing the dopant concentration up to several orders of magnitude. In addition, they also have other advantages, such as high material quality and mature manufacturing technology, which opens up exciting possibilities for novel device concepts. Ginn *et al.* predicted the existence of plasmons at 6 μm in Si with a doping level of 10^{20} cm^{-3}, which is a 10 times longer wavelength than that of Au at long-IR [27]. Baldassarre *et al.* demonstrated that heavily doped germanium with a doping level of 2.3 ×10^{19} cm^{-3} sustains plasmons at 13 μm [28]. Moreover, the fabricated Ge based nanoantennas show a significant spectral signal enhancement for a polymer thin film.
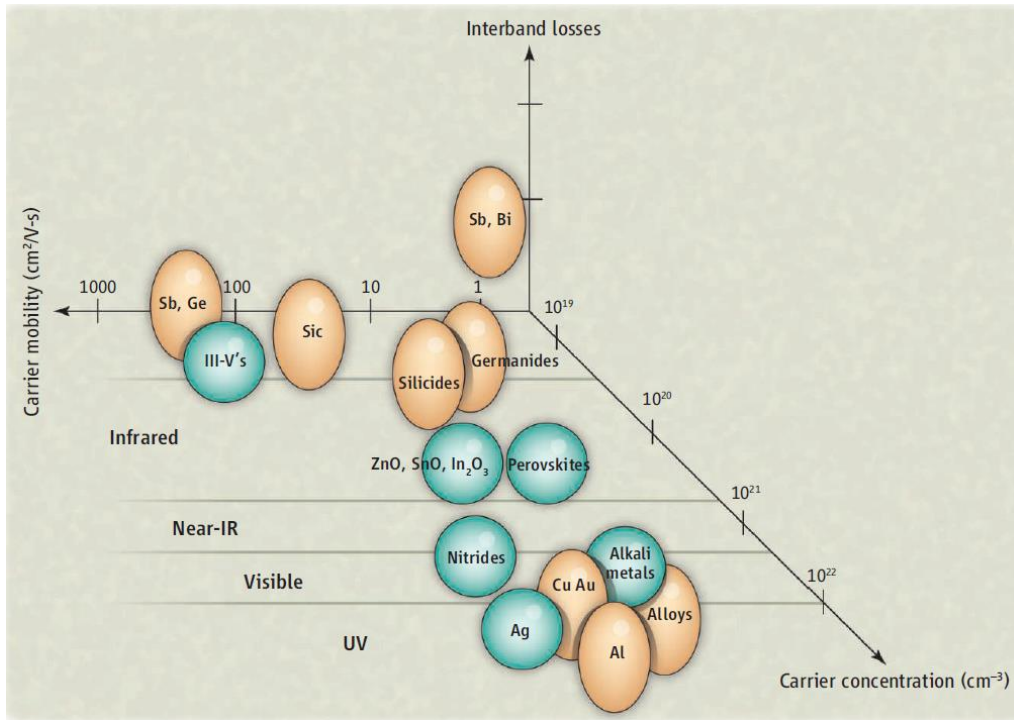
Fig. 2-2. Common plasmonic materials specified according to their carrier concentration, carrier mobility, and interband losses. Spherical bubbles represent materials with low interband losses, and elliptical bubbles represent those with larger interband losses in the electromagnetic spectrum. From ref. [11].

Group III-V compound semiconductors, like InAs and GaAs, are more desirable for mid-IR plasmonics applications than group-IV materials (e.g. Si and Ge), due to the low plasmonic losses originating from a higher mobility [11]. Heavily doped InAs is reported to show broadband plasmons in the spectral range from 5.5 to 15 μm by tuning the carrier concentration from 7.5×10^{19} to 2.7×10^{18} cm^{-3} [29]. In addition, patterned InAs nanoantennas with the length scale smaller than $\lambda_0/20$ are capable to detect very weak absorption resonances [19]. Fig. 2-3 shows detailed computational and experimental results for InAs nanoantennas. The simulation results for the near-field electric field distribution shown in Fig. 2-3(a) and (b) reveal the existence of two related longitudinal resonances propagating along the antenna arms, an air-like mode at the top position of the InAs/air interface and a substrate-like mode located at the InAs/substrate interface. These two resonant modes correspond to those two reflection/absorption peaks in Fig. 2-3(c). It also exhibits a resonance peak blue-shifted by increasing the doping concentrations. Furthermore, by coating PMMA on the top of antenna, the reflection spectrum redshifts by 71 cm^{-1} due to the change of the local refraction index of the surrounding of the nanoantenna, indicating the high sensitivity of heavily doped InAs. GaAs, the other III-V semiconductor, with a direct bandgap of $E_g = 1.42$ eV and high electron mobility, is widely used in the manufacture of optoelectronic devices. Even though with the

superior properties, GaAs is usually reported to be challenging for IR plasmonics because of the difficulty in achieving a high electron concentration (limited at $\sim 10^{19}$ cm^{-3}) [23, 30]. It should be noted that p-type GaAs has a larger effective mass and lower hole mobility, which means a high plasmonic loss and is undesirable in plasmonic applications. However, GaAs still holds the possibility as a superior mid-IR plasmonics material once its electron concentration exceed the $\sim 10^{19}$ cm^{-3} doping limit.
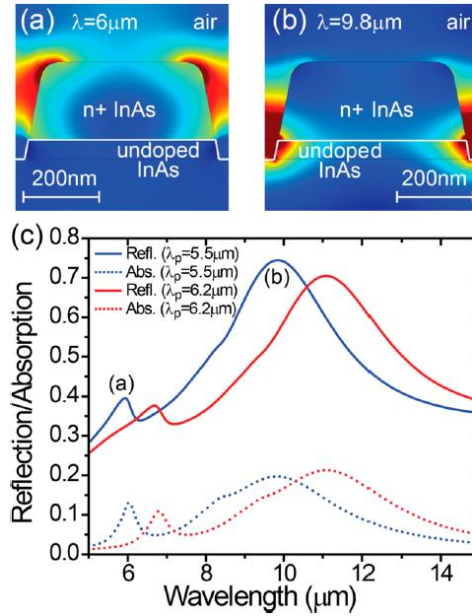
Fig. 2-3. (a) and **(b)** The simulated two electric field intensity configurations for InAs nanoantenna at two resonant wavelengths of 6 μm and 9.8 μm; **(c)** shows modeled reflection (solid lines) and absorption (dotted lines) for two heavily doped InAs layer with plasma wavelengths at 5.5 and 6.2 μm. From ref. [19].

2.1.2 Doping limitation in GaAs

Fig. 2-4(a) shows electron concentrations as a function of donor concentration in GaAs doped with S, Se, Te and Si [31]. It indicates that the activation efficiency of donors decreases as the donor concentration increases above the level of 3×10^{18} cm^{-3}, and the maximum carrier concentration saturates at the level of 1×10^{19} cm^{-3}. More specifically, for GaAs doped with Si (group IV), the highest electron concentration is in the range of 5×10^{18} cm^{-3}. Group IV dopants in GaAs are amphoteric, which means that they can act as donors or acceptors depending on the substitutional position. At low doping regime, Si replaces Ga donating into the system electrons while at high doping level (above 10^{18} cm^{-3}) Si substitutes As acting as a shallow acceptor. Thus, Si can compensate itself at high doping level, resulting in a low electron concentration [23]. Group VI elements such as S, Se or Te are donors in III-V semiconductors

and do not belong to amphoteric dopants. Nevertheless, the maximum achieved electron concentration is also limited to around 1×10^{19} cm^{-3}.

The physical origin of the doping limitations can be well explained by the compensating defect model [32]. The native defects in GaAs like vacancies, interstitials and antisite defects can be responsible for the reduction of the carrier concentration. Fig. 2-4(b) shows the formation energy of an acceptor (gallium vacancy (V_{Ga})) and a donor defect as function of the Fermi energy in the GaAs band gap. V_{Ga} is reported to be a triple acceptor for $E_F > E_V + 0.6$ eV, which trap electrons. Calculations of the electron concentration as a function of doping levels suggests that triple negatively charged gallium vacancies (V_{Ga}^{3-}) are responsible for the electron compensation (see Fig. 2-4(a)) [33], which gives a good fit to the experimental results. This shows the sublinear relation between the electron concentration n and the donor concentration N_d, and it follows $n \propto \sqrt[3]{N_d}$ at the donor concentration above 1×10^{19} cm^{-3}. The abundance of such kind of defects can increase with increasing dopant concentration and leads to a reduction in electron concentration. While for the low Fermi energies, V_{Ga}^{3-} is not stable and undergoes a transformation (Eq. 2-3) with the first neighbor As atoms moving towards the vacant Ga site. Such defect can trap holes instead of electrons.

$$V_{Ga} \Leftrightarrow (V_{As} + As_{Ga}) \qquad (2-3)$$

A similar amphoteric behavior is also predicated for V_{As}, where the transition is given by [34]:

$$V_{As} \Leftrightarrow (V_{Ga} + Ga_{As}) \qquad (2-4)$$

V_{As} is stable in GaAs when $E_F < E_V + 0.8$ eV and transforms to an acceptor-like $V_{Ga} + Ga_{As}$ when E_F is larger than $E_V + 0.8$ eV.

Another important feature about the native defects is that the total defect formation energy continuously decreases with increasing either n-type or p-type conductivity. This means that the defect concentration increases dramatically with increasing dopant concentration, where $E_F \cong E_C$ or $E_F \cong E_V$. This simultaneously decreases the effective electron concentration. Note that the E_{FS} in Fig. 2-4 (b), called the stabilized Fermi level, is close to the middle of the band gap in GaAs that is in agreement with the Fermi level pinning position observed at metal/semiconductor interfaces [35]. For Fermi energy $E_F > E_{FS}$ ($E_F < E_{FS}$) acceptor-like (donor-like) defects are predominantly formed resulting in a shift of the Fermi energy towards E_{FS}. The condition $E_F = E_{FS}$ is defined as the situation where the donor and acceptor-like defects are

incorporated at such rates that they perfectly compensate each other leaving the Fermi energy unchanged.

(a)

(b)
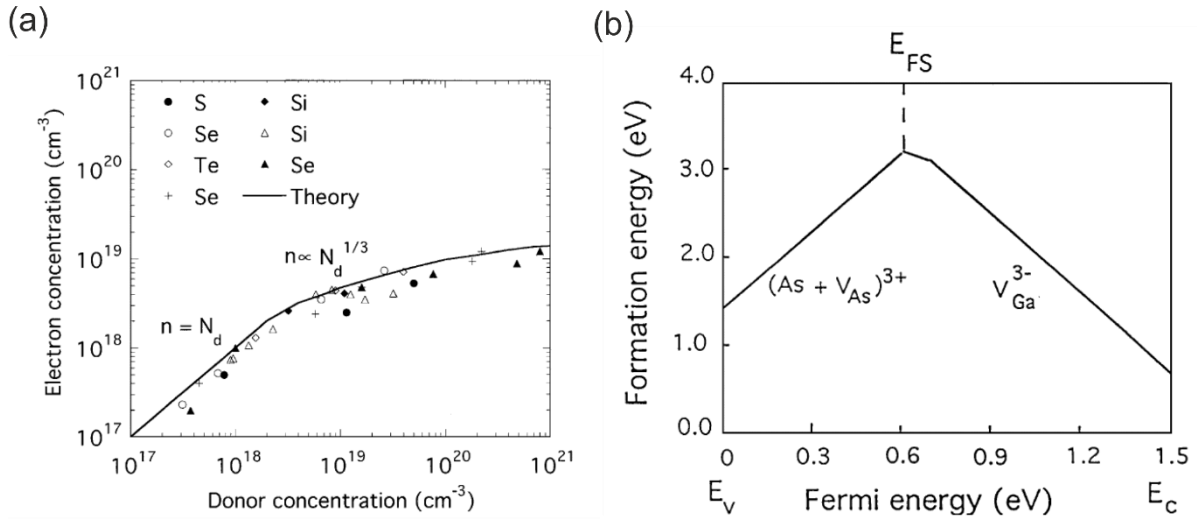
Fig. 2-4. (a) Electron concentration as a function of donor doping in GaAs for different dopants; **(b)** Formation energy of a gallium vacancy and the related donor defect as a function of the Fermi energy in GaAs band gap [31, 33, 34, 36]. From ref. [31].

In addition to native defects, the diffusion coefficient of dopants in the host crystal also plays an important role for carrier limitation. For p-type GaAs, the highest hole concentration is reported to be 1.5×10^{21} cm^{-3} in GaAs:C, because C possess the lowest diffusion coefficient in GaAs compared to different acceptors [32, 37]. Since the atom concentration in GaAs is 4.4×10^{22} cm^{-3}, the electrically active C concentration accounts approximately 3% of the total number of atoms in the host. Using beryllium doping, the maximum hole concentration is in the range of $\cong 10^{20}$ cm^{-3}. Be is a moderately fast diffuser in contrast to C. Zinc doping allows a hole concentration in the order of $\cong 10^{19}$ cm^{-3}. Zinc in GaAs is known to be a fast diffuser.

2.1.3 Sub-second annealing for hyperdoping semiconductors

Even if the carrier concentration is strongly limited by the solid solubility of dopants in semiconductors, the sub-second annealing performed after ion implantation or on the in-situ doped samples can overcome the solid solubility limit of dopants in semiconductors. This is not possible by using conventional annealing methods such as furnace annealing (FA) or rapid thermal annealing (RTA). Prucnal *et al.* reported an electron concentration for P doped Ge as high as 2.2×10^{20} cm^{-3} after ion implantation followed by ms-range flash lamp annealing (FLA) [38]. Wang *et al.* showed that the Te implanted in Si followed by nanoseconds pulsed laser annealing (PLA) causes a ultrahigh electron concentration up to 1×10^{21} cm^{-3} [39]. The reportedelectron concentrations are much above the solid solubility of dopants in Ge or in Si.

This method inspires us to apply sub-second annealing methods to GaAs in order to obtain an electron concentration beyond 10^{19} cm^{-3}, which can fulfill the requirements of heavily doped n-type GaAs as a plasmonic material.

The reasons why using sub-second annealing methods (FLA or PLA) hyperdoping in semiconductors is possible, can be explained by two aspects. One is by comparing the solute trapping or regrowth (τ_G) and diffusion time (τ_D) for impurity atoms over a semiconductor monolayer. If τ_D is larger than τ_G, it means that the dopants are able to be trapped at the moving amorphous/crystalline interface, instead of diffusing and forming precipitates. Zhou *et al.* have reported Se hyperdoped Si realized by ion implantation and FLA. The maximum electron concentration was in the order of 10^{20} cm^{-3}, which is about four orders of magnitude higher than the Se solubility in Si. They also compared the regrowth (τ_G) and diffusion (τ_D) times of Se elements in Si as a function of reciprocal temperature (see Fig. 2-5(a)) [40]. They show that τ_D is generally larger than τ_G especially in solid phase. That means that in solid phase processing selenium impurities can be trapped in the Si matrix if an optimized thermal treatment is applied. The author also pointed out that the short annealing time typical for FLA or PLA decreases significantly the diffusion length of impurity elements according to $L = (2Dt)^{1/2}$, where D is the diffusion coefficient. It means that, if the mean diffusion length of impurities at a certain annealing temperature is shorter than the average distance between impurities, the formation of precipitation/clustering is suppressed, that will increase the active carrier concentration. Fig. 2-5(b) presents the selenium diffusion length (L) in Si at different temperatures for different time duration. The three boxes indicate the working regime of different thermal process in solid phase including FLA, RTA and FA. This shows that an annealing processes performed in millisecond or microsecond time scale, while keeping the system in solid phase, could result in a minimized diffusion length.
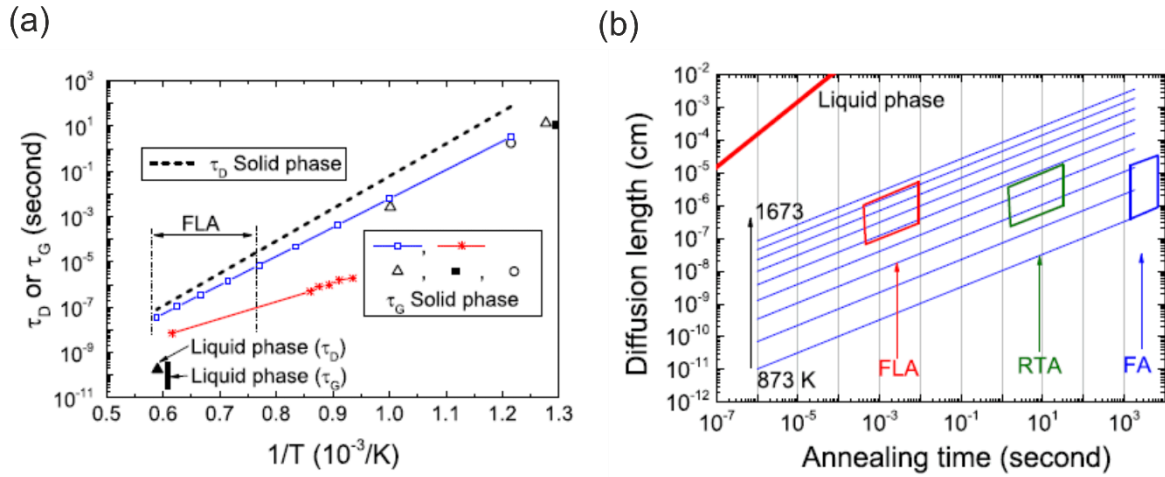
Fig. 2-5. (a) Competition between the Si solid phase (FLA) or liquid phase (PLA) recrystallization and selenium diffusion characterized by the time needed to regrowth (τ_G) or diffuse (τ_D) one monolayer. **(b)** Selenium diffusion length (L) in Si at different temperature vs. time duration. The three boxes indicate the working regime of different thermal process in solid phase: low temperature furnace annealing (FA) for more than 1000 second, rapid thermal annealing (RTA) for seconds and flash lamp annealing (FLA) for milliseconds at high temperature. From ref. [40].

On the other hand, defect concentrations and type of defects in semiconductors can also be modified by the sub-second annealing process. Prucnal *et al.* reported that 20 ms FLA at 1050 K can dissolve pre-existing phosphorus-vacancy clusters in *in-situ* P doped Ge [41]. Fig. 2-6 shows the positron annihilation lifetime τ_1 (a), and the intensities I_1 (b) as a function of the positron energy obtained from as-grown in-situ P-doped Ge samples after FLA from rear/front side annealing and from P-implanted Ge after rear-side annealing using FLA for 20 ms. The defects responsible for the positron annihilation lifetime τ_1 in the range of 260-290 ps is P_4V donor-vacancy complex. Compared to as-grown Ge:P, τ_1 decreases by 16 ps for P-implanted and FLA annealed Ge, which suggests that the main annihilation center in P-implanted and annealed sample is monovacancy bonded with P atoms. Additionally, FLA dissolves P_4V into monovacancy and isolated P atoms, which are immobile, because the annealing time is too short for phosphorus diffusion. It results in the increase of the fraction of electrically active P atoms from about 3.5×10^{19} cm^{-3} to about 8.0×10^{19} cm^{-3} after r-FLA and to about 6.2×10^{19} cm^{-3} after f-FLA. Fig. 2-6(b) demonstrates that after annealing the I_1 increases, implying a decrease of the concentration of the larger vacancy complexes.
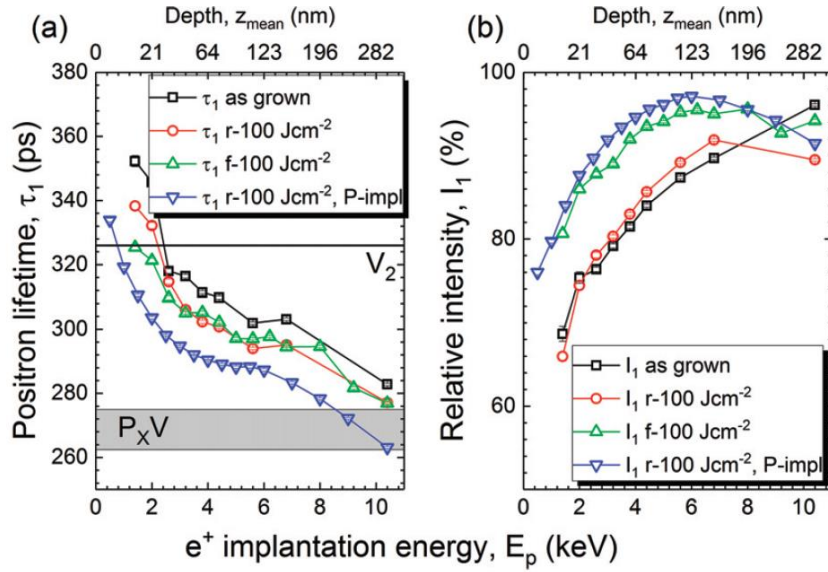
Fig. 2-6. (a) The positron annihilation lifetimes τ_1 (a), and the intensities I_1 **(b)** as a function of the positron energy/annihilation depth obtained from as-grown and FLA samples and from P-implanted sample annealed from rear-side. The horizontal lines in (a) indicate the positron annihilation in P_x-monovacancy (x≤4) and in V_2. From ref. [41].

In heavily doped n-type GaAs:Te, the compensating species is the donor atom bonded with the nearest gallium vacancy forming an acceptor, e.g., $Te_{As}V_{Ga}$ (for the case of group IV donors, both components of the complex are on the Ga sublattice, e.g., $Sn_{Ga}V_{Ga}$) [42, 43]. Gebauer *et al.* identified Ga vacancy-donor complexes (V_{Ga}-Te_{As}), tellurium donors (Te_{As}) and Ga vacancies (V_{Ga}). They are responsible for the charge carrier compensation mechanism in Te-doped GaAs by atomically resolved scanning tunneling microscopy [44]. The concentration of the V_{Ga}-Si_{Ga} complex as a deep positron trap in GaAs increases with increasing Si concentration [45-47]. It starts to be more and more visible when the Si concentration exceeds 5×10^{18} cm^{-3}. The compensation effect leads to a decrease of the electron concentration in n-type GaAs:Si. With the advanced functionality of the sub-second annealing method, it should be possible to achieve, in n-type GaAs, an electron concentration exceeding the solid solubility of donors by dissolving donor-vacancy complexes.

2.1.4 High-doping effects in GaAs

At high doping concentration, many properties of semiconductors are altered. These changes are due to either a high concentration of impurities or free carriers.

(i)   The Mott transition

The Mott transition refers to an insulator-to metal transition occurring in semiconductors at high dopant concentrations. At low temperature (T→0 K), the conductivity for a doped semiconductor with low doping concentration is expected to be negligible (zero in the ideal case), since free electrons freeze out onto localized donor states. Conductivity in this regime is commonly interpreted by hopping theory that electrons hop from neutral donors to ionized donors. The conductivity is referred to hopping conductivity and is described by the formula $\sigma_{hop} = \left(\alpha/T^\beta\right) exp\,(-\frac{E_{hop}}{kT})^\gamma$ [32], where α and β are constants, E_{hop} is the thermal activation energy for the hopping process and γ determine the functional dependence of the exponential factor. γ=1/4, 1/3, 1/2 or 1 corresponds to Mott-law of variable range hopping (VRH) for 3-dimensional and 2-dimensional systems, the Efros-Shklovskii (ES) VRH (a Coulomb gap in the density of states (DOS)), and the nearest-neighbour hopping, respectively. As the doping concentration increases, the Coulomb potentials of impurities overlap, resulting in electrons transferring from one donor to another donor more easily by tunneling or by thermal emission over the barrier. The probability of both processes increases with decreasing donor separation. Consequently, the activation energy for electron transport is reduced and approaches zero in the extreme case leading to finite conductivity even at T→0 K. Then the semiconductor possess the metal-like property. Fig. 2-7 presents the resistivity of carbon-doped GaAs in the temperature range from 1.7 to 300 K with a transition from insulating to the metallic range by tuning the hole concentration from 1.30×10^{17} to 1.29×10^{19} cm^{-3} [48]. It shows that the acceptor impurity concentration N_a =1×10^{18} cm^{-3} is a critical concentration for metal-insulator transition in p-type GaAs:C. Note that the critical concentration can also be estimated by the Mott criterion $N_a^{\frac{1}{3}}a_B = 0.26 \pm 0.05$ [49], where a_B is the effective Bohr radius. The critical donor concentration in GaAs with an effective Bohr radius r_B^*=103 Å is calculated to be N_{crit} =1.6×10^{16} cm^{-3} for n-type GaAs [50].
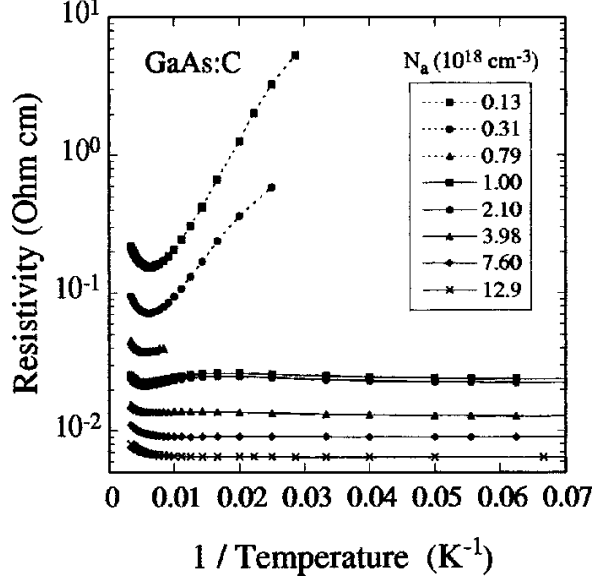
Fig. 2-7. Resistivity on a logarithmic scale versus inverse temperature for GaAs:C with different acceptor impurity concentrations. From ref. [48].

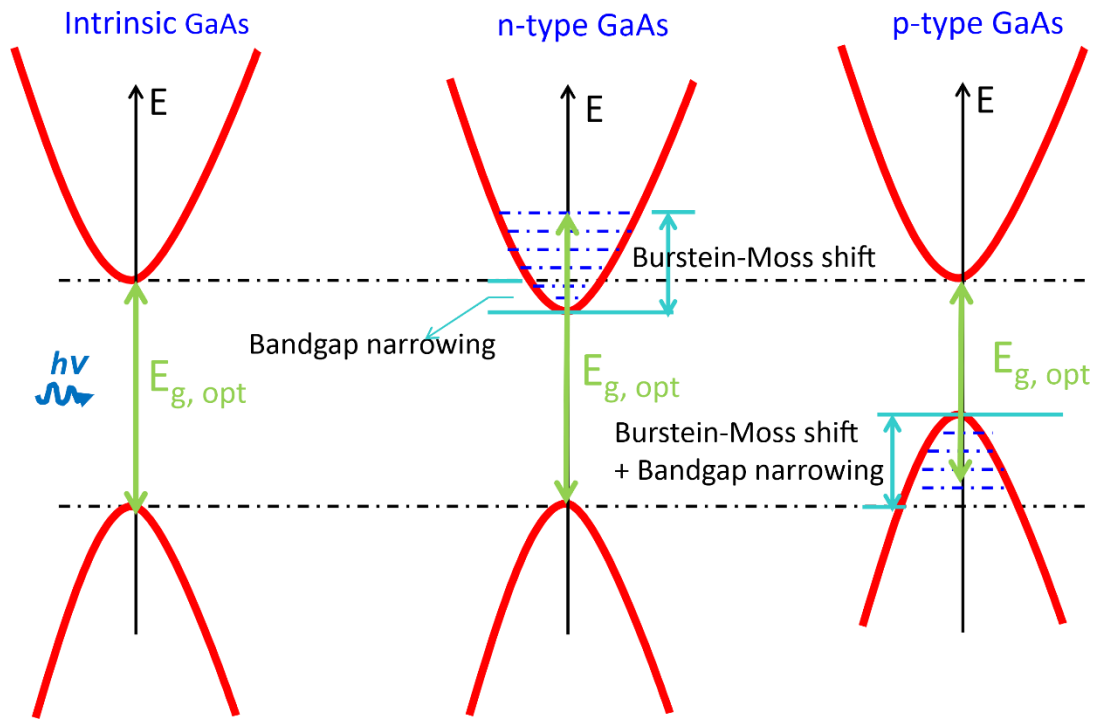### (ii) The Burstein-Moss shift vs. Bandgap narrowing

The shift of the absorption edge towards higher energies occurring at high doping concentrations is referred to as the Burstein-Moss effect [51]. The up-shift of the absorption edge is related to band filling effect. The conduction band becomes significantly filled at high doping concentrations due to the finite density of states. Due to band filling, absorption transitions cannot occur from the top of the valence band to the bottom of the conduction band. As a result, the fundamental edge of absorption transition shifts from E_C-E_V=E_g in undoped semiconductors to E_C-E_V>E_g in heavily doped n-type semiconductors. Quantitatively, the Burstein-Moss shift can be calculated from the filling of the conduction band or valence band in n-type and p-type semiconductors, respectively. The band filling for a single-valley, isotropic, and parabolic band is in the limit of extreme degeneracy given by $E_F - E_C (E_V) = \frac{\hbar^2}{2m_e^*}(3\pi^2 n)^{2/3}$, where n is the free carrier density and m_e^* is the electron effective mass. Note that the Burstein-Moss shift is inversely proportional to the effective mass. This means that the Burstein-Moss effect is more prominent in semiconductors with light carrier masses. For example, the blueshift is clearly observed in n-type GaAs ($m_e^* = 0.067m_0$), but not in p-type GaAs ($m_{hh}^* = 0.45m_0$) [32].

At high doping concentrations, the bandgap energy of semiconductors decreases. The bandgap decreases with increasing doping concentration and is usually referred as bandgap narrowing or bandgap renormalization. The most important reasons for bandgap narrowing are many-body effects of free carriers, which lower the electron energies as compared to a non-

15

interacting carrier system. This interaction becomes important at small carrier-to-carrier distances, i.e., at high free carrier concentrations. At room temperature, the magnitude of bandgap renormalization can be estimated by the classical self-energy of an electron interacting with an electron gas, i.e. interacting with its own polarization field [32]. The self-energy of an electron interacting with an electron gas is defined as $\Delta E_g \cong e \lim_{r \to 0} [V_s(r) - V(r)]$ where $V(r)$ is the Coulomb potential and $V_s(r)$ is the screened Coulomb potential of an electron in an electron gas. This equation represents the change in electrostatic energy of an electron before and after the electron gas has spatially redistributed itself to reduce the Coulomb interaction energy. By inserting the screening radii and a screened potential, ΔE_g can be further deduced as [32]:

$$\Delta E_g = -\frac{e^3 \sqrt{m^*(3n)^{\frac{1}{3}}}}{4\,\pi^{\frac{5}{3}}\varepsilon^{\frac{3}{2}}\hbar} \qquad (2-5)$$

The change in energy gap follows a 1/3 power of the doping concentration. The Burstein-Moss shift and bandgap narrowing are two phenomena, which cause the absorption edge of highly doped semiconductors to change in opposite directions. The Burstein-Moss shift prevails in n-type GaAs, resulting in a blueshift of the absorption edge and radiative transitions. In p-type GaAs, band gap narrowing prevails and results in a redshift of the absorption edge and radiative transition. The strongly different absorption characteristics of p-type and n-type GaAs are due to the heavier hole mass compared to the effective electron mass. The Burstein-Moss shift is inversely proportional to the carrier effective mass, which results in less band filling in p-type GaAs. Fig. 2-8 depicts the radiative transition in intrinsic, heavily *n*-doped and heavily p-doped GaAs with the influence of Burstein-Moss shift and bandgap narrowing. Fig. 2-9 demonstrates the RT PL emission obtained from p-type GaAs:Zn with a hole concentration of 1.65×10^{18} cm^{-3} and n-type GaAs:S with an electron concentration of 1.1×10^{17} cm^{-3} [42]. In comparison with un-doped GaAs the GaAs:Zn presents a redshift of PL emission, while the n-type layer shows a blueshift [52]. Similar results were reported by Chen *et al*., where a redshift for band-to-band and acceptor-to-band transition of around 15 meV and 20 meV in p-type carbon doped GaAs with the hole concentration increasing from 8×10^{17} to 1.1×10^{20} cm^{-3} was observed [53]. Hudait *et al*. demonstrated a band gap shrinkage by 120 meV in p-type zinc doped GaAs by increasing the hole concentration from 8×10^{17} to 1.1×10^{20} cm^{-3} [54]. De-Sheng *et al*. observed a blueshift reaching approximately 150 meV in n-type GaAs:Te by tuning the electron concentration from 2×10^{16} to 2×10^{19} cm^{-3} [55].

Fig. 2-8. Schematic energy diagram for the optical bandgap in intrinsic, heavily *n*-doped and heavily p-doped GaAs. Burstein-Moss shift dominates in *n*-type GaAs, while the bandgap narrowing effect prevail in *p*-type GaAs.
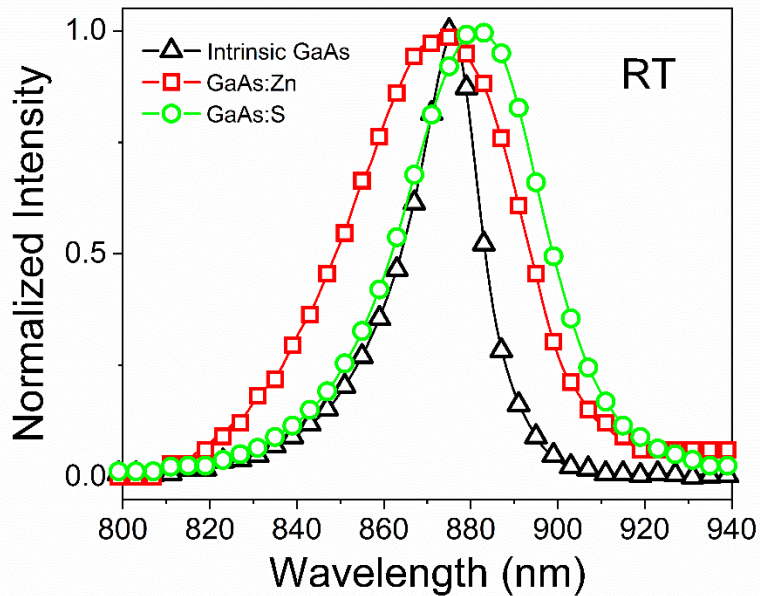
Fig. 2-9. Normalized room temperature photoluminescence spectra obtained from intrinsic GaAs and ion implanted GaAs after flash lamp annealing.

(iii)   Weak localization in heavily doped GaAs

Besides donating electrons, dopant atoms also introduce disorder into the system [56, 57]. In disordered semiconductors, multiple random elastic scattering of electrons from impurities leads to the quantum-interference (QI) phenomena, i.e., weak-localization (WL). WL is a consequence of constructive interference of two wave components starting at some point and returning to the same point after traversing time-reversed paths as shown in Fig. 2-10(a). More specifically, if the probability amplitudes for the wave packet to move from point r_0 along some path C_1 back to r_0 be A_1 and along a different path C_2 be A_2, then the transition probability for the particle to move either along C_1 or along C_2 will be [58] :

$$w = |A_1 + A_2|^2 = w_{cl} + w_{int} \qquad (2-6)$$

where $w_{cl} = |A_1|^2 + |A_2|^2$ and $w_{int} = 2Re(A_1^* A_2)$. For any two paths the interference term w_{int} may be positive or negative, and thus averages to zero. However, if $A_2 = A_r$ is the amplitude of the time-reverse of path $A_1 = A$ and if time reversal invariance remains, then $A = A_r$, i.e., the probability of return w is enhanced by a factor of two compared to the probability w_{int} of a classical system:

$$w = 4|A|^2 = 2w_{cl} \qquad (2-7)$$

This effect manifests itself as a positive correction to the resistivity of the metal or semiconductor. If the electrons during this process have strong momentum coupling (usually introduced by spin-orbit coupling), the angle of the spin sweeping out is π as it traverses the time reversible path. Then $w \approx 0$ [59]. This destructive interference effect suppresses backscattering leading to a weak anti-localization (WAL) effect as shown in Fig. 2-10(b). WAL results in a decrease in the resistivity of a metal or semiconductor. WAL is widely reported in topological insulators.

The applied magnetic field can break the time reversal symmetry and lead to a dephasing of destructive (WLA) or constructive (WL) interference. This phase factor strongly depends on the flux through the loops. Therefore, with a small increase in the magnetic field, the localization disappears quickly. This gives rise to a sharp cusp at low magnetic field, which is the signature of WAL (positive magnetoresistance or negative magnetoconductance) and WL (negative magnetoresistance or positive magnetoconductance), as shown in Figs. 2-10(a) and

(b). The WAL and WL effects are typically analyzed using the Hikami-Larkin-Nagaoka (HLN) formalism, which was developed in the 1980s for 2D systems [60].
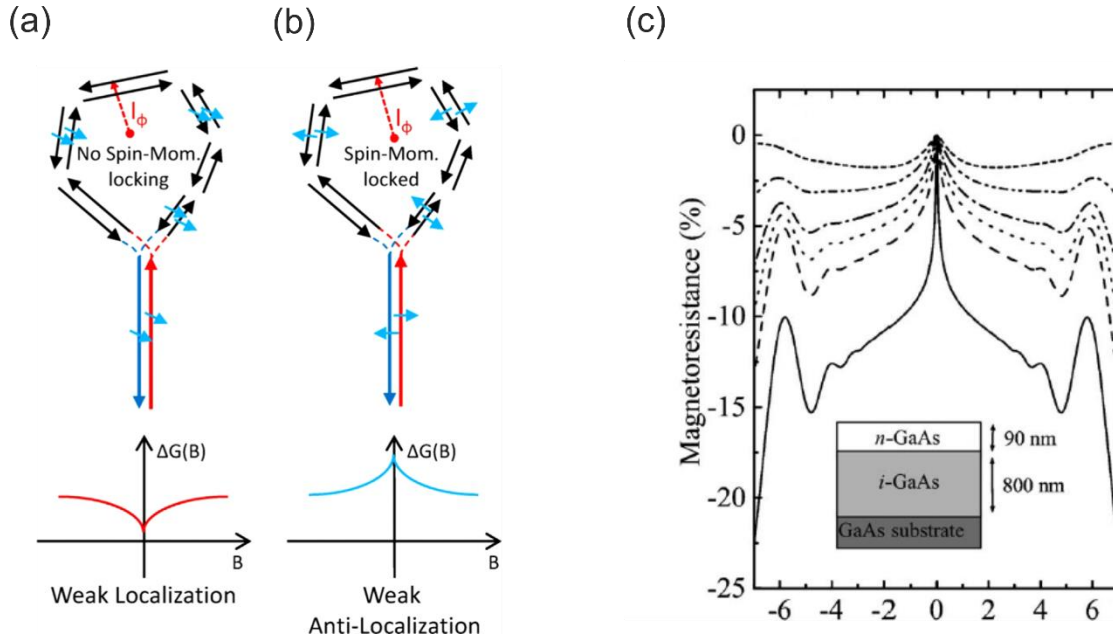
Fig. 2-10. (a) and **(b)** weak localization and weak anti-localization occur due to coherent backscattering along time reversible paths in the absence and presence of the spin-momentum locking, respectively. The relative magnetoconductance (MC) is $\Delta(B)=G(B)-G(0)$, where G(B) and G(0) are the conductance under magnetic field and zero field. From ref. [59]. **(c)** The magnetoresistances for n-type GaAs measured at T= 2, 10, 15, 30 and 40 K. The inset is the schematic of the layer structure. From ref. [61].

Negative magnetoresistance (NMR) has been widely observed in doped semiconductors. Rosenbaum *et al*. reported that phosphorus-doped silicon with electron concentration tuned from 3.7×10^{18} to 7.0×10^{18} cm^{-3} goes through the insulator-to-dmetal transition and shows NMR in the metalic-phase at low magnetic field. Gilbertson *et al*. investigated a 90 nm thick n-type GaAs epitaxial thin film using magnetotransport measurement and based on the weak localization theory they extracted a phase coherence time of ~30 ps at 2 K [61]. Fig. 2-10(c) shows the magnetoresistance measurements at T= 2, 10, 15, 30 and 40 K. The inset is the schematic of the layer structure. A strong NMR associated with the WL effect is observed at $B < 2\,T$. Weak Shubnikov-de Haas oscillations are resolved at high fields ($B > 3T$). The carrier density and mobility are determined to be 2.83×10^{17} cm^{-3} and 1660 cm^{2}V^{-1}s^{-1} at 2 K, respectively. In addition, Monsterleet *et al*. reported electron-electron interaction correction including the contribution of orbital and Zeeman affecting WL model for the metal-insulator transition regime of the n-GaAs [62]. Newton *et al*. found the n-type Ge displays WL and p-type Ge shows WAL by analyzing the magnetoresistance in the temperature range down to 1.6

K [63]. Moreover, using HLN fitting, the extracted phase coherence lengths can be as larger than 325 nm in the heavily doped n-type Ge ($n=5.3\times10^{19}$ cm^{-3}), suggesting possible applications in quantum technologies. In p-type Ge, the spin diffusion length of ~20 nm does not change over a broad temperature range. ZnO and $(Zn, Al)O_x$ thin films also show weak localization and phase coherence length as long as 100 nm at 2 K [57, 64]. It has also been shown that the WL effect is observed in GaAs quantum wells, like $Al_xGa_{1-x}As/GaAs/Al_xGa_{1-x}As$, due to the degenerate two-dimensional electron gas (2DEG) inside the quantum well [65, 66]. Thus, it is necessary to investigate the magnetotransport behavior of doped semiconductor in order to better understand the fundamental physics and aiming for possible applications like spintronic and quantum devices.

## 2.2 Van der Waals heterostructure based on TMDCs

2.2.1 Transition metal dichalcogenides

Transition metal dichalcogenides (TMDCs), the most studied 2D van der Waals materials besides graphene, are atomically thin semiconductors with the stoichiometric formula MX_2 [67], where M is the transition metal element (Mo, W, etc.) and X is the chalcogen (S, Se or Te). The bulk TMDCs exhibit a wide variety of polymorphs and stacking polytypes, i.e. 1T, 2H and 3R, where the letters stand for trigonal, hexagonal and rhombohedral, respectively, and the number denotes the number of X-M-X units in the unit cell. Figure 2-11(a) exhibits the 1T, 2H and 3R polytypes of MoS_2 [68]. Polymorphism can have a significant influence on the electronics of TMDCs, e.g., 2H and 3R show semiconducting properties while 1T exhibits metallic properties [67]. The TMDCs monolayer consists of a layer of transition metal atoms sandwiched between two layers of chalcogenide atoms. TMDCs have strong in-plane covalent bonds and weak out-of-plane van der Waals interactions. The weak van-der Waals forces between the layers allow easy exfoliation of atomically thin layers (monolayer with a thickness of 6~7 Å). In this thesis, $MoSe_2$ with 2H structure was chosen for optical and electrical studies. Figure 2-11(b) shows the structure of a hexagonal $MoSe_2$ monolayer, where Mo atoms are highlighted in violet and Se atoms in yellow.
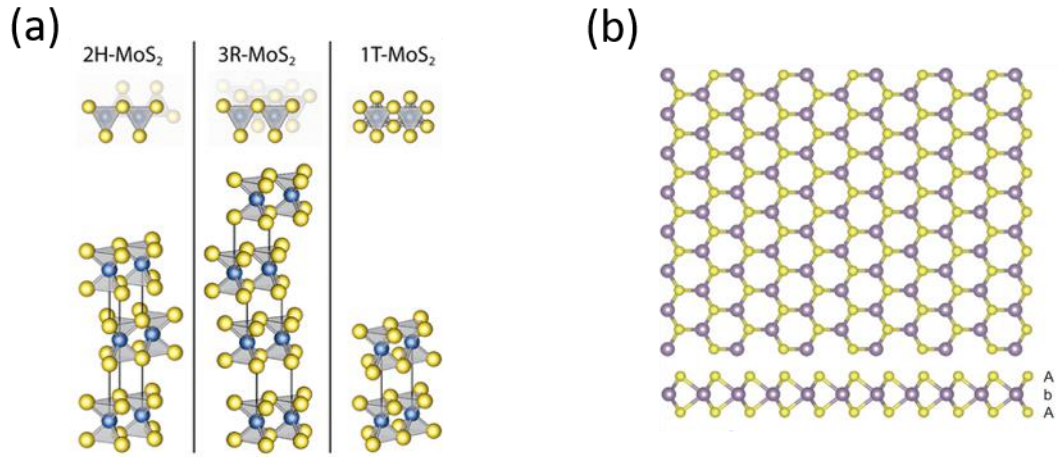
Fig. 2-11. (a) Stacking polytypes of bulk TMDCs. **(b)** The structure of a hexagonal $MoSe_2$ monolayer where Mo atoms are highlighted in violet and Se atoms in yellow. From ref. [68].

Figure 2-12 shows the calculated band structures of MoS_2, WS_2, $MoSe_2$, and WSe_2 with thickness ranging from 1 monolayer (ML) to 4 ML [69]. When the thickness of TMDCs goes down to 1ML, the conduction band minimum (CBM) and valence band maximum (VBM) are located at the K point, showing a direct bandgap in the energy range of 1.5~2.1 eV depending on TMDCs. Note that the local extrema of the conduction and valence bands at K point are barely affected by the change of flake thickness. These bands are formed by the $d_{x^2-y^2} + d_{xy}$ orbitals of Mo (W) atoms and the $p_x + p_y$ orbitals of in-plane S (Se or Te) atoms [70], therefore the energy of the bands at the K points is almost not changed by varying the thickness. Increasing the thickness of TMDCs to 2 ML and more, the VBM moves to Γ point while the CBM is located at Q or K points (see details in Figure 2-12), causing the formation of a smaller indirect bandgap compared to their 1 ML case. At the Γ point, the bands are a combination of p_z orbitals of S atoms and d_z^2 orbitals of Mo atoms, which has a strong out-of-plane character. As a result, the bandgap of TMDCs decreases with increasing thickness.
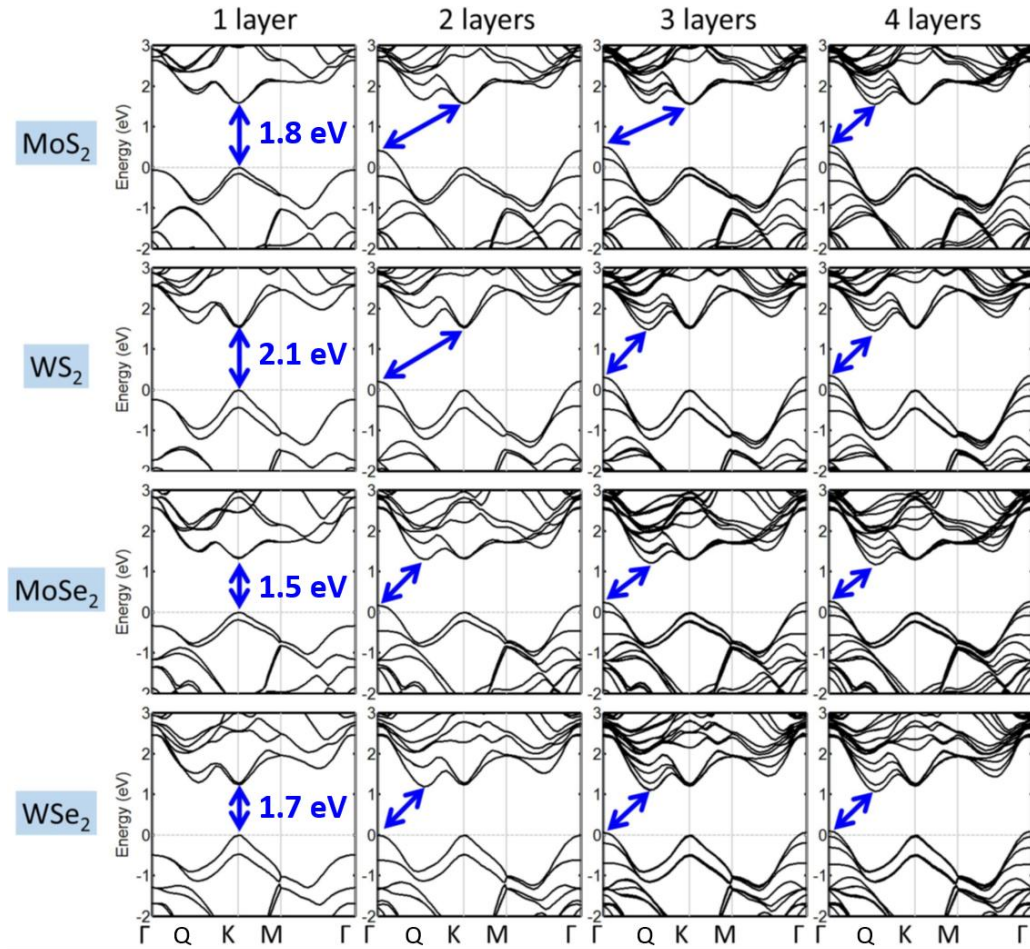
Fig. 2-12. Band structures of MoS₂, WS₂, MoSe₂, and WSe₂ for different thicknesses. For all cases, the valence band edge at Γ point becomes higher with increasing the number of layers due to the interlayer interaction, but the amount of spin splitting does not change significantly with the number of layers. From ref. [69].

The optical band gap can be manifest by photoluminescence (PL) measurements. Figure 2-13 presents the room temperature PL obtained from 1 ML, 2 ML and multilayer MoSe₂. The exciton emission for 1ML occurs at 1.55 eV and has the highest intensity, while the exciton emission for 2 ML and multilayer MoSe₂ shifts down to 1.51 eV. Furthermore, the peak intensity decreases with increasing the layer thickness and the peak itself becomes broader.
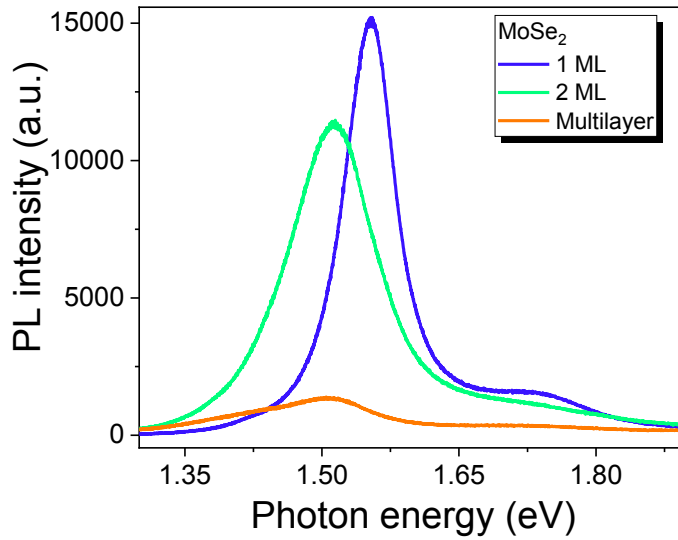
Fig. 2-13. Room temperature PL emission of 1 ML, 2 ML and multilayer MoSe$_2$ under 532 nm laser excitation with the laser power of 3.2 mW.

For TMDCs, the Mo or W atoms are heavy and the band edges at the K point are from d-orbitals of transition metal, which introduces a strong spin-orbit coupling (SOC). Strong SOC can remove spin degeneracy in both conduction and valence bands, and leads to strong energy splitting between spin-up and spin-down states. Specifically, based on theoretical calculations, the valance band splitting for MoSe$_2$ and WSe$_2$ is 0.184 and 0.466 eV, respectively, while the conduction band splitting is much smaller, 0.007 and 0.038 eV, respectively [71, 72].

The first Brillouin zone in TMDCs contains two inequivalent K valleys called K+ and K-. The energy of bands extrema at K+ and K- are the same, but they have opposite spins, as shown in Figure 2-14 [72], which originates from the broken parity symmetry. Thus it is possible to selectively excite different valleys with circular polarized charity light due to spin-valley locking rule, i.e., a right-handed circular polarized photon (σ+) initializes a carrier in the K+ valley, while a left-handed circular polarized photon (σ-) initializes a carrier in the K- valley [69, 73]. This degree of freedom provides a new concept by controlling carriers in K-valley index, called valleytronics, aiming for information processing and storage applications.
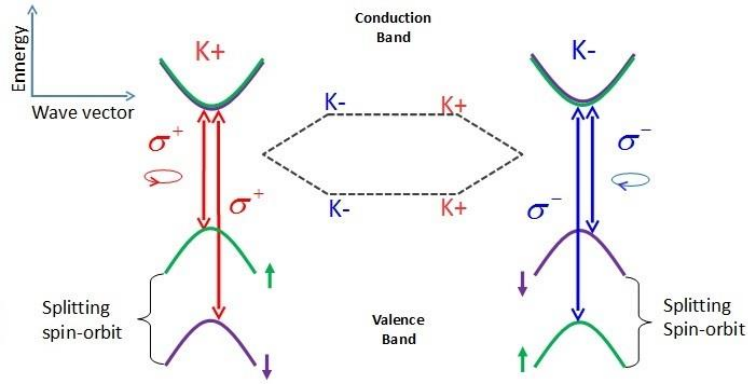
Fig. 2-14. Spin splitting in 1 ML TMDCs and optical selection rules. From ref. [72].

The reduced dimensionality suppresses the dielectric screening of charged carriers in ultrathin TMDCs and this makes the binding energy of excitons much larger than in traditional semiconductors, e.g., up to several hundred meV. Note that an exciton in 2D materials can be treated like a hydrogen atom, with an electron bound to a hole [74]. In addition, a neutral electron-hole pair can receive an extra electron or hole to form a charged exciton called a trion. The optical band gap for a trion is smaller than for a neutral exciton due to the increased binding energy by adding an extra charge. The trion binding energy for monolayer TMDCs is as large as 20-40 meV [1]. Figure 2-15(a) shows that the negatively charged exciton (X^-) in the monolayer $MoSe_2$ has a binding energy of about 30 meV. Ross. et al. also reported that by using back gating in field-effect transistors (FET) monolayer $MoSe_2$, the charge states of exciton can be manipulated from positive to neutral or to negative by tuning the carrier density [75].
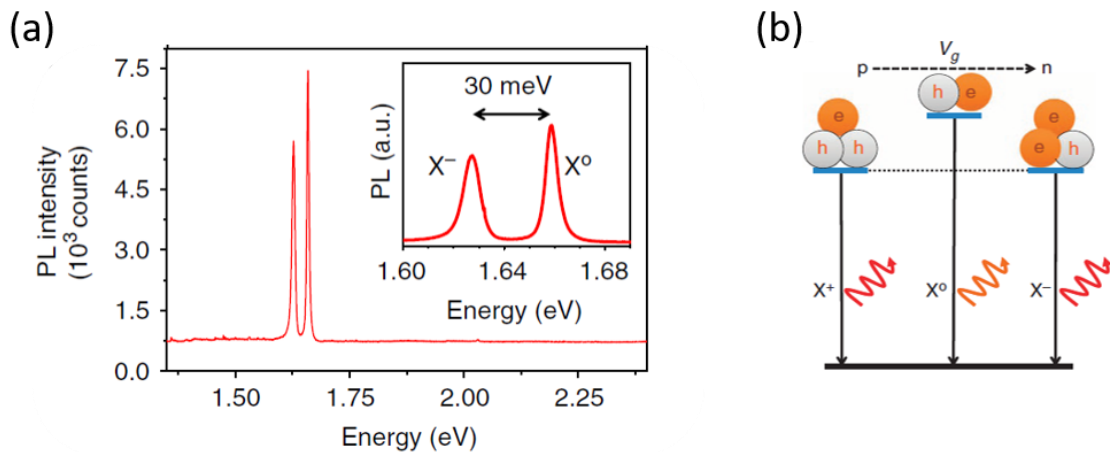

Fig. 2-15. (a) PL excited by laser with the photon energy of 2.33 eV shows neutral exciton (X^0) and the lower-energy charged exciton (X^-) at 20 K. The X^- shows a binding energy of about 30 meV. **(b)** Illustration of the gate-dependent trion and exciton quasi-particles and transitions. From ref. [75].

2.2.2 Metal phosphorus trisulfide

Another newly emerged class of van der Waals crystals, metal phosphorus trisulfide (MPS$_3$), where M= Fe, Ni, Mn, has recently attracted a tremendous attention in the scientific community. MPS$_3$ forms a monoclinic structure with the space group of C2/m. For the crystal structure, the transition metal atoms sit in the 4g position with a local symmetry of 2, forming a honeycomb lattice, surrounded by six S atoms with trigonal symmetry. These S atoms are connected to two P atoms above and below the M plane like a dumbbell [76, 77], as shown in Figure 2-16.
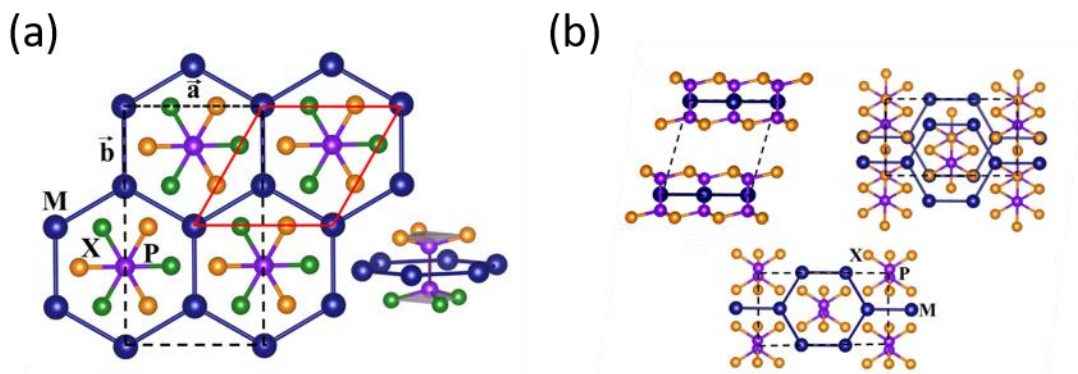

Fig. 2-16. Schematic structure of (a) and (b) MPS$_3$ with (P$_2$X$_6$)$^{4-}$ bipyramids, enclosing the metal atoms. From ref. [77].

There are two distinctly different characteristics of MPS$_3$ compared to TMDCs. One is that the bandgap of MPS$_3$ (in the range of 1.5-3.0 eV) is larger than that of most of TMDCs [77], i.e. 1.5 eV for multilayer FePS$_3$, 1.7 eV for multilayer NiPS$_3$ and 3.0 eV for multilayer MnPS$_3$ [78]. This means that MPS$_3$ is a promising material for optoelectric devices in the UV region. Gao et al. reported a FePS$_3$ UV photodetector with a responsivity as high as 171 mAW^{-1} when the device is illuminated with 254 nm light [79]. In addition, NiPS$_3$ and MnPS$_3$ have also been reported as high sensitive UV photodetectors [80, 81]. FePS$_3$ and NiPS$_3$ are indirect bandgap materials, while based on theoretical calculations, MnPS$_3$ shows indirect-to-direct transition as the thickness is reduced down to a monolayer [82].

Moreover, MPS$_3$ are antiferromagnetic semiconductors, indicating their potential applications in low-dimensional magnetic and spintronic devices. The Néel temperatures for bulk FePS$_3$, NiPS$_3$ and MnPS$_3$ are 123, 155 and 78 K, respectively [83]. The magnetic properties of FePS$_3$ can be well described by the Ising model, while NiPS$_3$ and MnPS$_3$ are described by the anisotropic and isotropic Heisenberg Hamiltonians, respectively [83]. Lee, et al. reported that FePS$_3$ remains Ising-type antiferromagnetic ordering down to the monolayer limit [76].

Specifically, they performed temperature dependent Raman measurement where the Néel temperature can be determined based on the change of the phonon structure. When the crystal undergoes an antiferromagnetic transition, the structure of the phonon mode P_1 (Figure 2-17(a)) changes from four separated peaks ($P_{1a} - P_{1d}$) to a broad one P_1 as temperature increases above Néel temperature. Similar properties are also exhibited by $NiPS_3$ and $MnPS_3$ [84, 85]. Figure 2-17(b) shows the bulk magnetic susceptibility of $FePS_3$, exhibiting the Néel temperature at 117 K and indicating a greater change in susceptibility along the c-axis than along a- and b-axes, i.e., the magnetic ordering is the Ising type. McCreary, et al. performed magnetic-field dependent Raman of $FePS_3$ at T=5 K, and found that P_{1d} can split into two components P_{1d}^1 and P_{1d}^2, where the frequency of P_{1d}^1 (P_{1d}^2) decreases(increases) with increasing magnetic field, as shown in Figure 2-17(c). It indicates that P_{1d} mode is actually a magnon [86].
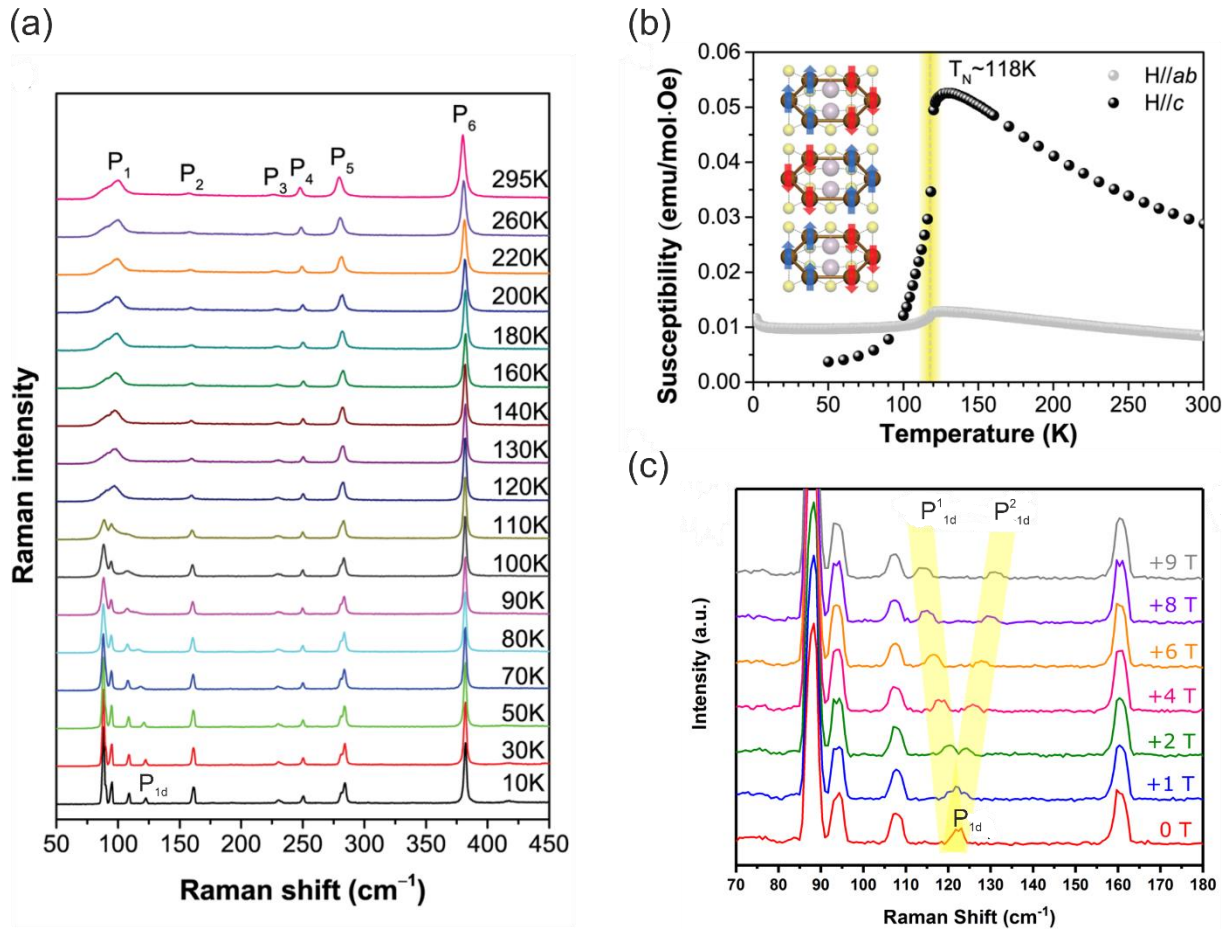
Fig. 2-17. (a) Temperature dependence of Raman spectra for bulk $FePS_3$. **(b)** Temperature dependence of magnetic susceptibility along a- or b- (gray spheres) and c- (black spheres) axes. From ref. [76]. **(c)** Magnetic-field dependent Raman of $FePS_3$ at T=5 K, showing the splitting of ψ_4 into two components, $\psi_4^{(1)}$ and $\psi_4^{(2)}$, where the frequency of $\psi_4^{(1)}$ ($\psi_4^{(2)}$) decreases(increases) with increasing magnetic field. From ref. [86].

2.2.3 Van der Waals heterostructures

Van der Waals heterostructures (vdWH) can be easily achieved by selecting constituent layers with desired properties. The interlayer bonding is realized through very weak van der Waals forces. It has two prominent advantages compared to transitional semiconductor heterostructures, i.e. a rotational degree of freedom and a less request for lattice constant matching [7, 87]. Thus, vdWHs provide a versatile platform for the study of novel physical phenomena, e.g. interlayer excitons with high binding energy [88, 89], and device applications, like field effect transistors [90], optoelectronic devices [7], spintronics [91].

From the point of view of band alignment, there are three types of possible heterostructures, as shown in Figure 2-18. In the case of type I, the conduction band minimum (CBM) and the valence band maximum (VBM) of the narrow band gap material (NBG), i.e. material A, are located inside the wide band gap material (WBG), i.e., material B. Due to the band offset, electrons and holes excited in the WBG transfer into NBG, as indicated by arrows. The carriers are then confined in the NBG, which promotes radiative recombination and is desirable for light-emitting application. Such a structure design has already been used in double heterostructure laser [92, 93], which was honored in 2000 with the Nobel Prize in Physics for H. Kroemer and Zh. Alferov. Specifically, the NBG material GaAs is sandwiched between two layers of WBG materials AlGaAs with n- and p-doped. Electrons and holes from n- and p-doped AlGaAs transfer to GaAs under forward bias. Thus, electrons and holes both present in GaAs, recombine and emit photons. This can increase the laser efficiency. In type-I vdWHs, carriers can be confined in NBGs even within the monolayer. Zheng, et al reported that the PL emission of WS_2 monolayer is enhanced by up to 106-fold in WS_2/PbI_2 heterostructure [94]. This PL enhancement in NBG has also been shown for $MoTe_2/WSe_2$, GaSe/GaTe, GaS/GaSe heterostructures [95, 96].
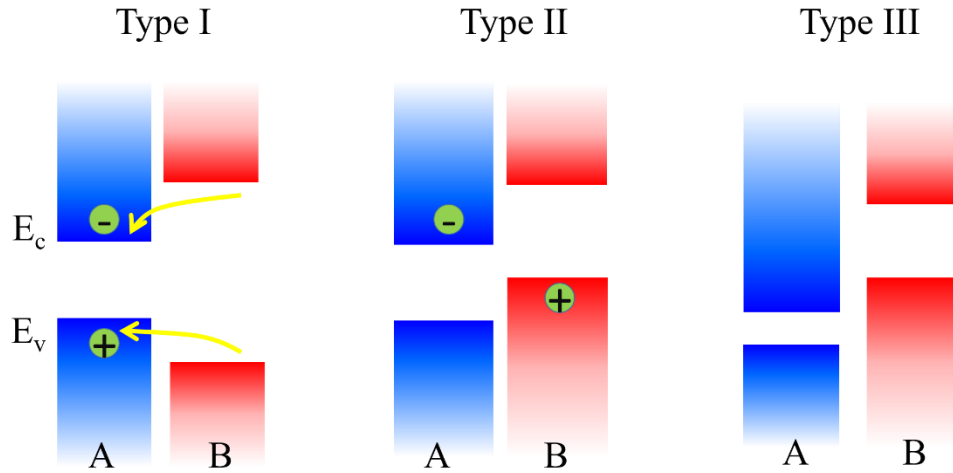
Fig. 2-18. Type-I, type-II and type-III band alignment in semiconducting heterostructures.

In the case of type-II band alignment, the CBM and VBM are located in different materials, as shown in the middle panel in Figure 2-18. Holes photogenerated in material A diffuse into material B, while electrons photogenerated in material B diffuse into material A. In TMDCs vdHWs with type-II band alignment, electrons and holes are confined in different materials and form so-called interlayer excitons. In $WSe_2/MoSe_2$, the occurrence of interlayer excitons is observed with the appearance of additional PL emission at energies lower than the intralayer excitons of a single layer [88, 89]. The lifetime of interlayer excitons can be enhanced up to 100 ns [97]. An interlayer exciton is optically bright if its kinematic momentum is zero (i.e., when the CBM and VBM are matched in momentum space) [98]. Therefore, an interlayer exciton is bright or dark is affected by the band structure and the size of the Brillouin zone of its constituent layers. This explains the reason why the interlayer exciton is mostly observed in TMDC vdHWs [99], e.g. WS_2/WSe_2, $MoS_2/MoSe_2$, MoS_2/WS_2, etc.

In type-III band alignment (right panel of Figure 2-18), the conduction band edge of semiconductor A lies below the valence band edge of semiconductor B. This type of heterojunction can be treated like a semimetal that has no bandgap and the states are available for holes or electrons at all energies.

Taking into account the unique and different properties for $MoSe_2$ and $FePS_3$, we expect heterojunction made of $MoSe_2$ and $FePS_3$ can reveal previously unknown phenomena in the field of optoelectronics.

Chapter 3. Experiment techniques and device fabrication

3.1 Ion implantation

Ion implantation is an industry-standard method for semiconductor doping, which can introduce energetic ions to the surface region of a target sample and modify its chemical composition. Compared to other doping techniques, ion implantation has the following advantages: i) precise control of the depth distribution of dopants in the samples; ii) the doping concentration can be higher than the solid solubility; iii) high efficiency, good homogeneity and reproducibility, etc. Heavily doped semiconductors are desired for plasmonic applications operated in the near- and mid-infrared spectral range. In this work, n-type GaAs with the carrier concentration higher than the equilibrium solid solubility is prepared for mid-infrared plasmonics. Samples are fabricated by ion implantation followed by sub-second annealing.

During the ion implantation process, energetic ions strike the host matrix and travel a "drunkard's" path through the crystal as their directions are changed due to collisions between the ions and the host atoms (including nuclei and electrons). Finally, the ions will stop at some depth. The initial energy of the ions is usually several tens of keV, which is much higher than the lattice energy and can stimulate elastic collisions between pairs of nuclei. The second component of scattering is due to inelastic collisions with electrons. The energy loss per unit penetration depth S is given by $S = (\frac{dE}{dx})_{nuclear} + (\frac{dE}{dx})_{electronic}$. Depending on the ion energy and ion mass, during single collision cascade many host atoms can be recoiled away from their lattice positions. This disturbs the perfect crystal structure. If the ion fluence is above a threshold, an amorphization of the implanted layer can be observed. The depth profile of the implanted ions follows a Gaussian stopping distribution, which is related to the projected range, R_p, the standard deviation ΔR_p, and the implantation fluence Φ. The relationship between those parameters can be expressed as follows:

$$N(x) = \frac{\Phi}{\sqrt{2\pi}\Delta R_p} exp[-\frac{(x-R_p)^2}{2(\Delta R_p)^2}] \qquad\qquad (3\text{-}1)$$

Where $N(x)$ is the concentration of the implanted ions at depth position x, and the exponential term equals to 1. Consequently, the peak concentration N_p can be described as:

$$N_p = \frac{\Phi}{\sqrt{2\pi}\Delta R_p} \qquad\qquad (3\text{-}2)$$

In addition, ion implantation allows for achieving a box-like depth profile of impurities in the solid. This can be done using a multiple implantation with difference energies and fluences. Ions implanted with higher energy stop in the host deeper than ions implanted with lower energy. By proper designing of the ion fluence and energy, homogeneous doping concentration over the depth of a few hundred nanometer is possible. This can be simulated by using software Stopping and Range of Ions in Matter (SRIM) [100]. Figure 3-1 shows the depth profile of Te implanted into GaAs with three different implantation energies and fluences. The implantated layer has thickness of about 300 nm and the Te concentration is of about 4.9×10^{19} cm^{-3}. In order to avoid channeling effect during the ion implantation (ions traveling without significant large-angle scattering), all the samples in this study are tilted by 7° with the respect to the ion beam.
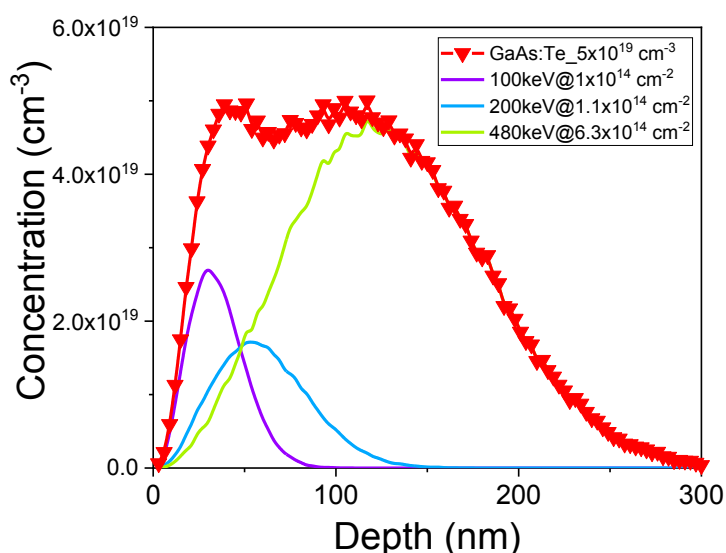

Fig. 3-1. Depth profile of Te implanted into GaAs with three implantation energies and fluences. Specifically, 100 keV with a fluence of 1.0×10^{14} cm^{-2}, 200 keV with a fluence of 1.1×10^{14} cm^{-2} and 480 keV with a fluence of 6.3×10^{14} cm^{-2}. Such a procedure gives a Te peak concentration of about 4.9×10^{19} cm^{-3}.

3.2 Flash lamp annealing and pulsed laser annealing

In order to activate dopants and repair the damage of implanted layer, high temperature annealing is necessary after the implantation process. In this work, two types of sub-second annealing methods are employed, i.e., flash lamp annealing (FLA) in milliseconds and pulsed laser annealing (PLA) in nanoseconds. Both annealing techniques are different from the traditional annealing method, e.g. furnace annealing (FA) or rapid thermal annealing (RTA), which are techniques based on the thermal equilibrium conditions. Using FA or RTA the

maximum dopant concentration which can be incorporated into the solids is limited by the solid solubility. For dopant concentration higher than the solid solubility, the segregation and clusters formation are observed during conventional annealing. Sub-second annealing, e.g. FLA and PLA, is non-thermal-equilibrium annealing process. The use of short time annealing can suppress the dopant diffusion and eliminate the possibility of cluster formation. Figure 3-2 shows the depth distribution of S in GaAs before and after the FLA for 10 ms with the peak temperature of about 1100 °C [52]. S was implanted with energies of 10 or 30 keV. The depth distribution and concentration of dopants are defined by ion implantation parameters. Apparently, independent of the implantation energy, during annealing only very slight diffusion of S is observed, which means that the ms-flash lamp annealing highly suppresses the dopant diffusion during the high temperature recrystallization process.
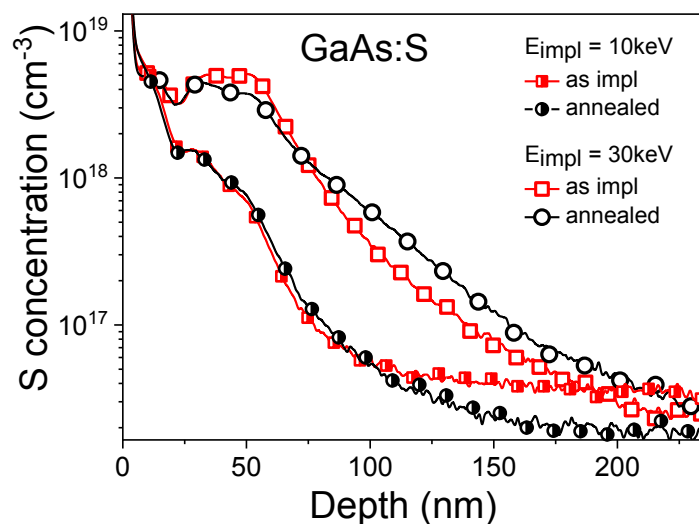
Fig. 3-2. S distribution in as-implanted and annealed GaAs:S samples with the ion implantation of 10 and 30 keV obtained by secondary ion mass spectrometry.

Figure 3-3 shows the scheme of millisecond-range flash lamp annealing (FLA) tool [52]. It is composed of 12 Xe-lamps with the size of 25 cm long each and a reflector to homogenize the flash light deposited on the sample surface. The emission spectrum of the Xe-lamps covers the broad wavelength range from 300 up to 800 nm. This means that the samples absorbing light in the UV-visible spectral range, e.g. GaAs, can be effectively annealed using this FLA system. Xe lamps are ignited by a bank of capacitors charged with high voltage, which provides pulse of energy. By manipulating the capacity or the resistance in the discharge R-L-C circuit, the flash duration can be tuned. The flash pulse can be changed between 0.3 and 20 ms with the

highest energy density of about 140 J/cm^2. The maximum temperature that can be achieved within the single flash pulse strongly depends on the annealed substrates. Moreover, the peak temperature is limited by the melting point of the annealed semiconductor, e.g., for Si it is about 1400 ºC while for GaAs the peak temperature is about 1150 ºC. However, during the FLA process the peak temperature should not exceed the melting temperature due to surface degradation and fast diffusion of dopants in the liquid phase. Therefore, the ion implanted layer treated by FLA recrystallizes usually via solid-phase epitaxy regrowth. This one is done at slightly lower than the melting point of the materials being processed. Importantly, during the ultra-short time annealing most of energy is deposited close to the surface which allows to anneal thin films deposited on the temperature-sensitive substrates like polymers or glass.
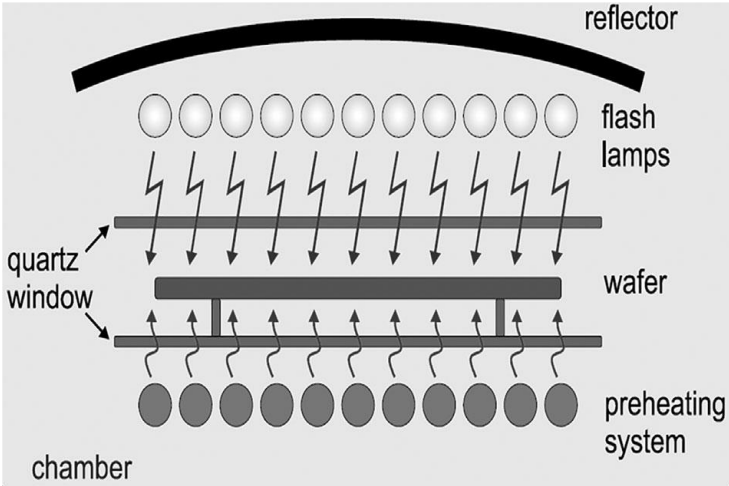
Fig. 3-3. Basic scheme of a FLA tool used for semiconductor wafer processing. From ref. [101].

Fig 3-4. Excimer laser system applied for pulsed laser annealing.

Beside FLA, another sub-second annealing method, i.e., pulsed laser annealing (PLA), is used to anneal ion implanted GaAs samples. A XeCl excimer laser with a wavelength of 308 nm and a repetition rate of 10 Hz is guided onto the sample. Figure 3-4 shows the excimer laser system applied for PLA. The pulse duration is fixed at 28 ns. The laser spot is homogenized and focused by a fly-eye homogenizer as a 5×5 mm^2 square spot. The energy of the spot is manipulated by a manual attenuator in the range from 0.15 to 1.2 J/cm^2. The laser light is absorbed close to the surface and converted rapidly to heat. For certain pulse energy the implanted region melts within first nanoseconds and remains liquid for a few hundred nanoseconds. Then, the implanted layer solidifies and recrystallizes by a rapid liquid-phase epitaxial regrowth. During such a process the concentration of dopants which can be incorporated into the semiconductor can be a few orders of magnitude higher than the equilibrium solid solubility. In rapid liquid-phase epitaxy, the solidification front moves at the velocity of a few m/s that is extraordinary in materials processing. The molten layer can be much thicker than the penetration depth of the UV photons in the annealed sample and should be a bit thicker than the implanted layer to achieve a better recrystallization. This process results in an epitaxial film of the desired semiconductor alloy with implanted atoms remaining within the molten layer. In this work, PLA is mainly used to activate dopants in 300 nm thick GaAs implanted with Zn, S and Te, and FLA is employed for the thinner implanted GaAs of about 100 nm.

3.3 Hall effect measurement

Electrical and magneto-transport characterization of heavily doped GaAs were performed by a Lake Shore 9700A Hall Measurement System in cryogenic setups applying high magnetic field (-4 to 4 Tesla) by a superconducting magnet. The temperature range is from 3 to 400 K controlled by Helium cooling and heating system. The detectable limitation for resistance is in the range of 0.04 mΩ to 200 GΩ for electrical measurements. GaAs samples have the size of 5 $\times$ 5 mm^2. Van der Pauw method is used for the electrical and magneto-transport study.

Figure 3-5 shows a common van der Pauw (vdP) geometry used for electrical characterization of GaAs samples [102]. The vdP geometry is adopted to measure the electrical properties of a sample of any arbitrary shape with the thickness much thinner than the width, i.e., approximately two-dimensional. For the resistivity measurement, a current can be applied to terminal 1 and 2, and the voltage can be detected at terminal 3 and 4. A resistance in the horizontal direction can be calculated based on the Ohm's law: $R_{12,34} = \frac{V_{34}}{I_{12}}$. By changing the

current polarity and switching the current-voltage detection channel, $R_{21,43}$, $R_{34,12}$, $R_{43,21}$ can be obtained. Thus, an averaged resistance in the horizontal direction is described as follows:

$$R_h = \frac{R_{12,34} + R_{34,12} + R_{21,43} + R_{43,21}}{4} \qquad (3-3)$$

Likewise, $R_{23,41}$ for the vertical edge can be obtained. The averaged resistance in the vertical direction is shown by:

$$R_v = \frac{R_{23,41} + R_{41,23} + R_{32,14} + R_{14,32}}{4} \qquad (3-4)$$

Finally, the actual sheet resistance R_S is deduced based on the van der Pauw formula [103]:

$$e^{-\pi R_v/R_S} + e^{-\pi R_h/R_S} = 1 \qquad (3-5)$$

The electrical resistivity ρ can be obtained by $\rho = R_S d$, where d is the thickness of the sample.

For the Hall effect measurement, an external magnetic field with the direction perpendicular to the sample surface is needed. It can introduce the Lorentz force to the flowing carriers. In the vdP geometry, when current I_{24} is applied to the sample under a positive magnetic field (positive z-direction), the Hall voltage $V_{13, P}$ is recorded due to the Lorentz force. Similarly, by reversing the magnetic field direction, current direction or switching current-voltage applying-detection channels, $V_{13, N}$, $V_{24, P}$, $V_{24, N}$, $V_{31, P}$, $V_{31, N}$, $V_{42, P}$ and $V_{42, N}$ can be recorded. Note that negative Hall voltage is also obtained here. The averaged Hall voltage V_H is the mean value of absolute eight Hall voltages. The sheet carrier density n_S and mobility μ are estimated by following equations [104]:

$$n_S = \frac{IB}{q|V_H|} \qquad (3-6)$$

$$\mu = \frac{1}{q n_s R_S} \qquad (3-7)$$

where the unit of sheet carrier density and the Hall mobility is cm^{-2} and $cm^2 V^{-1} s^{-1}$, respectively. I represents the current, B stands for the magnetic field, q is the elementary charge ($q = 1.602 \times 10^{-19}$ C) and R_S is the sheet resistance.
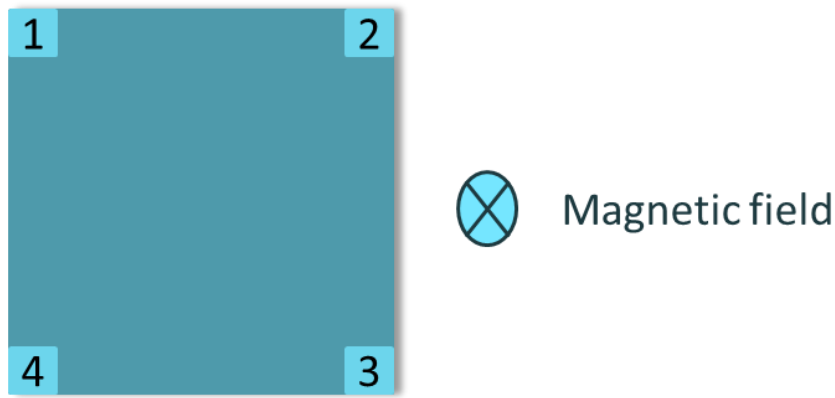
Fig. 3-5. Schematic representation of resistivity and magneto-transport measurements using common van der Pauw geometry for a square sample [105]. The small squares at the corner with numbers represent the electrical contacts. The magnetic field direction is perpendicular to the sample plane.

3.4 Mechanical 2D flake transfer
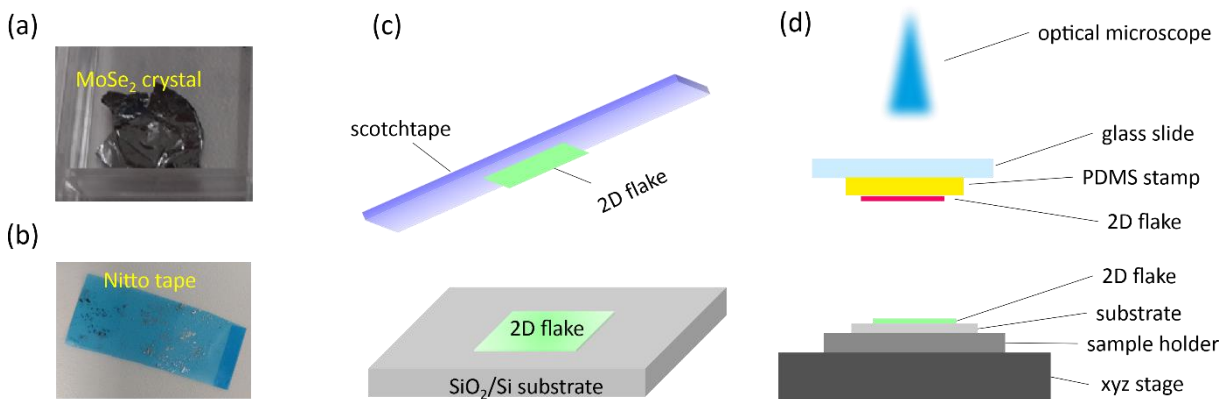
Fig. 3-6. Exfoliation and transfer process of van der Waals flakes. **(a)** Van der Waals bulk crystal ($MoSe_2$). **(b)** Blue Nitto tape. **(c)** Schematic of the $MoSe_2$ flake transferred from the Nitto tape on SiO_2/Si substrate. 2D flake can stay on a substrate after blue tape contacted and stripped away from substrate. **(d)** Sketch of using a micromanipulator to precisely fabricate heterojunctions made of different 2D flakes.

Mechanical exfoliation with the scotch tape is an easy and mature method to obtain van der Waals flakes with different thickness down to monolayer. Figure 3-6(a) and (b) show a $MoSe_2$ crystal and a blue Nitto tape used in the exfoliation process. The general process for this method is that the scotch tape can hold 2D flakes after contacting with the vdW crystal. After repeating the contact-release process several times, i.e., mainly by exerting a normal force to the flakes, flakes become thinner and thinner. Then, by contacting the tape and the SiO_2/Si substrate, exfoliated flakes can be transferred on to substrates for the follow-up research. Figure 3-6(c)

illustrates the "scotch tape" method for preparing thin flakes. SiO_2 with the thickness of 90 nm is used in our study since it gives a good contrast for monolayer and bilayer vdW flakes.

For the preparation of vdW heterostructures, a micromanipulator (Figure 3-6(d)) is used. With the micromanipulator we can precisely align and stack different flakes together. Here, we first transfer flakes from the scotch tape to polydimenthylsiloxane (PDMS) films stuck to a glass slide. The targeted flakes on the transparent PDMS stamp and the underlying substrate are visible under the optical microscope. The position of substrate can be controlled with a piezo electric xyz-stage. After alignment of the flakes on the PDMS and on the substrate in the xy- direction, the piezo z-stage is moved until both flakes are in contact. The parameters like substrate temperature, pressure, contact duration are crucial for the successful heterojunction formation.

3.5 Photolithography and EBL

Photolithography with UV Mask Aligner Süss MA6 is employed to prepare pre-patterned gold contacts for 2D materials. This is one of the most effective techniques to fabricate electrical contacts for the characterization of 2D materials. Figure 3-7 shows the step by step photolithography process. The SiO_2/Si substrate is firstly coated with promotor AR300-800 using spinning speed of 3000 rpm, and then the coating layer is baked for 5 min at 150 °C. After this, negative photoresist maN-1420 is spin coated with the speed of 3000 rpm and baked for 2 min at 115 °C. The photoresist is exposed under UV light through a photomask. Next, the sample is placed into a developer solution maD 533 for 2 min and immersed in stopper DI-water for 2 min. The resulting pattern in the photoresist layer on the substrate can be used as an evaporation mask for metal contacts e.g., Ti/Au. At the end, the photoresist is dissolved in acetone bath followed by isopropanol (IPA) bath for cleaning, i.e., the lift-off process. The metal contacts remain only in the unexposed regions, and the rest is removed together with photoresist. The pre-patterned gold contact is preferred for 2D flakes which are unstable at ambient conditions, since it does not require additional time for the follow-up metal deposition or electron-beam lithography (EBL) processes.

EBL is also used in this study to fabricate gold contacts on the top of 2D flakes. In such a case the vdW flakes are firstly transferred on the substrate and then the metal contacts are deposited. The details about EBL is not presented here, since EBL has very a similar working principle like photolithography. In contrast to photolithography, EBL uses a focused electron beam scanning to draw custom shapes on a surface covered with an electron-sensitive film, e.g., polymethyl methacrylate resist (PMMA), hydrogen silsesquioxane (HSQ), etc. The resolution

can go down to sub-10 nm. Since vdWH devices are varied in size, shape and position on the substrate, therefore, the EBL can be an excellent method to locate targeted sample and fabricate contacts.
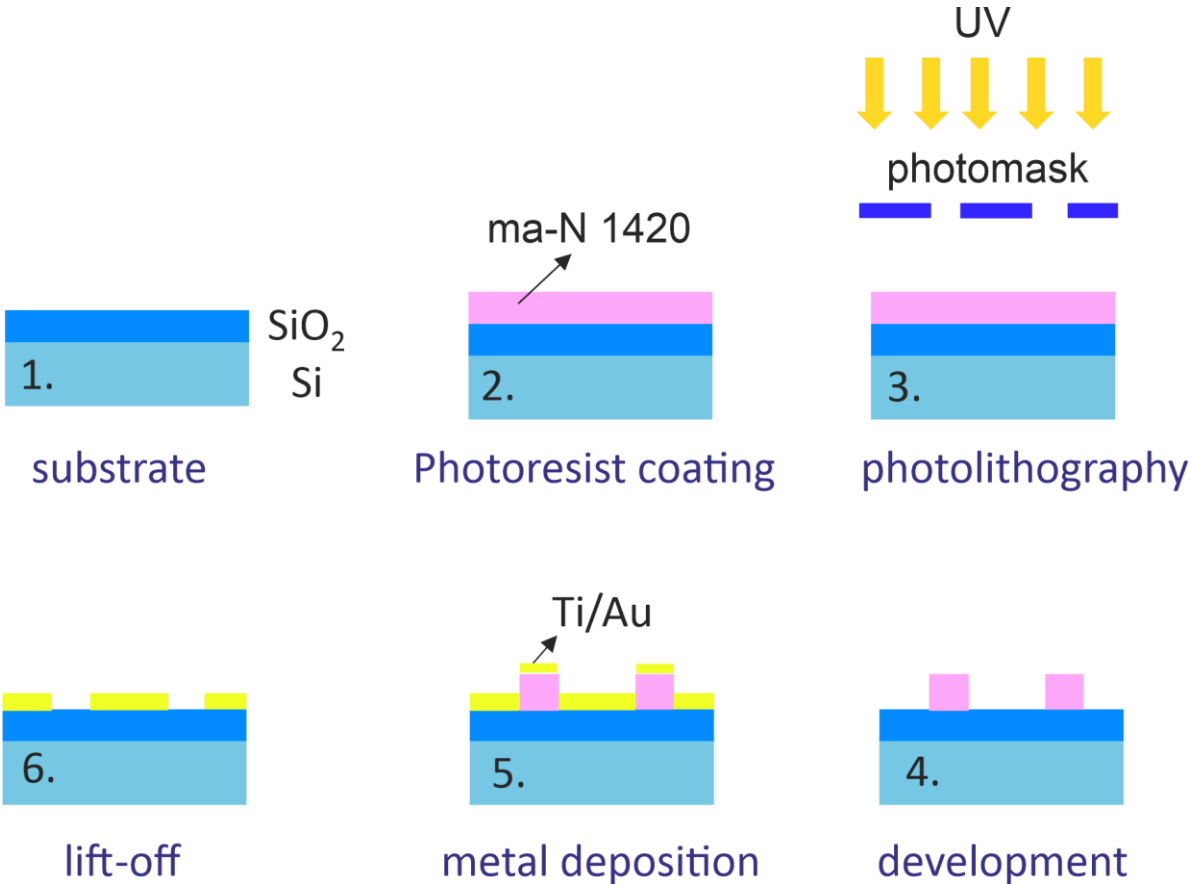
Fig. 3-7. Schematic of using photolithography to prepare pre-patterned gold contact for 2D materials. Step1: a Si substrate with 90 nm SiO_2. Step 2: promotor and negative photoresist are spin-coated on top of the substrate. Step 3: after baking, the photoresist layer is exposed to UV light with a photomask. Step 4: the un-exposed photoresist region is removed in a developer solution. Step5: Ti/Au deposition. Step 6: pre-patterned gold contacts are obtained after the lift-off process.

Chapter 4 Plasmonic and magnetotransport properties of heavily doped GaAs

Ion implantation of S and Te followed by sub-second flash lamp annealing with peak temperature about 1100 °C is employed to obtain metallic n^{++}-GaAs layers. The electron concentration in annealed GaAs is as high as 5×10^{19} cm^{-3}, which is several times higher than the doping level achievable by alternative methods. We found that heavily doped n^{++}-GaAs exhibits positive magnetoconductance in the temperature range of 3-80 K, which is attributed to the magnetic field suppressed weak localization. By fitting the magnetoconductance results with Hikami-Larkin-Nagaoka model, it is found that the phase coherence length increases with increasing carrier concentration at low temperature and is as large as 540 nm at 3 K. The temperature dependence of the phase coherence length follows $l_\emptyset \propto T^\eta$ ($\eta \sim 0.3$), indicating defect-related scattering as the dominant dephasing mechanism. In addition, the high doping level in n-type GaAs provides the possibility to use GaAs as a plasmonic material for chemical sensors operating in the infrared range.

This chapter is prepared for publications:

Juanmei Duan, Changan Wang, Lasse Vines, Lars Rebohle, Manfred Helm, Yu-Jia Zeng, Shengqiang Zhou and Slawomir Prucnal, Increased dephasing length in heavily doped GaAs, submitted to *New Journal of Physics*. FLA is done by S. Prucnal. Ion implantation is done by IBC at HZDR. All the measurements and analysis were done by the thesis author. The thesis author also wrote the manuscript.

Juanmei Duan, Qi Li, Wanchun Wu, Lars Rebohle, Yuehui Lu, Glen Yen-Hsun Lin, Yu-Jia Zeng, Minghui Hong, Manfred Helm, Shengqiang Zhou and Slawomir Prucnal, Mid-infrared plasmonics in heavily doped GaAs, to be submitted (2021). The etching was done by G. Lin from national Taiwan Univ. All the measurements, simulation and analysis were done by the thesis author. The thesis author also wrote the manuscript.

4.1 Introduction

In disordered electron systems, the electrons can be localized, which leads to weak localization (WL) and eventually Anderson insulators [106]. WL is a quantum mechanical effect where the constructive interference occurs between two electron waves traveling along a closed path in an opposite direction, leading to a suppression of conductivity. Under the action of a magnetic field, the two waves acquire a phase difference and the interference conditions are violated and causing a positive magnetoconductance (PMC, or negative magnetoresistance (NMR)). The theory of PMC in doped semiconductor was proposed decades ago [107] and explained by WL on the metallic side of the insulator-metal transition (IMT) [62, 63]. PMC has already been reported in δ-doped layers in GaAs [108], GaAs quantum wells [66] and GaAs/Al_xGa_{1-x}As heterostructures [109]. In the above-mentioned cases, the large amount of carriers are confined within a thin layer. However, unlike heavily doped Si and Ge epilayers [63, 110], PMC in GaAs epilayers has rarely been reported, due to the doping limitation for *n*-type GaAs. PMC in GaAs epilayers has not yet been reported in metallic-like n-type GaAs with carrier concentration above 10^{18} cm^{-3}, due to the n-type doping limitation. Moreover, although PMC effect has been reported in n-type GaAs film in the insulator-metal transition regime with carrier concentration in the order of 10^{16} cm^{-3} film, it is highly dependent on electron-electron interaction effect including orbital and Zeeman contributions [61, 62]. Specifically, Monsterleet et al., have showed a PMC effect in n-GaAs close to the metal-insulator transition, in which the electron concentration is 2.9×10^{16}cm^{-3} [62]. In addition, Gilbertson et al., have reported a weak localization with a 2D to 3D crossover in n-type GaAs with the doping level of 4×10^{17}cm^{-3} as temperature increases from 2 to 50 K [61]. The reason for the doping limitation in GaAs is mainly due to the compensating effect. Si is the most common *n*-type dopant for GaAs. Unfortunately, Si in GaAs is an amphoteric dopant, which limits the effective electron concentration to the level of about 5×10^{18} cm^{-3} [111, 112]. Specifically, for high doping level, Si occupies both Ga and As sites, donating both electrons and holes simultaneously, which causes compensation effect and decreases the effective carrier concentration.

A reasonable alternative for n-type doping in GaAs is choosing shallow donors from group VI, i.e. chalcogens like S, Se or Te [31, 113-115]. Chalcogens in GaAs are located at the substitutional positions replacing As and donate electrons. But it is rather surprising that the limit of the electron concentration of around 10^{19} cm^{-3} is a universal feature existing in group VI donors as well, although it is higher than in Si-doped GaAs. The saturation of the electron concentration for chalcogen doped GaAs is due to intrinsic defects, mainly triple negatively

charged gallium vacancies (V_{Ga}) bonded with donors [33]. With increasing doping level, the Fermi energy shifts up towards the conduction band, reducing the formation energy of V_{Ga}. This effect increases the number of V_{Ga}, which compensates the donors and leads to a saturation of the electron concentration [31].

In this work, ion implantation followed by sub-second annealing, in particular millisecond (ms)-range flash lamp annealing (FLA) is used to achieve high doping levels in GaAs. The ultra-doped GaAs layers are prepared by implanting S and Te (as donors), and Zn (as acceptors) ions into intrinsic GaAs wafers. n^{++} doping for GaAs in the range of 10^{19} cm^{-3} has been realized for both S and Te dopants. The highest obtained electron concentration for S doped GaAs reaches 5×10^{19} cm^{-3}, which is much above the equilibrium solid solubility of S in GaAs ($\sim 10^{19}$ cm^{-3}) [31], and it is three orders of magnitude higher than the room-temperature critical carrier concentration of 1.6×10^{16} cm^{-3} required for the insulator-metal transition (IMT) in GaAs [50]. The n^{++}-GaAs (100) layer of around 100 nm thickness exhibits positive magnetoconductance. The magnetoconductance can be well fitted with the Hikami-Larkin-Nagaoka (HLN) model, which allows for the estimation of the phase coherence length (l_ϕ). At 3 K l_ϕ is estimated as large as 540 nm for both S and Te doped GaAs, which is substantially longer than the previously reported values in other semiconductors, e.g. ~ 325 nm in Ge at 1.6 K and ~ 100 nm in ZnO at 5 K [57, 63, 64]. In addition, this unprecedented high electron concentration expectedly meets the requirement for GaAs as a plasmonic material with lower material losses due to a smaller effective mass compared with other heavily doped semiconductors [23].

4.2 Experimental details

Semi-insulating (100) GaAs wafers were implanted at room temperature with S, Te and Zn ions with energies of 55, 160 and 100 keV, respectively. The wafers were tilted by 7° with respect to the ion beam to avoid channeling effect. Before ion implantation, the required ion fluences and the implantation energies, which determine the dopant concentration and distribution in the implanted layer, were calculated using stopping range of ions in matter (SRIM) simulations [100]. Figure 4-1 shows the concentration profiles of Zn, S and Te with the highest fluence in GaAs obtained by SRIM-code simulation. We assumed that the heavily doped layer has the average thickness of about 100 ±10 nm, which corresponds to the ion distribution where the dopant concentration decreases to 10% of the maximum concentration (marked with grey area). The peak concentrations of the implanted dopants are in the range of $3 \times 10^{19} \sim 2 \times 10^{20}$ cm^{-3}. The detailed information about the sample parameters is listed in **Table 4.1**. After ion implantation but prior to FLA, a 100 nm thick SiO$_2$ layer was deposited by plasma

enhanced chemical vapor deposition at 200 ℃. The SiO_2 capping layer was used to prevent the decomposition of GaAs during the high temperature annealing process. After annealing, the capping layer was removed by wet etching in 10% $HF:H_2O$ solution. GaAs samples were annealed by FLA at an energy density of 115 J·cm^{-2} for 20 ms, which corresponds to a peak temperature of about 1100 ℃. The details about the FLA system used to anneal implanted samples and the calculation of the temperature during FLA process can be found in Ref. [101]. Note that millisecond-range annealing can suppress the dopant diffusion in GaAs, which is reported in our previous work [52]. It means that the thickness of doped layer after FLA remains at around 100 nm. The energy difference between the Fermi level and the conduction band (*n*-type) or the valence band (*p*-type) resulting from the band filling in degenerated GaAs is deduced from Eq. (4-6).

TABLE 4.1. Sample definition and related parameters: implantation energy, ion fluence, peak concentration (obtained from SRIM simulation), carrier concentration, and the energy difference between the Fermi level and the conduction band (*n*-type) or the valence band (*p*-type) originated from the band filling in degenerated GaAs based on Eq. (4-6).

Samples ID	Dopants	Energy (keV)	Fluence (cm^{-2})	Peak ion concentration from SRIM ($\times 10^{19}$ cm^{-3})	Measured carrier concentrations ($\times 10^{19}$ cm^{-3})	E_F-E_c (E_v) (eV)
0.07% S	S	55	2×10^{14}	2.9	1.3	0.213
0.16% S	S	55	5×10^{14}	7.2	2.3	0.244
0.32% S	S	55	1×10^{15}	14	5.2	0.281
0.08% Te	Te	160	2×10^{14}	3.7	0.43	0.123
0.21% Te	Te	160	5×10^{14}	9.2	0.69	0.179
0.42% Te	Te	160	1×10^{15}	18.5	3.7	0.272
0.07% Zn	Zn	100	2×10^{14}	3.1	2.9	-0.079
0.17% Zn	Zn	100	5×10^{14}	7.6	6.9	-0.183
0.34% Zn	Zn	100	1×10^{15}	15	10.9	-0.189

The Rutherford backscattering spectrometry (RBS) measurements were performed with a collimated 1.7-MeV He$^+$ beam of the Rossendorf van de Graff accelerator with a 10-20 nA beam current at a backscattering angle of 170°. The crystalline quality of heavily doped GaAs layers before and after FLA were estimated from random and channeling RBS spectra. The channeling spectra were collected by aligning the sample to make the impinging He$^+$ beam parallel to the GaAs [001] axes. The structural properties of implanted and annealed samples were also investigated by micro-Raman spectroscopy. The Raman spectra were collected in a backscattering geometry in the range of 100 to 600 cm^{-1} with the resolution of 0.1 cm^{-1} using a 532 nm Nd:YAG laser and a liquid nitrogen cooled silicon based charge-coupled device camera. The laser power was 3.2 mW and the diameter of the laser spot was 0.8 μm. The spectra are taken in Z(YY)$\underline{Z}$ configuration. The optical properties were investigated by photoluminescence (PL) under a continuous wave green laser (532 nm) excitation with a maximum excitation power up to 10 mW with the diameter of the laser spot of 0.8 μm. The PL signal was collected with a liquid nitrogen cooled InGaAs detector and optical spectrometer with the resolution of 0.2 nm. The focal length of the spectrometers for both Raman and photoluminescence is 800 mm.

Fourier-transform infrared spectroscopy (FTIR) measurements were performed at room temperature using a Bruker Vertex 80v FT-IR system. The electric field distributions in the n^{++} GaAs based antenna were numerically calculated with a commercial software COMSOL Multiphysics using a finite element method. For saving calculation resources, a simplified 2D numerical calculation was performed with electric field polarization parallel to the long axis of the antenna. Floquet periodic boundary conditions were employed for considering a periodic array.

Electrical properties were measured in van der Pauw geometry using a commercial Lakeshore Hall System with a magnetic field perpendicular to the sample plane and swept from -4 T to 4 T in the temperature range of 3-300 K. The electrical contacts for Hall Effect measurements were made by indium. According to current-voltage curves, all contacts were confirmed to be ohmic.
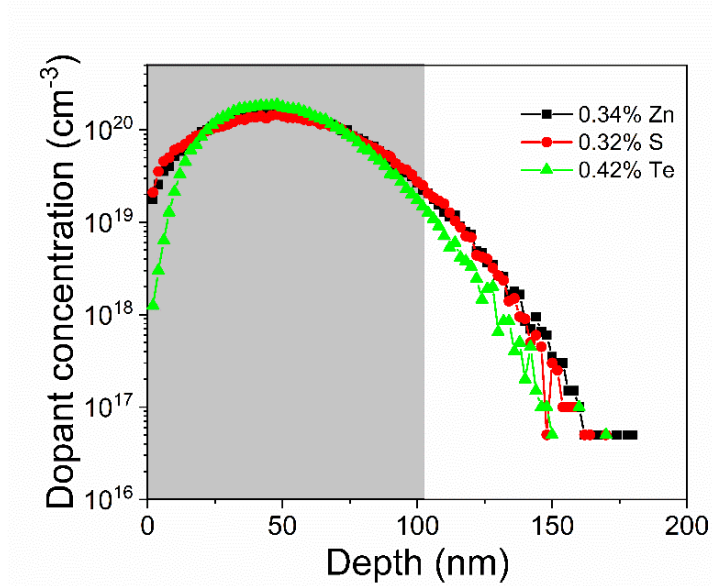
Fig. 4-1. Concentration distribution of Zn, Te and S in implanted GaAs obtained by SRIM code simulation.

4.3 Results and discussion

4.3.1 Structural properties

Figure 4-2 shows the RBS random and channeling (RBS/R and RBS/C) spectra for Zn, S and Te implanted GaAs samples with the highest doses before and after annealing. A non-implanted virgin GaAs is included as the reference. Since RBS/R spectra for all the samples including virgin GaAs are overlapping, only one representative spectrum is shown. The RBS/C spectra for as-implanted samples exhibit a broad damage peak with higher backscattering yields at the sample surface (from 1260 to 1370 keV), which is attributed to lattice damage introduced by the ion implantation. After FLA, the RBS/C of Te-doped sample reveals a minimum backscattering yield χ_{min} (the ratio of the aligned to random yields) of about 11.0 %, which is comparable to the value of 7.8% determined for the virgin GaAs samples. The slightly higher yield χ_{min} can be due to a bit lower crystal quality than the virgin one. The RBS/C spectra obtained from samples doped with S and Zn after annealing overlap with the spectrum of the virgin GaAs in the near surface region, indicating a complete recrystallization of the implanted layer. For virgin GaAs and in samples after annealing, in all RBS/C spectra the Ga (1320 keV) and As (1350 keV) related surface peaks are well-separated, which confirms the formation of high quality layers. The presented results show that the non-equilibrium millisecond-range FLA can effectively recrystallize the ion implanted GaAs without surface decomposition which is otherwise commonly observed after conventional high temperature annealing (above 800 ºC) [116].
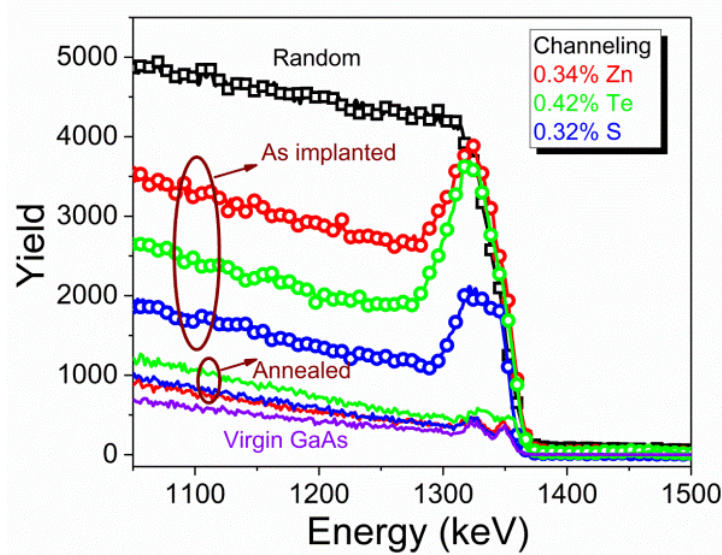
Fig. 4-2. RBS random and channeling spectra obtained from the as-implanted and annealed 0.34% Zn, 0.42% Te and 0.32% S samples. Symbol-lines and solid-lines represent RBS/C spectra for the three as-implanted and annealed samples, respectively. The annealing was performed using FLA at an energy density of 115 J·cm^{-2} for 20 ms.

4.3.2 Plasmonic properties

Figure 4-3(a) and (b) show the normalized Raman spectra from virgin, as-implanted and annealed GaAs samples. The Raman spectra of as-implanted samples (cyan curves) exhibit a broad phonon band, which indicates that the doped layers are totally amorphized. This is in good agreement with RBS results. After FLA, the transverse optical (TO) and longitudinal optical (LO) phonon modes clearly appear for all samples. Due to the selection rules of the Raman scattering, only the LO phonon mode should be detected in (100) GaAs [117, 118], as shown for virgin GaAs in the lower panel of Figure 4-3(a). However, for annealed samples, the observed phonon mode located at the position of the TO phonon (about 268 cm^{-1}) is more prominent than the peak at the LO phonon mode position. This is due to the coupling between the LO phonon mode and the carrier-related plasmon mode, i.e. the coupled LO-phonon plasmon mode (CLOPM) [119-121]. In polar semiconductors like GaAs, the LO phonon couples strongly with the collective oscillations of the free-carrier system (plasmons). Figure 4-3(a) shows the experimental and fitting results using Gaussian deconvolution for Zn-doped GaAs samples. The broadening and the increase of the intensity of the CLOPM mode were observed with increasing doping /carrier concentration. The Stokes Raman scattering rate by the CLOPM mode can be written in the long-wavelength limit by taking into account both the allowed deformation potential and electro-optical contribution as follows [119, 122]:

44

$$I_s(\omega) = A(n_\omega + 1)\frac{[\omega_{TO}^2(1 + C) - \omega^2]^2}{(\omega_{TO}^2 - \omega^2)^2} \times Im[-1/\varepsilon(\omega)] \qquad (4-1)$$

where A is an ω-independent constant factor, n_ω is the Bose-Einstein distribution, C is the Faust-Henry coefficient, ω is the angular frequency, ω_{TO} is the frequency of the TO mode, and $\varepsilon(\omega)$ is the dielectric function, which is given by [122]:

$$\varepsilon(\omega) = \varepsilon_\infty\left[1 + \frac{\omega_{LO}^2 - \omega_{TO}^2}{\omega_{TO}^2 - \omega^2 - i\gamma\omega} - \frac{\omega_P^2}{\omega^2 + i\Gamma_P\omega}\right] \qquad (4-2)$$

where ε_∞ is the high-frequency dielectric constant, ω_{LO} is the frequency of the LO mode, γ is the LO damping factor, and Γ_P is the plasma damping constant. ω_p is the (screened) plasma frequency, which can be obtained by:

$$\omega_P^2 = \frac{ne^2}{m_e^*\varepsilon_\infty\varepsilon_0} \qquad (4-3)$$

where ε_0 is the vacuum permittivity, m_e^* is the average electron effective mass, and n is the electron concentration. For p-type samples, n is replaced by p (hole concentration) and m_e^* is replaced by the heavy hole effective mass m_{hh}^*.

According to the equations 4-1 to 4-3, $I_s(\omega) \propto p$, which explains the increase of the intensity of the CLOPM with increasing dopant concentration. Moreover, the weak TO phonon mode (blue curves) observed in Zn-doped samples is due to the disorder effect originating from the high dose implantation. It causes the breakdown of the Raman selection rules [117, 118].

In the n-type GaAs case, see Figure 4-3(b), the lower branch of the CLOPM mode is located exactly at the TO phonon mode position and is insensitive to the change of the carrier concentration. n-type III-V semiconductors are characterized by high carrier mobilities and low carrier effective masses. In this case, the lower branch (ω_{L-}) and upper branch (ω_{L+}) of CLOPM should be observed. A theoretical model applying for $\omega_{L\pm}$ can be described by equation (4-4) [123].

$$\omega_{L\pm}^2 = \frac{1}{2}(\omega_{LO}^2 + \omega_P^2 + \Gamma_P\gamma) \pm \frac{1}{2}\sqrt{(\omega_{LO}^2 + \omega_P^2 + \Gamma_P\gamma)^2 - 4\omega_P^2\omega_{TO}^2} \qquad (4-4)$$

where the damping constant Γ_P of the plasma oscillation can be written as follows [116]:

$$\Gamma_P = \tau^{-1} = \frac{e}{\mu m^*} \qquad (4-5)$$

where μ is the mobility of the free carriers, and τ is the momentum relaxation time. We assume that the phonon mode observed at the position of the TO phonon mode originates from ω_{L-}, since ω_{L-} reaches the TO phonon energy at high carrier concentration. The upper-frequency mode (ω_{L+}) evolves from a phonon-like to a plasmon-like character with increasing carrier concentration [123, 124], see Figure 4-3(c). The calculated plasma frequencies, using equation (4-3), for p-type and n-type GaAs are also shown in Figure 4-3(c). For Zn-doped GaAs, the CLOPM peak is much broader than for n-type GaAs, due to the higher plasmon damping Γ_P ($\sim$ 700 cm^{-1}) in p-type GaAs. Therefore, in p-type GaAs only one overdamped CLOPM mode is found [121]. Due to the lower effective mass for electrons than for holes, with an identical carrier concentration, the plasma frequency (ω_p) for n-type GaAs is higher than that for p-type GaAs. Hence, the tuning of the plasma frequency is easier in the n-type GaAs. This makes n-type GaAs a potential material for mid-infrared plasmonic chemical sensors [23, 28].
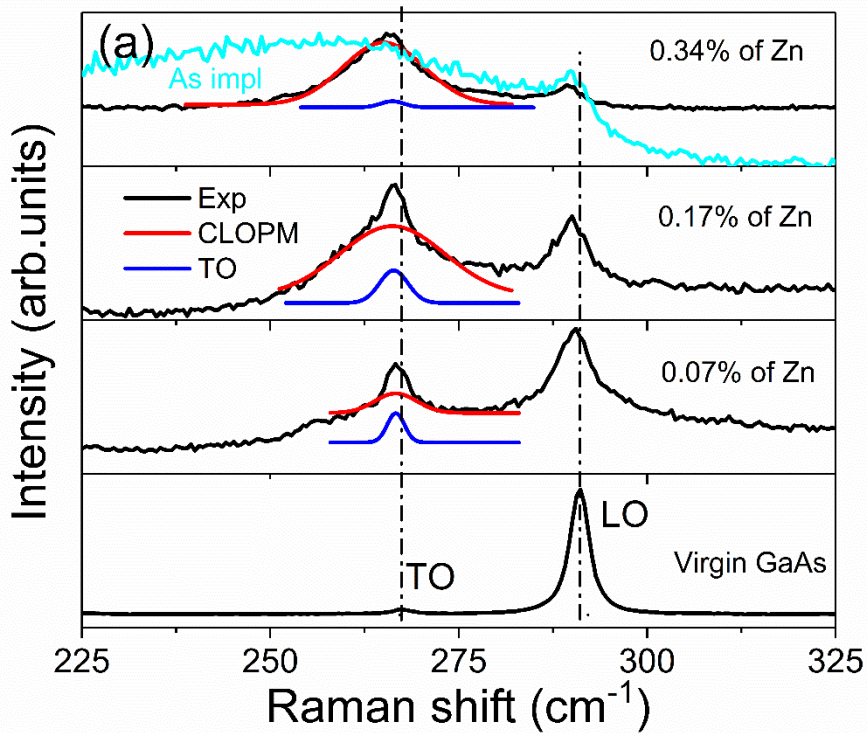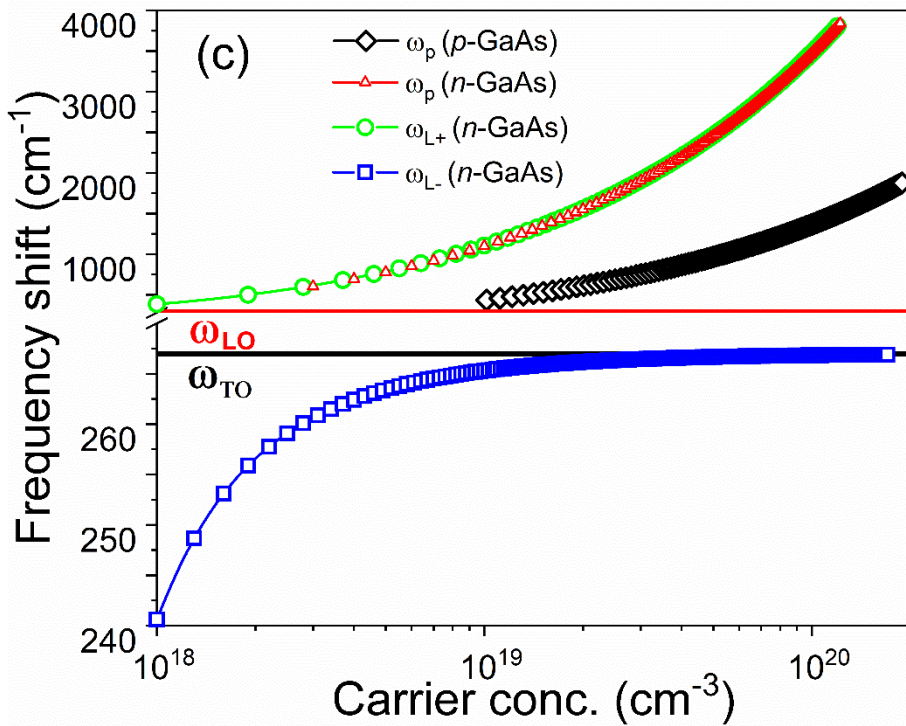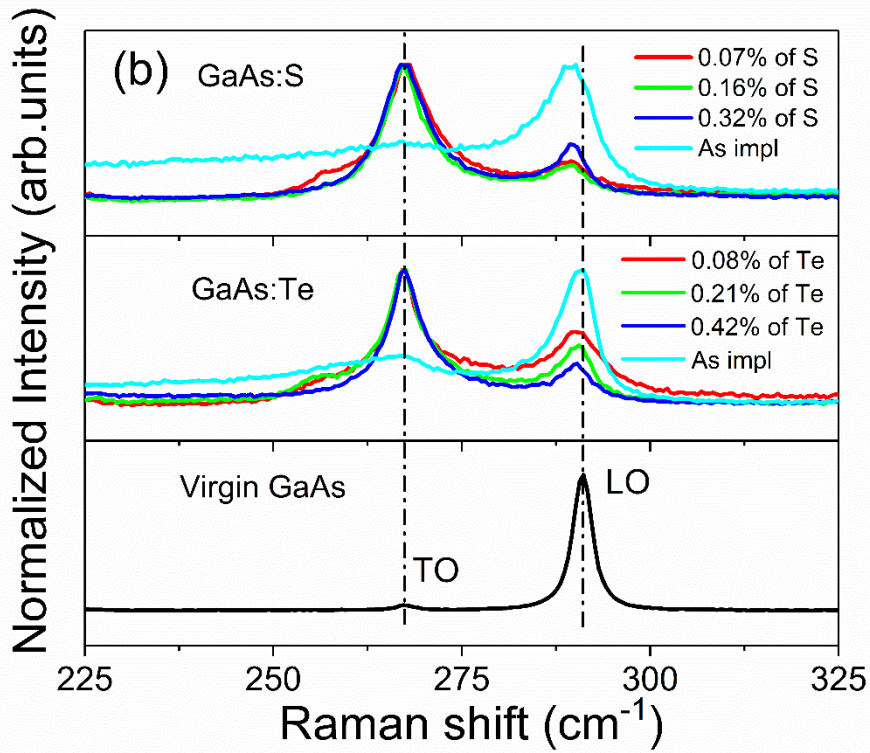
Fig. 4-3. **(a)** and **(b)** show the Raman spectra obtained from virgin, as-implanted and annealed GaAs samples. **(c)** shows the Raman shift of the phonon mode and the plasma frequency ω_p versus concentration for heavily doped p-type and n-type GaAs calculated using eq. 4-3 and eq. 4-4: green circles-upper branch of the CLOPM phonon mode; blue squares-lower branch of the CLOPM phonon mode; black diamonds-plasma frequency for p-type GaAs; red triangles-plasma frequency for n-type GaAs.

47

Figure 4-4(a) shows the reflectivity spectra of n^{++} GaAs samples with different electron concentrations of 7.7×10^{18}, 2.0×10^{19}, 4.0×10^{19} and 7.6×10^{19} cm^{-3}, respectively. Note that the samples here have a thickness of 300 nm in order to get a strong optical signal of implanted layer. The detailed information about the sample parameters is listed in **Table 4.2**. The spectrum of a virgin GaAs wafer is shown for reference. All spectra show an abrupt decrease of reflectivity (plasma edge) and reach a minimum value R_{min} at different wavenumbers between 1400 and 2700 cm^{-1}. More importantly, the plasma frequency is tuned to higher wavenumber by increasing carrier concentration of GaAs, which is in agreement eq. 4-3. The spectra shown in Fig. 4-4(a) indicate the lowest damping factor for sample 4, which can be explained by the highest dopant activation efficiency and lowest defect concentrations.

We explore the application of such highly-doped plasmonic GaAs by numerically modeling the response of antenna structures based on this material. Single-arm plasmonic antennas are modeled with COMSOL Multi-physics 2D simulation. The target material in this simulation is sample 4 with electron concentration of 7.6×10^{19} cm^{-3}. The electric field polarization is parallel to the antenna axis. The height of the antenna is fixed to 0.3 μm. The antenna length sizes vary from 0.8 to 5 μm and the incident wavelengths sweep from 17 to 50 μm (200-580 cm^{-1}). The simulated reflection spectra are presented in Figure 4-4(b). Two surface plasmon resonances labeled with R1 and R2 are clearly observed, experiencing a red shift and becoming broader with increasing the antenna length. It is due to the retardation effects, including both the polaritonic red shift and the increased radiation damping resonance with increasing long-arm sizes [125, 126].

Each resonance corresponds to specific modes in the near-field. Fig. 4-4 (c) and (d) present the electric field distribution for L=2 μm with the incident wavelength λ corresponding to 20 and 35 μm, respectively. The high field intensity, or the so-called hot spots, is located at the n^{++} GaAs/substrate interface for λ= 20 μm, marked as resonance 1 (*R1*), as seen in Fig. 4-4(c). Fig. 4-4(d) shows the hot spots located in the whole short edge of the antenna near both the n^{++} GaAs/substrate and n^{++} GaAs/air interfaces, labeled as resonance 2 (*R2*). The electric field enhancement suggests that n^{++} GaAs is promising for a high sensitivity plasmonic application in Mid-infrared range.

TABLE 4.2. Sample definition and related parameters: implantation energy, ion fluence, peak concentration (obtained from SRIM simulation), annealing parameters, carrier concentration obtained from Hall effect measurement.

Samples ID	Dopants	Energy (keV)	Fluence (cm^{-2})	Peak ion concentration from SRIM ($\times 10^{19}$ cm^{-3})	Laser energy density of pulsed laser annealing (J/cm^2)	Measured carrier concentrations ($\times 10^{19}$ cm^{-3})
S1	S	200	9.9×10^{14}	5	0.6	1.3
		70	2.8×10^{14}			
S2	S	200	2.1×10^{15}	50	0.7	2.3
		70	5.6×10^{14}			
S3	Te	480	6.5×10^{15}	50	0.6	5.2
		200	1.2×10^{15}			
		100	1.0×10^{15}			
S4	Te	480	6.5×10^{15}	50	0.7	5.2
		200	1.2×10^{15}			
		100	1.0×10^{15}			

Fig. 4-4. **(a)** Room-temperature reflectance of n^{++} GaAs samples with different electron concentrations: 7.7×10^{18}, 2.0×10^{19}, 4.0×10^{19} cm^{-3} and 7.6×10^{19}. The reflectance spectrum of non-intentionally doped GaAs is shown for reference. Dotted-lines are the fitting results obtained from a multilayer model based on transfer matrix method. From the fitting results, plasma frequency (ω_p) defined as the zero-crossing frequency of function real part of permittivity (ε') can be tuned from 745 to 1740 cm^{-1}. **(b)** Mid-infrared plasmon resonances in sample 4 based single arm antenna simulation with COMSOL. The simulated reflection spectra with varying the arm length and incident wavelength indicates two resonance labeled with R1 and R2. **(c)** and **(d)** Electric field distribution of sample 4 based single-arm antenna; the incident wavelength is 20 and 35 μm, respectively.

4.3.3 Photoluminescence

Figure 4-5 shows the normalized room-temperature PL spectra obtained from GaAs samples doped with 0.32% S, 0.42% Te or 0.34% Zn after green laser excitation. The PL spectrum of virgin GaAs is shown for reference. The penetration depth of the green laser in GaAs is deeper than the thickness of the doped layer, therefore the presented PL spectra are a superposition of the PL emission collected from the top implanted layer and from the undoped substrate. The

PL emission from the undoped substrate is expected to be located at the same position as that observed from virgin GaAs. After deconvolution of the PL spectra with two Gaussian peaks, the PL emission from the doped and undoped layers can be distinguished, as visualized with shadow areas and green dash-dot lines (see Figure 4-5). The substrate peaks labeled with green lines are in different positions for three doped samples, which could be related to the doping induced strain effect. Note that the peak at about 900 nm from the *n*-type GaAs layer is attributed to defect-related emission [127]. It is clearly visible that the peak positions of the 0.32% S- and 0.42% Te-doped samples exhibit a blue shift with respect to the virgin GaAs (see the violet area in Fig. 4-5). On the contrary, the 0.34% Zn doped sample shows a red shift (see the red area in Fig. 4-5). The blue shift in *n*-type GaAs is mainly due to the filling of the conduction band with carriers leading to the Fermi level upshift above the conduction band minimum. Likewise, in *p*-type GaAs, the Fermi level downshifts below the valence band maximum. The energy difference between the Fermi level and the conduction band (or valence band) follows the equation (4-6) [55]:

$$E_F - E_C\,(E_V) = \frac{\hbar^2}{2m_e^*}(3\pi^2 n)^{2/3} \quad (4\text{-}6)$$

where n is the free carrier density and m_e^* is the electron effective mass. For *p*-type samples, n is replaced by p (hole concentration) and m_e^* is replaced by the heavy hole effective mass m_{hh}^*. The calculation results are listed in **Table 4.1**. Taking into account the position of the Fermi level, all the doped samples are degenerate semiconductors expecting to show metallic-like behavior.
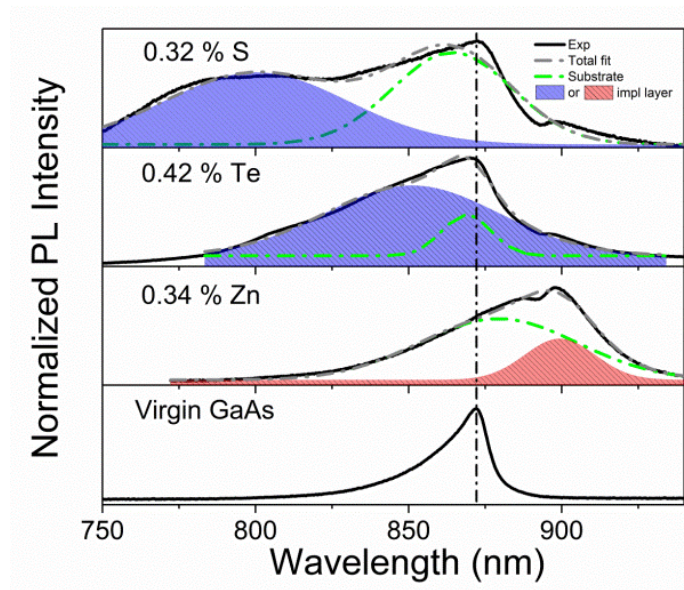
Fig. 4-5. Normalized room-temperature PL spectra obtained from 0.32% S, 0.42% Te or 0.34% Zn samples. The PL spectrum of virgin GaAs is shown for comparison.

High-level doping can also induce bandgap narrowing, which lowers the electron energies as compared to a non-interacting carrier system. The spatially redistributed electrons reduce the long-range Columbic interaction energy. As a result, the interaction energy reduces the total energy of the electron system. The change in energy gap follows a 1/3 power law of the doping concentration, $\Delta E_g \propto n^{1/3}$[32] . The bandgap narrowing causes the downshift of the conduction band minimum. However, the band filling effect in *n*-type GaAs prevails causing the blue shift of the PL peak position [128, 129]. The red shift of the PL emission in heavily doped *p*-type GaAs (the radiative recombination of heavy holes and free electrons) is dominantly attributed to the bandgap narrowing effect, leading to the decrease of emitted photons energy [32, 54, 55, 130-132].

4.3.4 Transport properties

Figure 4-6 (a) shows the carrier concentration at 300 K as a function of dopant concentration obtained from Zn, S and Te implanted GaAs followed by FLA. In the case of *p*-type GaAs (Zn doped), the highest hole concentration is 10.9×10^{19} cm^{-3}, while the maximum electron concentration for *n*-type GaAs doped with S is as high as 5.2×10^{19} cm^{-3}. High *p*-type doping of GaAs is easier than *n*-type doping. On one hand, this is due to the higher solid solubility of acceptors than donors in GaAs. On the other hand, the higher formation energy for V_{As} in *p*-type GaAs than V_{Ga} in *n*-type GaAs decreases the probability for the formation of acceptor-vacancy (e.g. Zn-V_{As}) complexes compared with the formation of donor-vacancy complexes (e.g. S-V_{Ga}) [31, 133]. This is in agreement with previous reports that high hole concentrations can be relatively easily achieved in GaAs. For example, using Be as the acceptor in GaAs, hole concentration as high as 10^{21} cm^{-3} is possible [37]. Therefore, the much higher hole concentration obtained from Zn-doped GaAs compared to the electron concentration measured from S or Te doped GaAs is not surprising.

The effective Bohr radius of shallow-donor bound electrons in *n*-type GaAs with effective mass of 0.067 m_e is a_B =103 Å and the critical concentration of donors for IMT in GaAs at room temperature is n_c=1.6×10^{16} cm^{-3} [50]. That means that all the investigated *n*-type GaAs samples are highly degenerate semiconductors and supposed to exhibit metallic behavior. Since the larger effective mass leads to smaller Bohr radii ($m^* \propto \frac{1}{a_B}$), for the Zn-doped *p*-type GaAs, the effective Bohr radius is about 15.6 Å. The critical hole concentration for IMT at room temperature in *p*-type GaAs is around 4.1×10^{18} cm^{-3}, based on the Mott theory of the IMT as described by equation (4-7) [32, 49].

$$n_c^{1/3} a_B = 0.26 \pm 0.05 \qquad (4-7)$$

where a_B is effective Bohr radius, and n_c is the critical electron concentration. Therefore, the presented *p*-type GaAs samples are expected to be also degenerate semiconductors like *n*-type GaAs.
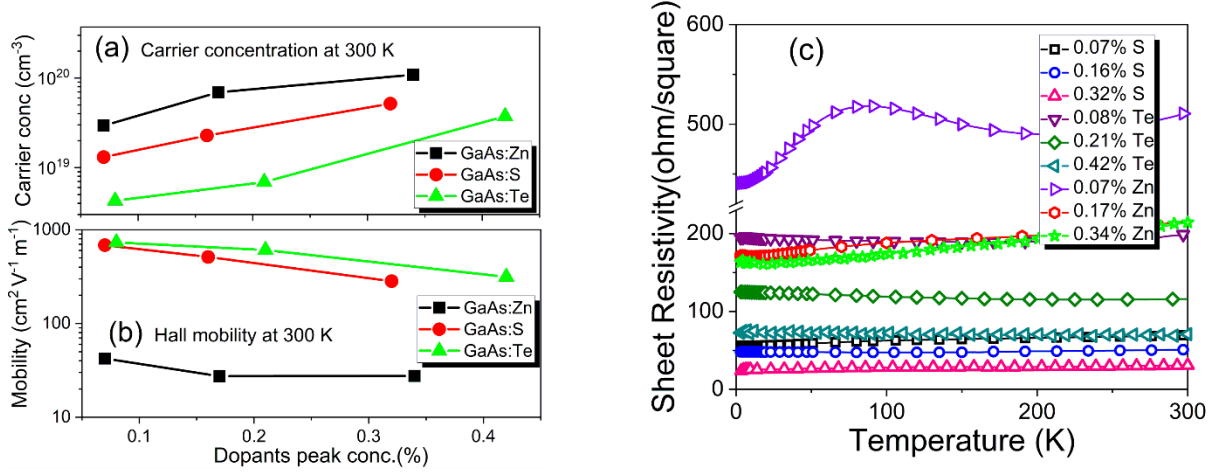
Fig. 4-6. **(a)** The carrier concentration and **(b)** the Hall mobility at 300 K as a function of dopant concentration obtained from implanted GaAs followed by FLA. **(c)** Temperature-dependence of the sheet resistance of doped GaAs in the temperature range of 3 K to 300 K.

Figure 4-6(b) shows the carrier mobility at 300 K as a function of dopant concentration. The mobility for *n*-type GaAs and *p*-type GaAs is in the range of 283~733 and 42~28 cm²/(V·s), respectively. The decrease of the carrier mobility with increasing carrier concentration is mainly attributed to electron-electron scattering and carrier scattering by the impurities, which is typical for heavily doped semiconductors [134]. Figure 4-6(c) shows the temperature-dependence of the sheet resistance obtained from implanted GaAs followed by FLA. *p*-type GaAs with the lowest Zn concentration (0.07% Zn) exhibits a different behavior from other samples. This is due to the lower hole concentration. The other samples show nearly temperature-independent sheet resistivity as expected for degenerate semiconductors.

Figure 4-7 shows the magnetoconductance of *n*-type and *p*-type GaAs samples. The conductance data is described by equation (4-8) and shows the change in the conductivity of measured sample under magnetic field (*G(B)*) relative to the zero field (*G(0)*) conductivity.

$$\Delta G = G(B) - G(0) = \frac{1}{\rho(B)} - \frac{1}{\rho(0)} \qquad (4-8)$$

where ρ(0) and ρ(B) are the resistivity of measured samples without and with magnetic field. Obviously, at low temperature, the *n*-type GaAs samples show PMC at low magnetic field (< 0.3 T), while *p*-type GaAs exhibits negative MC in the whole magnetic field range. The theory of PMC is extensively studied for heavily doped semiconductors [110, 135]. In weakly

disordered semiconductors, it is explained that the multiple random elastic scattering of electrons from impurities leads to the quantum interference phenomena [57, 106]. Quantum interference can introduce the WL effect, which significantly influences the temperature dependent electron transport mechanisms. WL arises because of the self-interference of time-reversed electronic waves backscattered from impurities. It leads to an enhanced probability of carrier backscattering, and therefore results in an enhanced resistivity. The magnetic field applied normal to the plane of carrier motion breaks the time reversal symmetry, and suppresses the weak localization, leading to a PMC or named negative magnetoresistance (NMR). Note that in n-type GaAs, the weak localization corrections were first developed in the limit of weak disorder, when $k_F l \gg 1$ (k_F is the Fermi wavelength, and l is the mean free path). For our n-type GaAs shown in this manuscript, $k_F l = 11\text{-}26$ (estimated from the free-electron theory, $k_F l = \hbar(3\pi^2)^{2/3}/e^2\rho n^{1/3}$) [136].

There are alternative two- and three-dimensional fitting models for n-type GaAs. The 3-D model can be written as [106]:

$$\frac{\Delta\rho}{\rho} = -\alpha\rho\frac{e^2}{2\pi^2\hbar}\sqrt{\frac{eB}{\hbar}}F(x) \qquad (4\text{-}9)$$

where $\frac{\Delta\rho}{\rho}$ is the fractional change in resistivity due to the applied magnetic field, α is a coefficient between 0 and 1 that is thought to represent the Coulomb screening, e is the elementary electronic charge, $\hbar$ is Planck's constant, B is the applied magnetic field, and ρ is the resistivity. F(x) is the Hurwitz zeta function given by [137]:

$$F(x) = \sum_{n=0}^{\infty}\left[2(n + 1 + 1/x)^{1/2} - 2(n + 1/x)^{1/2} - (n + 1/2 + 1/x)^{-1/2}\right] \quad (4\text{-}10)$$

where x is a dimensionless quantity defined by $x = 4eD\tau^*B/\hbar$, D is the electron diffusion constant, τ^* is the electron inelastic-scattering lifetime, and the phase coherence length $l_\phi = \sqrt{D\tau^*}$. In the high magnetic field regime (> 0.3 T), MC is dominated by the parabola-like (B^2) dependence, originating from the Lorentzian deflection of carriers under perpendicular magnetic field. The electron executes cyclotron orbits, thereby shortening the mean free path, and thus decreasing the conductance [138]. We accounted for this by fitting the transport data. However, the fitting quality provides a worse description to experimental results, as exemplarily shown in Figure 4-7(b) with the orange line for 0.42% Te.

Using the Hikami-Larkin-Nagaoka (HLN) 2D model [60, 63, 139]:

$$\Delta G\left(B\right) = \beta \frac{e^2}{\pi h}\left[\Psi\left(\frac{1}{2} + \frac{B_\phi}{B}\right) - ln\left(\frac{B_\phi}{B}\right) + 2\,ln\left(\frac{B_\phi + B_{SO}}{B}\right) - 2\Psi\left(\frac{1}{2} + \frac{B_\phi + B_{SO}}{B}\right) - \right.$$
$$\left. \Psi\left(\frac{1}{2} + \frac{B_\phi + 2B_{SO}}{B}\right) + ln\left(\frac{B_\phi + 2B_{SO}}{B}\right)\right] \qquad (4\text{-}11)$$

where $\Psi(x)$ is the digamma function of a physical variable x [140] and β is a constant of 1 (or -1/2) corresponding to weak localization (weak anti-localization). $B_\emptyset = \frac{\hbar}{4el_\emptyset^2}$ is a magnetic field defined by a phase coherence length l_ϕ $(l_\phi = \sqrt{D\tau_\phi})$. $B_{so} = \frac{\hbar}{4el_{so}^2}$ is the characteristic magnetic field defined by the spin-orbit length l_{so}, which can lead to weak anti-localization effect. Since at high magnetic field the conductance is dominated by the large quadratic background (B^2 dependence) from the Lorentz force, the final fitting of the conductivity was performed using equation (4-12).

$$\Delta G\left(B\right)_{FIT} = \Delta G\left(B\right)_{HLN} + CB^2 \quad (4\text{-}12)$$

where C is a measurement temperature related parameter [63], while in the fitting process of temperature range of 3-80 K, it keeps nearly constant.

The solid curves in Figures 4-7(a) and (b) correspond to the fits with Eq. (4-12). The theory of weak localization in two-dimensional provides an excellent description of the transport results. Figure 4-7(c) shows the magneto-transport data obtained from p-type GaAs exhibiting the negative MC. This phenomenon is commonly explained by weak anti-localization originating from spin-orbit coupling, which has already been reported in heavily doped p-type Ge [63], and in some topological insulator materials [141]. However, by fitting the transport curve of the p-type GaAs using Eq. (4-12), we found that l_{so} is negligibly small compared to l_ϕ, which excludes the assumption that the negative MC in p-type GaAs can be attributed to the strong spin-orbit coupling. Here, the negative magnetoconductivity in p-type GaAs is attributed to the Lorentzian force instead of a weak-antilocalization.

Figures 4-7(d) and (f) show the phase coherence length and spin-orbit length as a function of carrier concentration at 3 K. As expected, the phase coherence length is comparable or larger (80~540 nm) than the thickness of the doped layer (100 nm), confirming that the system is quasi-two dimensional and justifies the use of HLN model.
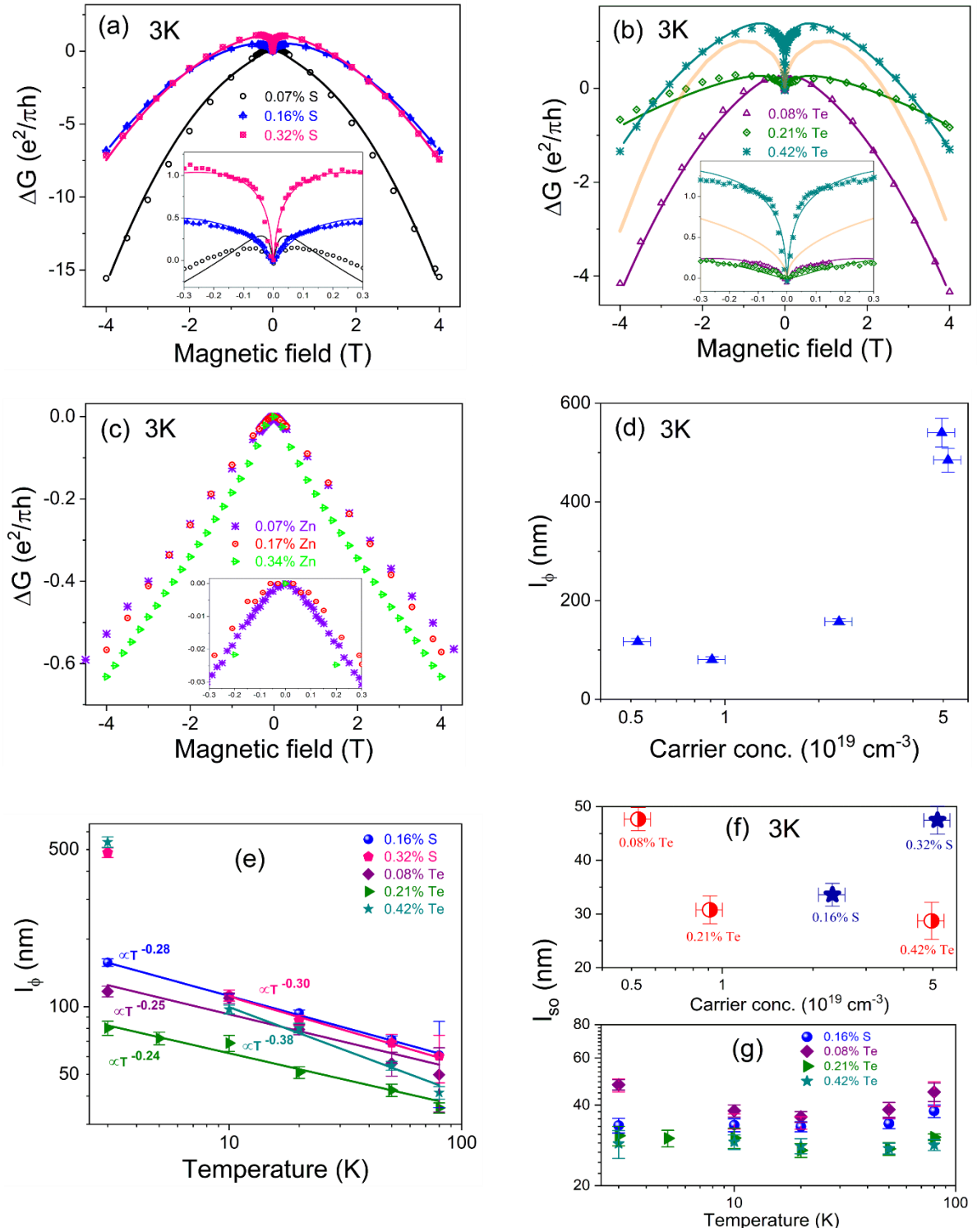
Fig. 4-7. Magneto-transport properties in heavily doped GaAs samples. **(a)**, **(b)** and **(c)** show the MC measured at 3K for GaAs:S, GaAs:Te and GaAs:Zn samples with different doping concentrations. Symbols are experimental points and solid lines are fitting results based on weak localization theory using the HLN model, Eq. (4-12). The orange line in Figure (b) shows the 3-D model fitting result for 0.42% Te. **(d)** and **(f)** show the phase coherence length $l_\emptyset$ and the spin-orbit length l_{so} at 3 K for *n*-type GaAs as a function of carrier concentration. **(e)** and **(g)** show the temperature dependent phase coherence length $l_\emptyset$ and spin-orbit length l_{so}, respectively.

56

The electron dephasing time τ_ϕ corresponds to 0.5-38 ns with l_ϕ varying from 80 to 540 nm. The error bars for the phase coherence length and the spin-orbit length in Figure 4-7 indicate the 95% confidence intervals of the fits. The 10% percent inaccuracy of the carrier concentration is due to the inaccuracy in determining the thickness of the doped layer. For the 0.07 % S sample, we are unable to extract a proper phase coherence length and spin-diffusion length owing to the bad quality of the experimental data fittings, thus the discussion will focus on the rest of the *n*-type GaAs samples.

Figure 4-7(d) shows that l_ϕ increases from 80 to 540 nm with increasing the electron concentration from 5×10^{18} to 5×10^{19} cm^{-3}. Similarly, an enhancement of l_ϕ with increasing carrier concentration by applying back gating voltage is reported in low dimensional systems. Koester *et al*. have reported that in Si/Si$_{0.7}$Ge$_{0.3}$ quantum wells, at 1.3 K the phase coherence length can be tuned from 170 to 690 nm by increasing sheet electron concentration from 4.15×10^{11} to 4.85×10^{11} cm^{-2} [142]. Premasiri *et al*. have showed that for a multilayer indium monoselenide (InSe), at 2.2 K l_ϕ increases from 40 to 65 nm as the back gating voltage increases from 23 to 48 V, corresponding to an increase in sheet electron concentration from 3×10^{12} to 13×10^{12} cm^{-2} [143]. The increase of l_ϕ is commonly attributed to the enhanced diffusion parameter and the increased Fermi velocity [144]. Figure 4-7(e) illustrates temperature dependent l_ϕ, which decreases with increasing temperature and follows $l_\phi \propto T^\eta$ power law. The reported value $\eta = $ -1/2 is ascribed to the dephasing mechanism being related to electron-electron collision with small energy transfer (or the 'Nyquist dephasing') in 2D systems [144, 145]. Since the electron-phonon scattering also plays a role in the inelastic scattering mechanism in heavily doped n-type GaAs, it could explain the value of η between -0.24 and -0.38 as shown in Figure 4-7(e). Moreover, the phase coherence length of about 540 nm for samples 0.42% Te and 0.32% S at 3 K could not fit with this power law, which may be related to the stronger screening of charged impurities at electron concentration reaching 5×10^{19} cm^{-3} [64]. It means electrons can obtain a longer phase memory before they are scattered by impurities, leading to an enhanced weak-localization for samples 0.42% Te and 0.32% S at 3 K. The l_ϕ as large as 540 nm at 3 K in this study is comparable with the values obtained in Si/Si$_{0.7}$Ge$_{0.3}$ quantum well systems [142], which is desirable for quantum device applications.

Figure 4-7(f) show the extracted l_{so} in the range of 29-48 nm for five heavily doped n-type GaAs samples. For Te doped GaAs, it shows a decreased l_{so} with increasing the electron concentration. This is due to the reduced spin relaxation time τ_{so} since $l_{so} = \sqrt{D\tau_{so}}$. Dzhioev *et al*. have studied the spin relaxation time in GaAs by the optical orientation method [146]. It

was found that τ_{so} decreases with increasing electron concentration in the metallic regime. With increasing the donor concentration from 10^{16} to 10^{19} cm^{-3}, the spin relaxation time decreases from 100 to 0.04 ns. Using $l_{so} = \sqrt{D\tau_{so}}$, we have estimated τ_{so} in our Te-doped GaAs in the range of 0.06 and 0.18 ns. The decrease of τ_{so} was explained by Dyakonov-Perel (DP) spin dephasing mechanism [146]. It applies to materials without the inversion symmetry, like groups III-V (such as GaAs) and II-VI (ZnSe) compound semiconductors, where the inversion symmetry is broken by the presence of two distinct atoms in the Bravais lattice. However, in our case Figure 4-7(g) illustrates that at temperature range of 3-80 K, l_{so} for n^{++} GaAs is insensitive to temperature, which suggests spin precession is due to carrier collisions with phonons or impurities named Elliott-Yafet (EY) spin relaxation mechanism instead of DP mechanism [147]. J. M. Kikkawa and D. D. Awschalom also reported that the EY mechanism dominates the spin precession process in n-type GaAs below 30 K [148]. For S doped GaAs, l_{so} is generally larger at a similar electron concentration. Since heavier elements have stronger spin-orbit coupling (SOC), GaAs:Te gives rise to a shorter spin relaxation time than in GaAs:S. This explains the different behavior of l_{so} for GaAs:Te and GaAs:S samples.

4.4 Conclusion

In summary, heavily doped GaAs samples synthesized by ion implantation followed by non-equilibrium annealing process are systematically investigated regarding their electrical and optical properties. We have shown that weak localization is responsible for the positive magnetoconductance in n-type GaAs samples. By fitting the magnetotransport data with the HLN model, the extracted phase coherence length and the spin-orbit length are as large as 540 and 48 nm, respectively, implying heavily doped GaAs as a potential material for quantum devices and spintronic application. Moreover, the unprecedented high electron concentration (5×10^{19} cm^{-3}) extends the possibilities of using GaAs as chemical sensors based on plasmonic effect.

Chaper 5 Enhanced trion emission in monolayer MoSe$_2$ by constructing a type-I van der Waals heterostructure

Trions, quasi-particles consisting of two electrons combined with one hole or of two holes with one electron, have recently been observed in transition metal dichalcogenides (TMDCs) and drawn increasing attention due to potential applications of these materials in light-emitting diodes, valleytronic devices as well as for being a testbed for understanding many-body phenomena. Therefore, it is important to enhance the trion emission and its stability. In this study, we create a MoSe$_2$/FePS$_3$ van der Waals heterostructure (vdWH) with type-I band alignment, which allows for carriers injection from FePS$_3$ to MoSe$_2$. At low temperatures, the neutral exciton (X^0) emission in this vdWH is almost completely suppressed. The I$_{Trion}$/I$_{x0}$ intensity ratio increases from 0.44 in a single MoSe$_2$ monolayer to 20 in this heterostructure with the trion charging state changing from negative in the monolayer to positive in the heterostructure. The optical pumping with circularly polarized light shows a polarization for trion emission in MoSe$_2$/FePS$_3$ of 14%. Moreover, forming such type-I vdWH also gives rise to a 20-fold enhancement of the room temperature photoluminescence from monolayer MoSe$_2$. Our results demonstrate a novel approach to convert excitons to trions in monolayer 2D TMDs via interlayer doping effect using type-I band alignment in vdWH.

5.1 Introduction

Two-dimensional (2D) transition metal dichalcogenides (TMDCs), MX_2 (M=Mo, W; X=S, Se, Te) with a hexagonal crystal structure are an exciting class of materials [2-4]. Monolayer TMDCs feature a direct bandgap, a large binding energy of neutral exciton (X^0) of up to several hundred meV because of the reduced dielectric screening, valley-selective optical coupling due to the lack of inversion symmetry and a strong spin-orbit coupling [1]. Excitons in TMDCs can often trap an electron (X^-) or a hole (X^+) to form so-called trions [1, 75, 149, 150]. With these exotic features and tunable bandgaps from visible to near-infrared regions, TMDCs are considered as a highly desired material class for the next generation optoelectronic and valley-based electronic applications [151].

Stacking 2D layered materials with pre-selected properties will give rise to the formation of van der Waals heterostructures (vdWHs) with atomically sharp and near-defect-free interfaces, which may exhibit novel physics and possess versatile properties [5-7]. So far, the most extensively studied TMDC vdWHs include MoS_2-$MoSe_2$ [152], MoS_2-WS_2 [153, 154], MoS_2-WSe_2 [155, 156], $MoSe_2$-WSe_2 [88], $MoSe_2$-WS_2 [157] and WS_2-WSe_2 [158]. Their band alignment is found to be staggered type-II, where the conduction band minimum (CBM) and valence band maximum (VBM) are located in the wider-bandgap (WBG) and narrower-bandgap (NBG) materials, respectively. Electrons and holes can be spatially separated, which results in the formation of the interlayer excitons and consequently in quenching of the photoluminescence (PL) in their component layers [153].

However, the type-I band alignment, which is common in conventional semiconductor heterostructures like GaAs-AlGaAs, is very rarely reported in vdWHs. The CBM and VBM of type-I band alignment are both located in the NBG layer [159]. Therefore, in the heterojunction with type-I band alignment, carriers will flow only from the WBG to the NBG material. Consequently, in the NBG layer, the carrier concentration increases and its PL intensity is enhanced [94-96]. Nevertheless, besides the use of hexagonal boron nitride (h-BN) for passivation, up to now only a few implementations of the type-I band alignment in 2D materials, like PbI_2/WS_2 [94] and MoS_2/ReS_2 [159], MoS_2/ZnO-QDs [160], have been reported. Those papers focus on the charge transfer process at the interface, which leads to a PL enhancement of the NBG layer. However, trion and exciton emission behavior in type-I vdWH with TMCDs has not yet been investigated. The conversion from excitons to trions controlled by charge density can influence the exciton lifetime and leads to a large valley polarization via valley-selective optical pumping [161]. Since in straddling bands carriers flow only in one direction,

by proper selection of WBG materials (*n*-type or *p*-type) the charging state of trion can be controlled. Moreover, positively charged trions, X^+, have a much longer dephasing time than negatively charged trions, X^- and thus a smaller linewidth, which makes them attractive for quantum technology [162].

In this work, we demonstrate the manipulation of the trion charging state and population in monolayer $MoSe_2$ by constructing a vdWH $MoSe_2/FePS_3$ with type-I band alignment. $FePS_3$ with an indirect bandgap is chosen as the WBG semiconductor. The type-I band alignment is supported by density-functional theory (DFT) calculation, such that $MoSe_2$ with the narrower bandgap acts as the carrier extraction layer and *p*-type $FePS_3$ is a source of holes. We have achieved an enhancement of the trion emission with the I_T/I_{X0} ratio increasing from 0.44 to 20, and a 20-fold enhancement of PL emission from the $MoSe_2$ monolayer due to carrier injection from $FePS_3$. Moreover, both the exciton emission in a single $MoSe_2$ monolayer and the trion emission in $MoSe_2/FePS_3$ depend on the chirality of the excitation light, indicating the valley polarization selectivity. Our study provides essential insight into the underlying carrier transport mechanism and points to potential device application based on type-I band alignment vdWH.

5.2 Experimental Section

Sample preparation

The 2D material flakes were mechanically exfoliated through blue tape and then transferred onto SiO_2/Si substrates (90 nm thick SiO_2 on heavily doped Si) by using a polymer stamp transfer technique within a nitrogen atmosphere in a glove box environment. This technique provides good crystalline quality, intact atomic interfaces and less contamination of the flake in comparison with other transfer techniques [163]. Also, pre-patterned electrodes with Ti/Au (5/45nm) on SiO_2/Si substrates were fabricated by standard photolithography and electron-beam evaporation processes. To fabricate the $MoSe_2/FePS_3$ vdWH, $FePS_3$ was first transferred onto the SiO_2/Si substrate, and then the monolayer $MoSe_2$ was transferred onto the top of the $FePS_3$ flake. For reference, the single $MoSe_2$ monolayer flakes were prepared in the same way. Finally, both the vdWH and single $MoSe_2$ flakes were covered with h-BN in order to reduce flake contamination and degradation resulting from contact with air.

Characterization

For the micro-PL and micro-Raman measurements, we used a cw frequency-doubled Nd:YAG laser for excitation at a wavelength of λ=532 nm. The laser power was controlled by introducing neutral density filters. The maximum laser power used here was 3.2 mW to avoid heating of the flake. The spot diameter of the laser on the sample was approximately 3 μm, i.e., smaller than the size of the target flakes. Both PL and micro-Raman investigations were performed in the temperature range from 4 to 300 K using a liquid-He cooled chamber and temperature controller. A liquid nitrogen-cooled Si-CCD camera was used to detect the PL emission, which is dispersed in a spectrometer. To check the PL polarization of trion and exciton in $MoSe_2$, the excitation with circular left-(right-) handed polarized light was performed. The measurement was done at 4 K. The thickness of $FePS_3$ is measured with atomic force microscopy (*AFM*) with a Bruker Multimode 8 system, and the thicknesses of $MoSe_2$ were estimated by optical contrast and confirmed by micro-Raman, PL results.

Calculation details

Calculations are done by M. Ghorbani-Asl and A. V. Krasheninnikov.

Spin-polarized density functional theory (DFT) calculations were performed in the framework of the projector augmented wave method using the Vienna Ab initio Simulation Package (VASP) code [164]. The generalized gradient approximation (GGA) with the Perdew-Burke-Ernzerhof (PBE) parametrization was used for the exchange-correlation functional [165]. To account for the strong correlation effects among d-orbital electrons of iron atoms, the DFT + U method with an effective Hubbard value (U) of 4.5 eV for Fe atoms was employed. The plane-wave basis set with a kinetic energy cutoff of 600 eV was used. The Brillouin zone of the system was sampled using $8 \times 8 \times 1$ *k*-mesh for primitive cells and $5 \times 5 \times 1$ *k*-mesh for supercells. London dispersion interactions were included in the total energy as proposed by Grimme in the DFT-D2 method [166]. The geometry optimization was carried out until the atomic forces were less than 0.01 eV/Å. A vacuum layer of 20 Å perpendicular to the basal plane was introduced to implement the isolated slab condition. In order to adopt zigzag antiferromagnetic ordering in $FePS_3$, a unit cell of tetragonal shape with 20 atoms was considered, as shown in Figure 5-2(a). The heterostructures were constructed by using an interface consisting of 1×1 unit cell of $FePS_3$ and 1×3 unit cells of monolayer $MoSe_2$ corresponding to a lattice mismatch of only 0.6%. The supercells contain 38 atoms in 2 layers and 74 atoms in 4 layers ($MoSe_2$ triple layers+ $FePS_3$ monolayer) configurations.

## 5.3 Results and discussion

5.3.1 Raman results

Figure 5-1(a) shows the schematic configuration of $MoSe_2$/$FePS_3$ vdWH covered with a few layers of h-BN. Except protecting samples from air, the h-BN encapsulation also reduces the linewidth of the trion and exciton emission from the $MoSe_2$ monolayer [162]. The $MoSe_2$ monolayer was fully laying on the top of $FePS_3$ and the heterostructure area is around 100 μm^2 which is much larger than the laser spot size (about 7 μm^2). Therefore, all the optical signals (including micro-Raman and micro-PL) are coming from the heterojunction. For the reference, individual $MoSe_2$ monolayers and $FePS_3$ flakes covered with h-BN were prepared as well. Figure 5-1(b) shows the optical microscope image of $MoSe_2$/$FePS_3$ vdWH, where regions with magenta and orange outlines represent $FePS_3$ and $MoSe_2$, respectively.

Figure 5-1(c) and (d) show the Raman spectra of monolayer $MoSe_2$ combined with 22 nm (corresponding to 31 layers) $FePS_3$, defined as 1ML $MoSe_2$/31ML $FePS_3$, multilayer $FePS_3$, and individual $MoSe_2$ flakes with different thicknesses (1ML, 2ML and multilayer). For $MoSe_2$, the A_{1g} mode is an out-of-plane vibration modes in which Se atoms in all layers oscillate in phase with reference to the corresponding central Mo atom [167]. Figure 5-1(d) shows the micro-Raman spectra taken from the $MoSe_2$ layer with different thicknesses. The peak positions of the A_{1g} mode at 240.6 cm^{-1} for 1ML $MoSe_2$, 241.7 cm^{-1} for 2ML and 242.3 cm^{-1} for multilayer $MoSe_2$ are in good agreement with previous reports [167], confirming the thickness of $MoSe_2$ in our study. Besides the A_{1g} phonon mode, the $MoSe_2$ flake has other Raman active phonon modes like E_{2g}^1 and B_{2g}^1 visible at about 286.9 cm^{-1} and 355.7 cm^{-1}, as well as E_{1g} at 169.7 cm^{-1} for 1ML $MoSe_2$ (see Figure 5-1(c)). Their peak positions shift to lower wavenumbers as the number of layers increases and the highest peak intensities are observed for the $MoSe_2$ bilayer. The other peaks labeled in Figure 5-1(c) with a, b and c showing much broader features especially pronounced in monolayer and bilayer $MoSe_2$ are assigned to second-order Raman processes [168]. Interestingly, the A_{1g} phonon mode from 1ML $MoSe_2$ in vdWH has the same peak position as that from individual 1ML $MoSe_2$, but the peak intensity is significantly reduced, probably due to the softening of the phonons by phonon-carrier interaction.

The Raman spectrum from $FePS_3$ is also presented in Figure 5-1(c). $FePS_3$ shows six distinguishable peaks labeled with P_1-P_6. The observed phonon modes are in agreement with previously reported ones [76]. The P_3-P_6 phonon modes are assigned to the $(P_2S_6)^{4-}$ bipyramid

63

structures and P_1-P_2 are related to the Fe atoms and are sensitive to the magnetic coupling between Fe atoms [169].
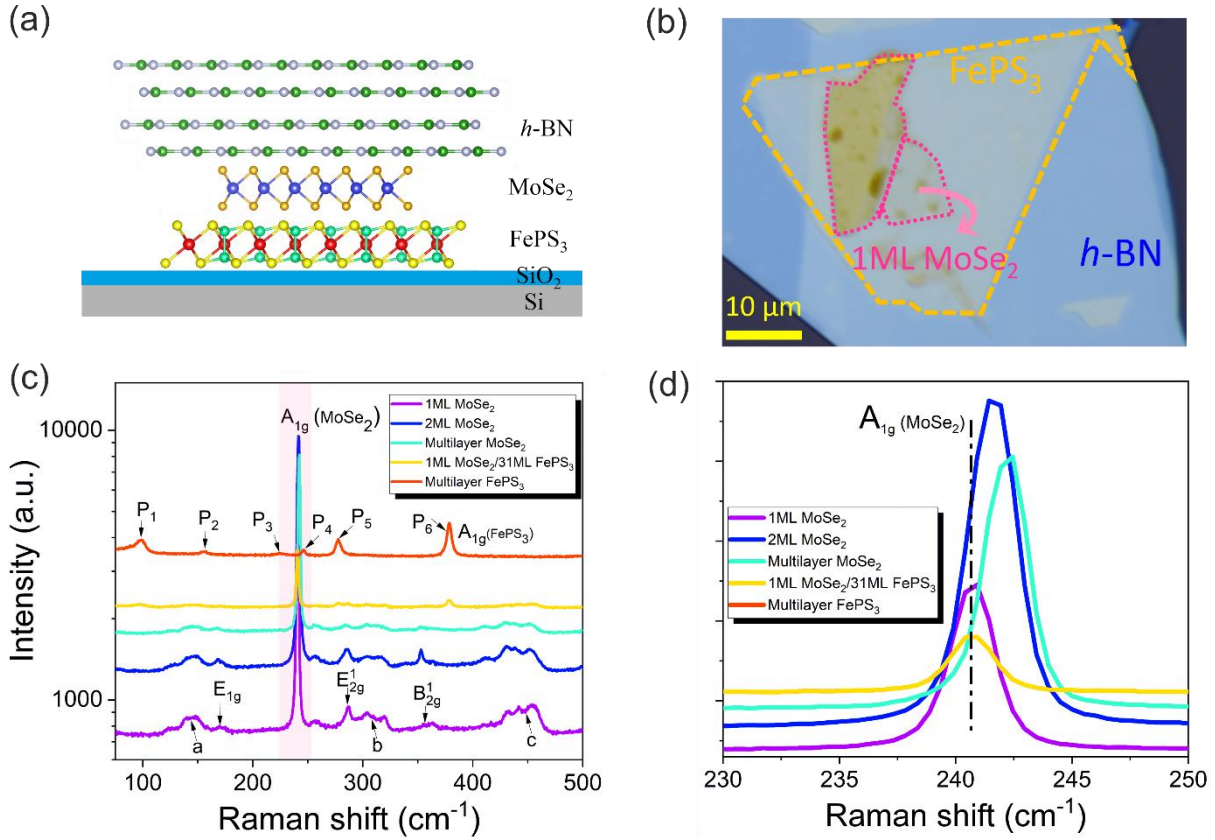
Fig. 5-1. (a) Schematic diagram of a fully *h*-BN covered MoSe$_2$/FePS$_3$ vdWH on a SiO$_2$/Si substrate. **(b)** Optical image of the 1ML MoSe$_2$ placed on the 31ML FePS$_3$ in vdWH. **(c)** Raman spectra from the 1ML MoSe$_2$, 2ML MoSe$_2$, multilayer MoSe$_2$, 1ML MoSe$_2$/31ML FePS$_3$ vdWH and multilayer FePS$_3$. **(d)** Zoomed-in Raman spectra for the marked region in panel (c) in the range of 230-250 cm^{-1} under a 532 nm laser excitation. All spectra were shifted vertically for clarity.

Figure 5-2(a, b) show the temperature-dependent Raman spectra from multilayer MoSe$_2$/FePS$_3$ heterostructure and multilayer FePS$_3$. A_{1g} and B_{2g}^1 peaks of MoSe$_2$ shift to lower wavenumber with increasing temperature as shown in Figure 5-2(a). The peaks labeled with P_1-P_6 originate from FePS$_3$ in the heterojunction. Note that at low temperature the P_1 phonon mode shows several separated sharp peaks including P_{1a}-P_{1d}, which become broad and asymmetric with increasing temperature. Especially as temperature increases from 110 to 120 K, P_{1a} and P_{1b} merge to one broad peak P_1. This phenomenon is due to the transition of the magnetic state from antiferromagnetic (AF) to paramagnetic (PM) in FePS$_3$ with a Néel temperature at 118 K [169]. Figure 5-2(b) illustrates the Raman spectra of multilayer FePS$_3$. It shows a similar behavior for P_1 mode like FePS$_3$ in MoSe$_2$/FePS$_3$ with increasing temperature

to 120 K, which suggests the Néel temperature remains at around 118 K for single multilayer FePS$_3$ or after combined with MoSe$_2$.
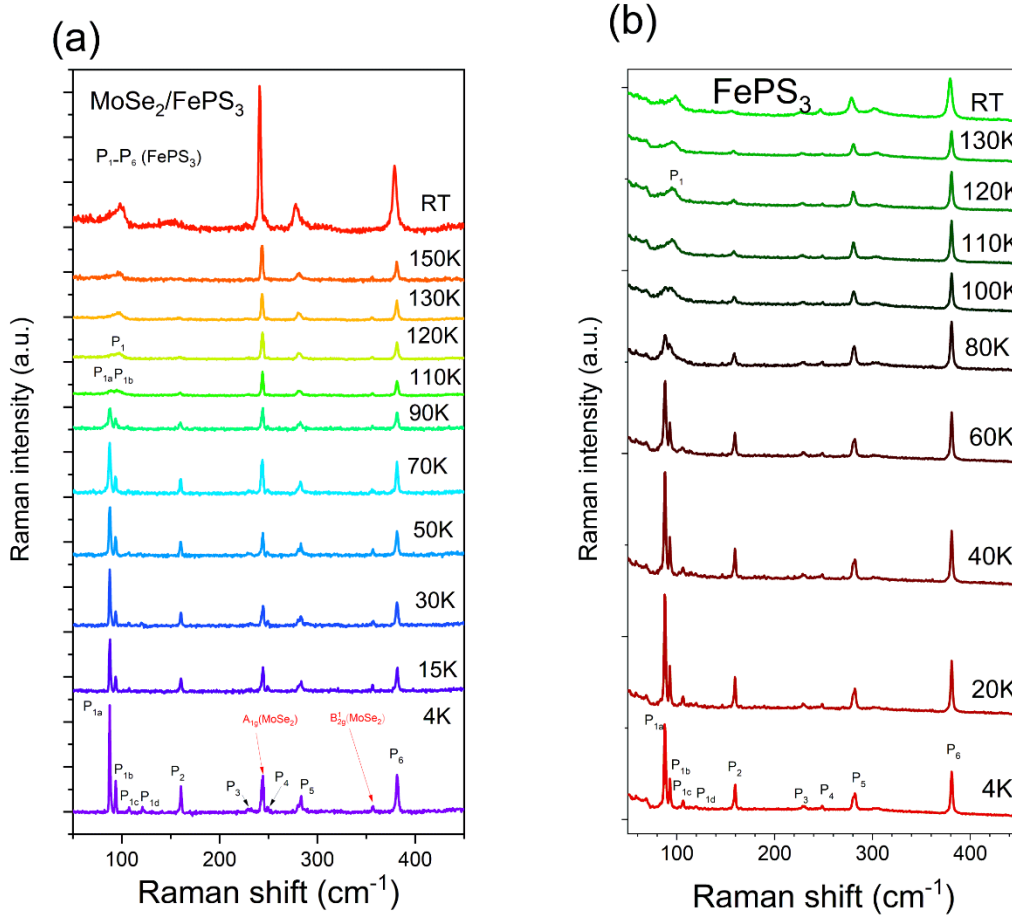
Figure 5-2. (a) Temperature dependent Raman spectra of a multilayer MoSe$_2$/FePS$_3$ heterostructure and **(b)** Raman spectra obtained from an individual FePS$_3$ flake.

5.3.2. Band alignment from DFT calculations

We used DFT calculations to investigate the band alignment for monolayer MoSe$_2$/FePS$_3$. For the calculations, we have considered a monolayer heterojunction 1ML MoSe$_2$/1ML FePS$_3$ and a heterojunction prepared of 3ML MoSe$_2$ on monolayer FePS$_3$, as shown in Figure 5-3(a). After structural optimization, an average interlayer distance of $d = 3.63$ Å was found between FePS$_3$ and MoSe$_2$. The binding energy between FePS$_3$ and MoSe$_2$ was calculated to be 16 meV/ Å^2 which is close to the values in other 2D vdWH interfaces [170]. Our electronic structure calculations indicate that the MoSe$_2$ monolayer has a direct band gap of 1.33 eV at the K point (Fig. 5-4(a)). The FePS$_3$ monolayer shows a quasi-direct bandgap of 2.27 eV where VBM and CBM are both located at the Σ point (midpoint of Γ and K points), as shown in Fig. 5-4(b).

Although DFT band gap cannot directly be compared to the optical gap measured in the experiment, our results are in line with the experimental band gaps (2.2 eV) [171] and the theoretical band gap (2.5 eV) for $FePS_3$ monolayer [82]. The slight difference of band gap values for $FePS_3$ monolayer between our calculation and the previous theoretical report [82] is due to different calculation methods. Based on the electronic structure calculations, the CBM of the $MoSe_2$ is lower than that of the $FePS_3$ while the VBM is higher than that of the $FePS_3$, forming type-I band alignment, as schematically illustrated in Figure 5-3(b, c). Both heterostructures with $1ML-MoSe_2$ and $3ML-MoSe_2$ show direct band gaps of 1.51 eV and 1.07 eV, situated at the Γ point in Figure 5-3 (b, c). The projected densities of states suggest that the VBM mainly consists of Mo d and Se p orbitals, whereas the CBM is mainly composed of the Mo d orbitals and slight contributions from Fe d states. To further analyze the effect of coupling between $FePS_3$ and $MoSe_2$, the average potential profile across the heterostructure and the charge difference between the combined system and isolated parts are shown in Figure 5-5. Owing to the higher potential energy of $MoSe_2$, the charge is redistributed in the system with predominant accumulation at the side of $MoSe_2$ layer facing $FePS_3$.
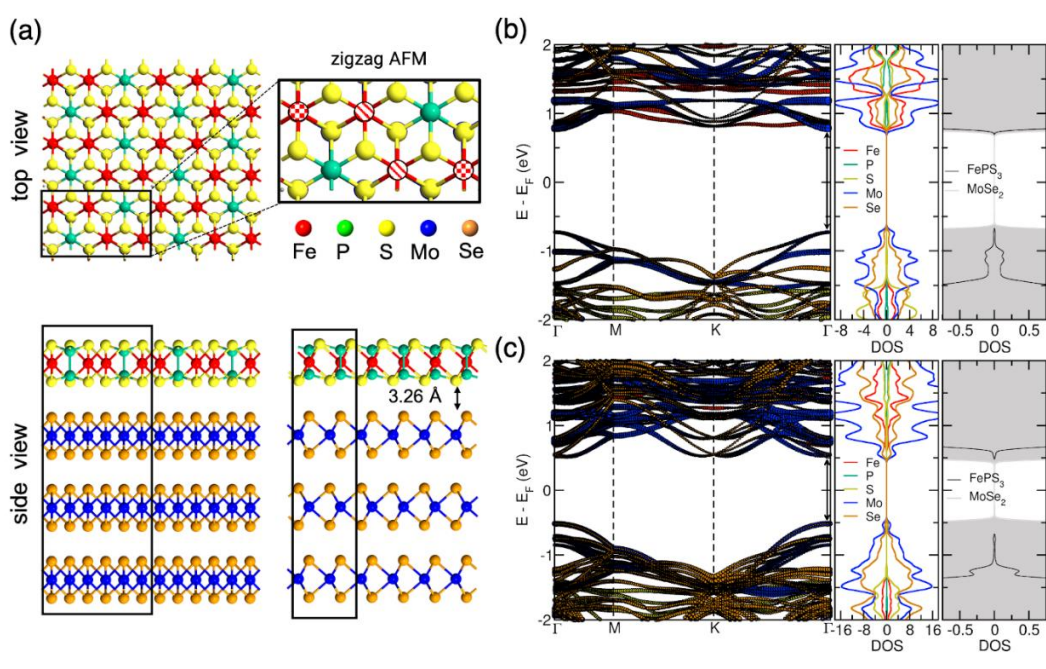
Figure 5-3. (a) Atomic structure of $FePS_3/MoSe_2$, the top and side views. The rectangular unit cell of $FePS_3$ is indicated by black lines. The hatched red markers illustrate the directions of local spins (up and down, checkerboard and striped circles) of zigzag antiferromagnetic order in the unit cell. **(b)** Calculated electronic band structure and density of states (DOS) of $1ML\ MoSe_2/1ML\ FePS_3$ and **(c)** $3ML\ MoSe_2/1ML\ FePS_3$ by DFT.
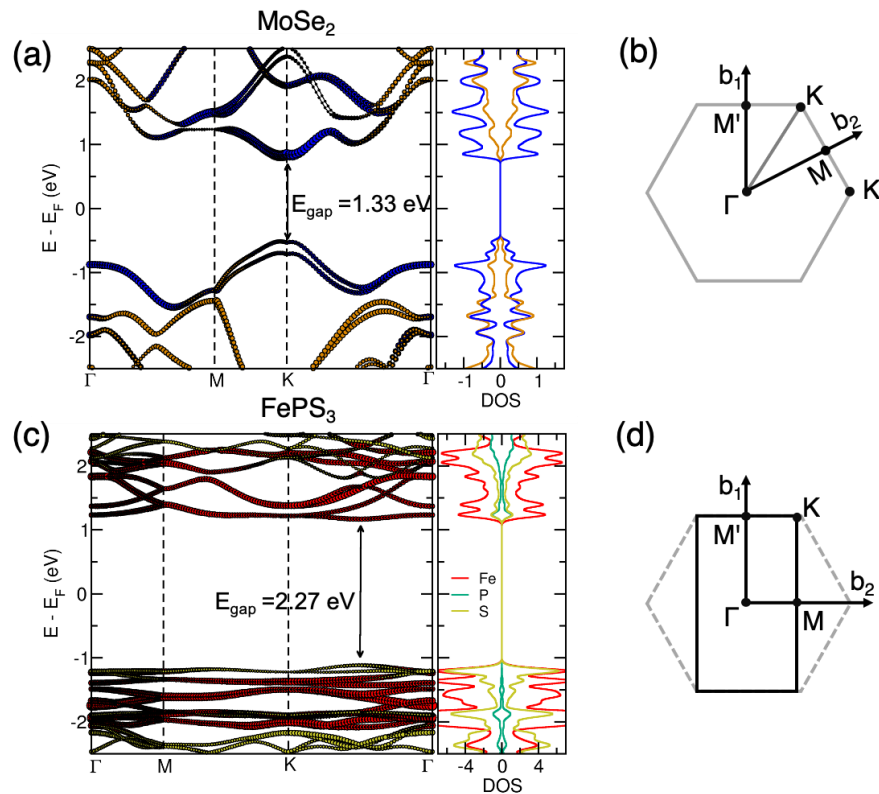
Figure 5-4. (a) Electronic band structure and density of states (DOS) of MoSe$_2$ monolayer calculated at the DFT/PBE level. The spin-orbit coupling (SOC) is considered. **(b)** First Brillouin zone and high-symmetry k-points of the hexagonal unit cell **(c)** Electronic band structure and DOS of FePS$_3$ monolayer calculated using the DFT+U method. **(d)** First Brillouin zone and high-symmetry k-points of the rectangular unit cell.
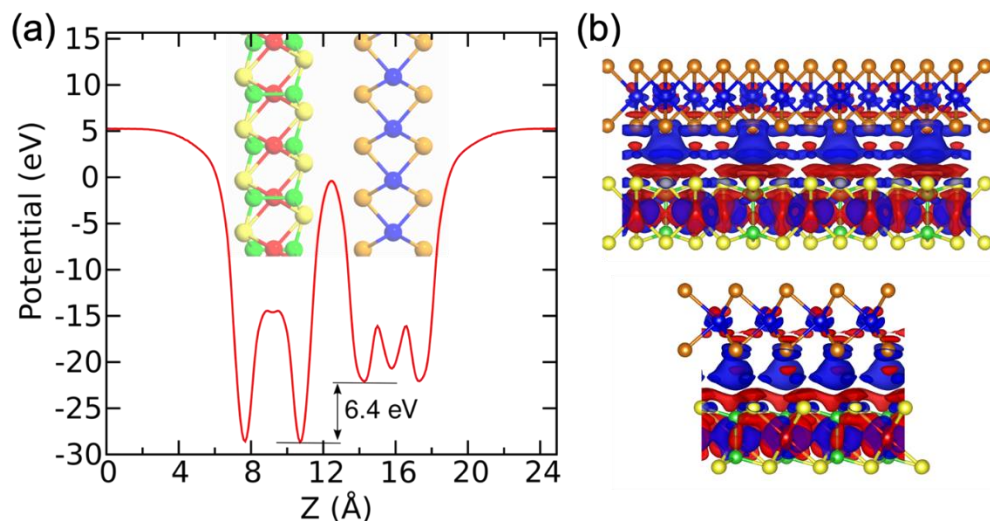
Figure 5-5. (a) Averaged electronic potential along the perpendicular direction of the FePS$_3$/MoSe$_2$ heterostructure. **(b)** Difference of the electron densities in the heterostructure and isolated sheets as viewed from two directions. Blue areas correspond to an increase in electron density, red to the depletion of the electronic charge.

5.3.3. Photoluminescence results

Figure 5-6 (a) shows the room temperature PL (RTPL) spectra of 1ML $MoSe_2$/31ML $FePS_3$, and individual $MoSe_2$ monolayer. The RTPL spectra obtained from 2ML individual $MoSe_2$ and its heterostructure are presented in Figure 5-6(b). Note that the RTPL measurement was performed in air under ambient conditions. Insets show optical images of investigated samples. 1ML and 2ML $MoSe_2$ are specially chosen here since $MoSe_2$ possesses thickness-dependent bandgap features [3, 69], i.e., a direct bandgap for monolayer $MoSe_2$ and an indirect bandgap for thicker $MoSe_2$. Similar to Raman spectra, the PL measurements can be used to determine the thickness of investigated $MoSe_2$ flakes. All the samples for PL measurement were covered with h-BN in order to prevent oxygen/moisture contaminations and obtain a high quality of optical emission spectra [172]. Since $FePS_3$ is an indirect band gap semiconductor [82] and its photogenerated carriers can quickly relax to $MoSe_2$ due to their type-I band alignment, all the PL peaks presented here originate only from $MoSe_2$ flakes. The single $MoSe_2$ monolayer flake shows the RT excitonic PL emission at 1.573 eV while the PL emission from 1ML $MoSe_2$/$FePS_3$ is slightly blue-shifted to 1.579 eV. More importantly, the heterostructure shows 20-fold enhancement of PL emission. Since the exciton lifetime in indirect semiconductors is generally much longer than in direct ones, the photogenerated carriers in $FePS_3$ can quickly diffuse into $MoSe_2$ and radiatively recombine there, which accounts for this giant PL enhancement in 1ML $MoSe_2$/31ML $FePS_3$. The PL emission from bilayer $MoSe_2$ on $FePS_3$ observed at 1.543 eV is enhanced by a factor of 1.3 in comparison to the individual flake. Zhang et al. have shown strong enhancement of the exciton emission from WS_2 monolayer covered with WO_3 due to reduction of non-radiative recombination channel and charge transfer within the heterostructure [173].As concluded from DFT calculation, 1ML $MoSe_2$/$FePS_3$ shows a straddling type-I band alignment between $MoSe_2$ (NBG) and $FePS_3$ (WBG).

In addition, the conductivity type of single $MoSe_2$ and $FePS_3$ flakes is confirmed by electrical measurements presented in Figure 5-7. Figure 5-7(a) shows that the I_{ds} increases with increasing positive gate voltage suggesting *n*-type conductivity of $MoSe_2$. Figure 5-7(b) presents the transfer characteristics of multilayer $MoSe_2$ and the on-off ratio of $MoSe_2$ is estimated to be $\sim 10^2$ from the curve. Moreover, we calculated the field-effect mobility of $MoSe_2$ using the equation $\mu_{FE} = \left(\frac{L}{WC_{ox}V_{ds}}\right)(d\,I_{ds}/d\,V_g)$, where C_{ox} =3.84×10^{-8} F/cm^2 is the capacitance per unit area of 90 nm SiO_2 between $MoSe_2$ and the back gate, L and W are the

channel length of 23 μm and channel width of 20 μm. The calculated field-effect mobility of MoSe$_2$ is determined to be $\mu_{FE} = 3.1 \times 10^{-2}$ cm^2 V^{-1} S^{-1} at V$_{ds} = 0.2$ V. It is worth mentioning that μ_{FE} of MoSe$_2$ is dependent on applied V$_{ds}$ and higher V$_{ds}$ can lead to a higher μ_{FE}. Figure 5-7(c) demonstrates the output characteristics of a multilayer FePS$_3$ transistor at different gate voltages. I$_{ds}$ of FePS$_3$ increases with increasing negative gate voltage suggesting p-type conductivity of FePS$_3$. MoSe$_2$ and FePS$_3$ possess n-type and p-type conductivity, respectively, which is consistent with other reports [79, 174].

After forming a heterojunction with type-I band alignment, holes will flow from FePS$_3$ to MoSe$_2$ to achieve an equilibrium state (see the middle panel in Figure 5-6(c)). In our case the thickness of the MoSe$_2$ is limited to one monolayer (about 0.7 nm), which can be completely converted to p-type when combining with 31 ML FePS$_3$. The shallowed areas in Figure 5-6(c) indicate the band alignment for 1ML MoSe$_2$/multilayer FePS$_3$. Under excitation, both electrons and holes generated in FePS$_3$ can diffuse to MoSe$_2$ with a result of its PL enhancement due to type-I band alignment (see the right panel in Figure 5-6(c)).

The smaller enhancement in 2ML MoSe$_2$/24ML FePS$_3$ is due to the fact that 2ML MoSe$_2$ is an indirect bandgap semiconductor with much lower radiative recombination rate [69]. Since the MoSe$_2$ layer is placed fully on the FePS$_3$ flake, we can exclude the possibility that surface charges in the SiO$_2$ substrate can donate carriers into MoSe$_2$, as it was previously reported [172, 175]. Therefore, in our case only FePS$_3$ can be the extra source of photogenerated carriers in MoSe$_2$. A PL emission enhancement for the narrower bandgap material in type-I van der Waals heterojunctions has been reported before, e.g. for MoTe$_2$-WSe$_2$ [95], PbI$_2$-WS$_2$ [176], WSe$_2$-black phosphorus [177], MoS$_2$-ReS$_2$ [159], GaSe-GaTe [96], etc. This distinct feature is substantially different from that of the widespread type-II band alignment for TMDCs heterostructures, like MoS$_2$-WSe$_2$ [155], MoS$_2$-MoSe$_2$ [152], MoS$_2$-WS$_2$ and WSe$_2$-MoS$_2$ [153, 178], where the PL emissions of two constituent layers are both quenched along with the appearance of an additional interlayer exciton peak with low energy [88, 179].
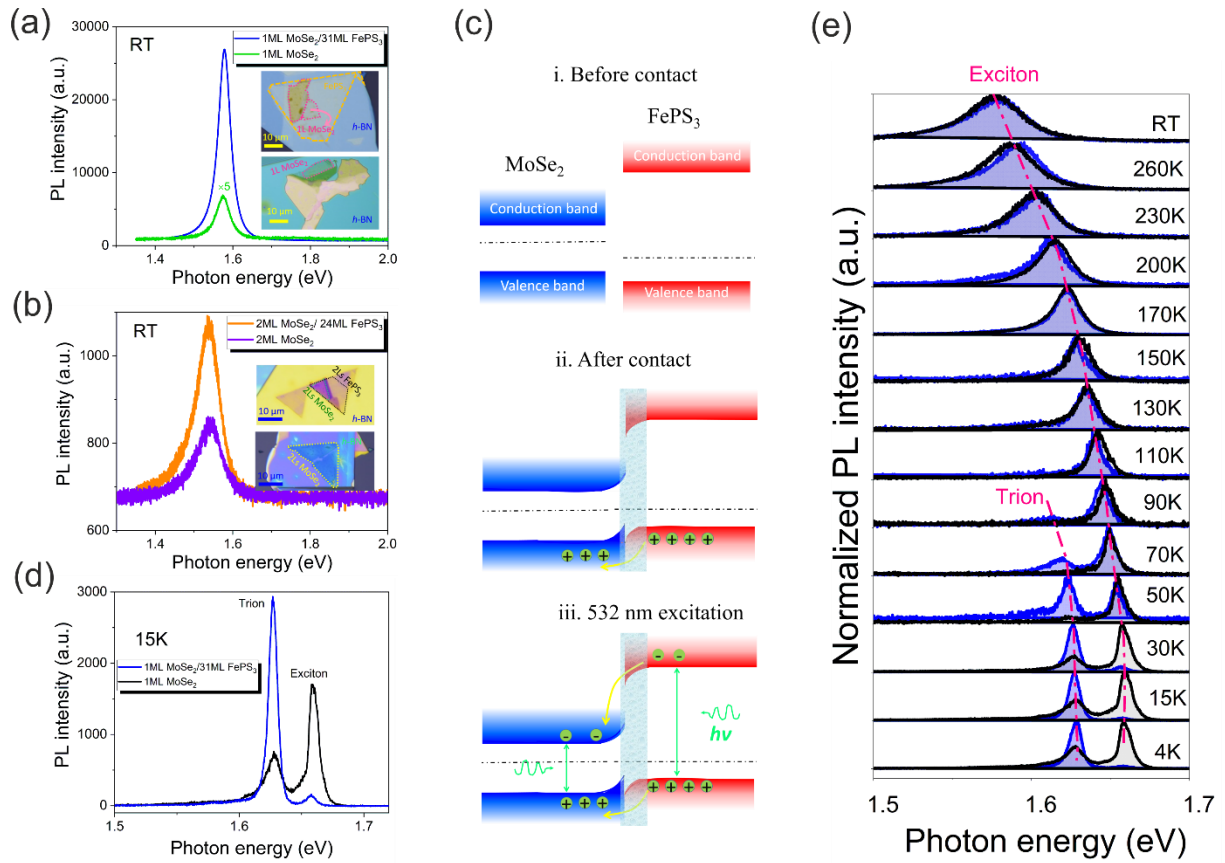
Figure 5-6. (a) RTPL spectra of 1ML MoSe₂/31ML FePS₃ and 1ML MoSe₂-single layer. **(b)** RTPL spectra of 2ML MoSe₂/24ML FePS₃ and 2ML MoSe₂-single layer. Insets are optical images of samples. **(c)** Band alignment of MoSe₂/ FePS₃: before contact of constituent layers, after contact of constituent layers and under laser excitation. The shadowed areas visualize the band alignment for 1ML MoSe₂/ multilayer FePS₃. **(d)** PL spectra of 1ML MoSe₂/31ML FePS₃ and single 1ML MoSe₂ at 15 K. **(e)** Normalized TDPL spectra for 1ML MoSe₂/31ML FePS₃ (blue-shaded areas) and 1ML MoSe₂ (black-shaded areas).
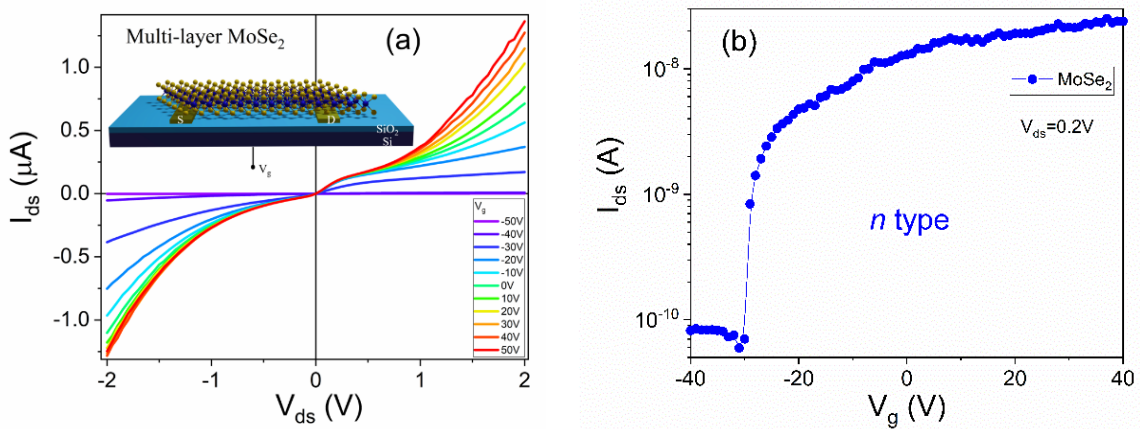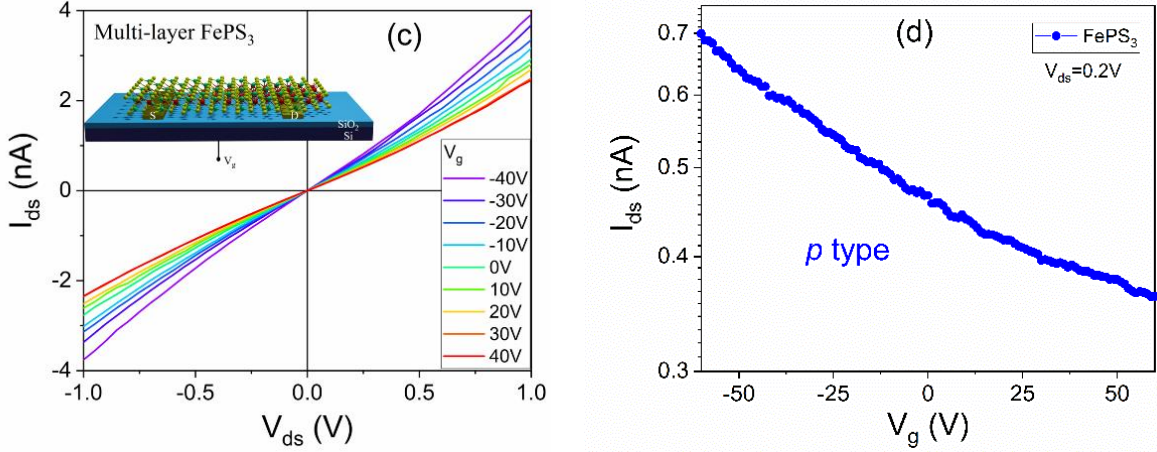
Figure 5-7. (a) Output characteristics of a multilayer MoSe₂ transistor at different gate voltages. **(b)** Transfer characteristics of a multilayer MoSe₂ transistor measured with V_{ds} = 0.2 V. **(c)** Output characteristics of a multilayer FePS₃ transistor at different gate voltages. **(d)** Transfer characteristics of a multilayer FePS₃ transistor measured with V_{ds} = 0.2 V. The insets in Figure S4 (a) and Figure S4 (c) represents the schematic of MoSe₂ and FePS₃ transistors.

To shine more light on the interaction and charge transfer between FePS₃ and MoSe₂, temperature-dependent PL (TDPL) measurements were performed. In this measurement, we focus on the sample 1ML MoSe₂/31ML FePS₃. As the reference sample, an individual MoSe₂ monolayer was also investigated. Figure 5-6(d) shows the PL spectra of 1ML MoSe₂/31ML FePS₃ and individual MoSe₂ monolayer at 15 K. The peaks at 1.66 and 1.63 eV in both spectra correspond to neutral exciton (X) and charged trion (T) emission from the MoSe₂ monolayer, respectively. The appearance of the trion emission in the individual MoSe₂ monolayer is due to the unintentional *n*-type doping as a consequence of impurities attached to reactive chalcogenide vacancies or defects in the SiO₂ substrate [180-182]. In Figure 5-6(d), we observe a giant enhancement of the trion emission and a dramatic suppression of the exciton emission (the PL intensity ratio $\frac{I_{Trion}}{I_X} = \sim 20$) for MoSe₂ in the heterojunction in comparison with $\frac{I_{Trion}}{I_X} = \sim 0.44$ for individual 1ML MoSe₂. The strong enhancement of the trion emission implies a strong doping of MoSe₂ in vdWH. Again, this agrees well with the definition of type-I band alignment where carriers can flow only in one direction from WBG to NBG. In heavily doped semiconductors excitons can trap free electrons or holes to form trions. This phenomenon also can be explained by a model based on the law of mass action [183, 184]:

$$\frac{N_X n_e}{N_T} = \left(\frac{4m_X m_e}{\pi \hbar^2 m_T}\right) k_B T \, exp\left(-\frac{E_B}{k_B T}\right) \qquad (5-1)$$

Here N_T, N_X and n_e are trion, exciton and charge carrier concentrations, $\hbar$ is the reduced Planck's constant, k_B is the Boltzmann constant, T is the temperature, E_B is the trion binding energy, m_e is effective mass of electrons, m_X and m_T are exciton and trion effective masses, respectively. According to this model, there is a positive correlation between $\frac{N_T}{N_X}$ and n_e, i.e. $\frac{N_T}{N_X}$ increases with increasing carrier concentration n_e. Since the concentrations of trions and excitons are proportional to their PL intensities ($\frac{N_T}{N_X} \propto \frac{I_T}{I_X}$), it means that doping (higher n_e or n_p) can lead to a higher PL intensity ratio $\frac{I_T}{I_X}$. Besides, the increased trion binding energy, which can be modified by the dielectric environment, could also lead to a higher $\frac{I_T}{I_X}$. Specifically, a lower dielectric constant of the environment can reduce the total screening effect on 1ML TMDCs, which can result in a higher trion binding energy and further can contribute to a higher $\frac{I_T}{I_X}$ [172]. Due to $\varepsilon_{FePS_3} < \varepsilon_{SiO_2}$, it means that FePS$_3$ in vdWHs may provide an environment that is more energetically favorable for trion formation in MoSe$_2$/FePS$_3$ than in individual MoSe$_2$ being directly contacted with a SiO$_2$ substrate.

Figure 5-6(e) shows the normalized TDPL spectra for vdWHs (dash-dotted lines) and individual 1ML MoSe$_2$ (solid lines). The red shift of exciton and trion peaks for both samples is observed with increasing temperature, which is due to temperature-induced bandgap shrinkage. Below 50 K, the trion emission gives a pronounced peak and dominates the spectra of vdWH, while in individual 1ML MoSe$_2$ the exciton emission dominates the PL spectra because of the lower carrier concentration and thus lower trion concentration. At 50 K the trion and exciton emissions from the heterojunction have comparable intensity, but with increasing temperature the trion emission vanishes. This is due to thermal fluctuations resulting in the conversion from trions to excitons. In individual 1ML MoSe$_2$ the trion emission is already negligible as compared with the exciton peak at 50 K as a consequence of lower carrier concentration. In the temperature range of 90-300 K, only the exciton emission peak is observed for both vdWHs and individual MoSe$_2$. Note that we assume FePS$_3$ has no effect on the exciton peak position of MoSe$_2$ in vdWHs. In addition, the thermal stability of the trion also depends on its charge state. Positively charged trions, X$^+$, have localized holes that are less prone to scattering, leading to the reduced line width [162].

In order to clarify the charge sign of trions in both systems and to explore their potential impacts on valleytronics, we have employed PL excitation with circularly polarized light (see Figure 5-8). Using left-(σ^-) or right-handed (σ^+) excitation in both systems, we have seen differences in the PL emission. Here, the degree of circular polarization is evaluated as $P_c =$

$[I(\sigma +) - I(\sigma -)]/[I(\sigma +) + I(\sigma -)]$, where $I(\sigma +)$ and $I(\sigma -)$ correspond to the PL intensities under left-(σ^-) or right-handed (σ^+) excitation. In the individual monolayer MoSe$_2$ the exciton emission is enhanced by 13% for σ^+ excitation while the trion emission is almost not affected with a small broadening. The exciton emission polarization is resulted from the broken inversion symmetry and the strong SOC in monolayer TMDCs [185], which gives rise to two inequivalent K+ and K- valleys with different population. Due to the spin-valley locking effect, the right-handed (σ^+) circular polarized photon initializes a carrier in the K+ valley and the left-handed (σ^-) initializes a carrier in the K- valley, i.e. valley dependent optical selection rules [186, 187]. Zeng et.al. reported that 30% valley polarization can be achieved in pristine monolayer MoS$_2$ with circularly polarized light pump [187]. For PbI$_2$/WS$_2$ heterostructure with type I band alignment, Zhang and coworkers have shown near unity spin polarization in PbI$_2$ due to the modification of the carrier lifetime [188]. In the heterostructure MoSe$_2$/FePS$_3$, the exciton emission is the same for both excitations, while the trion emission exhibits a polarization of about 14%. It suggests that no carrier spin polarization is introduced from Ising-type antiferromagnetic FePS$_3$ to MoSe$_2$. Moreover the trion emission from the heterostructure is narrower than from the individual MoSe$_2$ monolayer and the peak position is blue shifted for the heterostructure by about 2 meV. Since holes are more localized than electrons in MoSe$_2$, X^+ are immobile and less prone to scattering, leading to a narrow linewidth of X^+ than X^- [162]. A similar energy difference for the X^+ and X^- emission and narrowing of the PL emission for X^+ in MoSe$_2$ were observed by Shepard et al [162]. Therefore, we can conclude that in our case negatively charged trions X^- form at low temperature in the individual MoSe$_2$ monolayer, while in the heterostructures the trions are positively charged due to hole injection from p-type FePS$_3$ into the MoSe$_2$ monolayer.
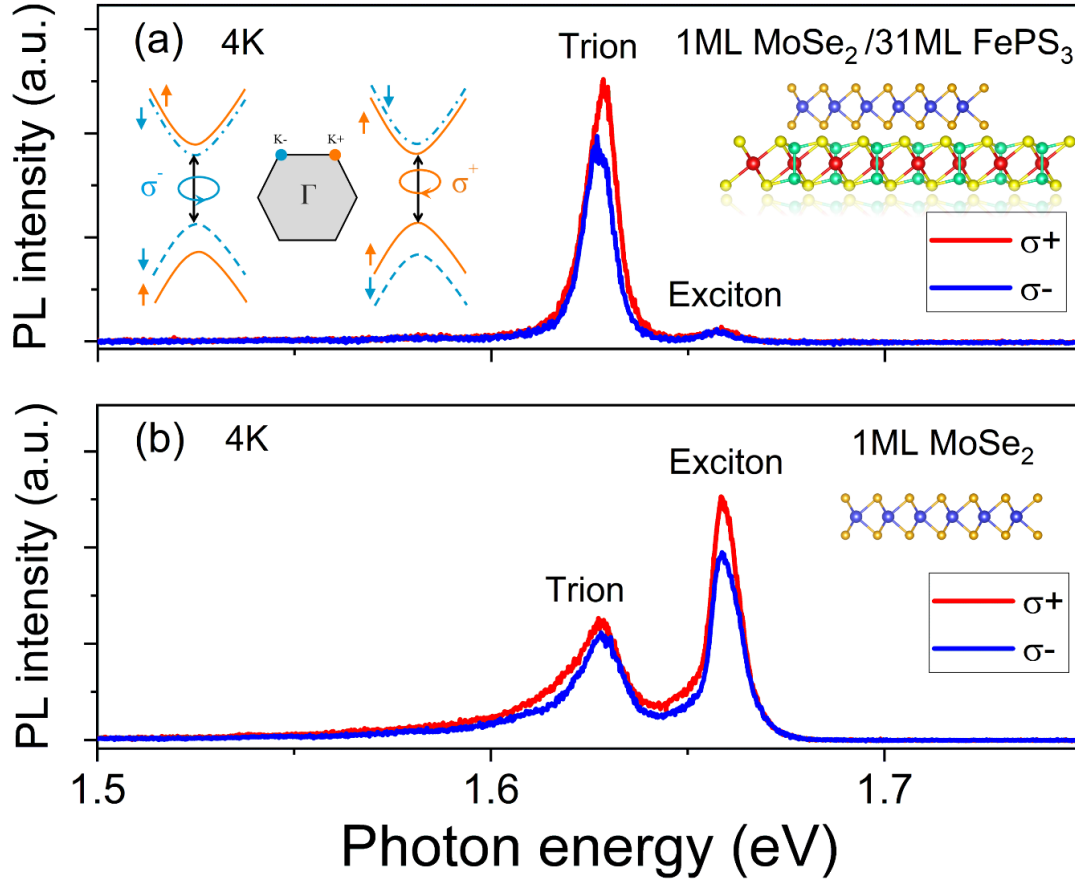
Figure 5-8. Low temperature PL emission after excitation with left- or right-handed circularly polarized light obtained from the heterojunction **(a)** and from the individual $MoSe_2$ monolayer **(b)**. The inset shows the chiral optical selection rules for interband optical transitions in nonequivalent valleys K+ and K- in monolayer $MoSe_2$.

5.4 Conclusion

In conclusion, we have performed a systematic study of optical properties for a novel semiconductor-antiferromagnetic $MoSe_2/FePS_3$ vdWH. DFT calculations show the type-I band alignment in ultrathin $MoSe_2/FePS_3$, which is verified by the PL results. The room temperature PL shows 20-fold enhancement of the emission from 1ML $MoSe_2$ in $MoSe_2/FePS_3$ vdWH, which is due to carrier injection from WBG $FePS_3$ to NBG $MoSe_2$. At low temperatures, the intensity ratio between trion and exciton emission increases from 0.44 to about 20. Moreover, the heterojunction exhibits trion emission polarization, which makes it attractive for valleytronics. Our results present a novel approach to modify the population of trions and excitons as well as the trion charge state by forming a heterostructure with type-I band alignment. This approach is transferable to many other 2D materials and is opening a broad playground for fundamental physics and for valleytronic applications.

Chapter 6. Self-driven Broadband photodetector based on MoSe$_2$/FePS$_3$ van der Waals n-p Type II heterojunctions

2D van der Waals materials with broad-band optical absorption are promising candidates for next-generation UV-vis-NIR photodetectors. FePS$_3$, one of the emerging antiferromagnetic van der Waals materials with a wide bandgap and p-type conductivity, has been reported as an excellent candidate for UV optoelectronics. However, a high sensitivity photodetector with a self-driven mode based on FePS$_3$ has not yet been realized. Here, we report a high-performance and self-powered photodetector based on multilayer MoSe$_2$/FePS$_3$ type-II n-p heterojunction with a working range from 350 to 900 nm. The presented photodetector, operating at zero bias and at room temperature under ambient conditions, exhibits the maximum responsivity (R_{max}) of 52 mA W^{-1} and external quantum efficiency (EQE$_{max}$) of 12% at 522 nm, which are better than the characteristics of its individual constituents and many other photodetectors made of 2D heterostructures. The high performance of MoSe$_2$/FePS$_3$ is attributed to the built-in electric field in the MoSe$_2$/FePS$_3$ n-p junction. Our approach provides a promising platform for broadband self-driven photodetector applications.

6.1 Introduction

Two-dimensional (2D) materials are usually characterized by strong in-plane covalent bonds and weak out-of-plane van der Waals interlayer bonding. The weak interlayer van der Waals interaction allows easy and flexible stacking of different 2D materials to form the so-called van der Waals heterostructures (vdWHs). vdWHs offer the great advantage to combine different features into single devices and introduce novel physical properties [5-7, 88, 179]. Graphene is the first discovered 2D material [189]. Unfortunately, due to the lack of a bandgap, the application of graphene in optoelectronic devices is limited. Later, a new family of 2D materials, i.e., transition metal dichalcogenides (TMDCs), has been introduced. Usually, TMDCs with the structural formula MX_2, where M= Mo, W, etc., and X=S, Se, Te, have optical bandgaps in the range of 0.8-2.1 eV. Moreover, TMDCs possess interesting and diverse physical properties, like the existence of neutral and charged excitons, spin-valley coupling [1], and indirect-to-direct bandgap transitions when the thickness is reduced down to one monolayer [2-4]. With these unique features, vdWHs consisting of TMDCs open a complete new application avenue for optoelectronic devices, like solar cells [8], light emitting diodes [9], and photodetectors [10]. However, the relatively small optical bandgap of TMDCs imposes some limitation on the harvesting of the ultra-violet (UV) photons. Even though Zhou *et al.* reported that the working range of the MoS_2-based photodetector can be extended from the visible to the UV range by combining MoS_2 flakes with ZnO quantum dots [160], the performance of such photodetectors is significantly limited due to the poor interface quality.

Recently, a new class of 2D materials consisting of transition metal chalcogenophosphates (TMCPs) has been discovered with the general formula MPX_3, where M=Fe, Ni, Mn and X=S, Se. TMCPs exhibit antiferromagnetic properties making them attractive for spintronics [190-192]. In addition to this, they possess a relatively large bandgap (from 1.3 to 3.5 eV) [193, 194]. This makes them excellent candidates for UV photodetectors [79-81]. Ramos *et al.* have shown that the $FePS_3$ few-layer thick photodetector presents an external quantum efficiency (EQE) of about 7% with ultra-broad spectral photoresponse [195]. The EQE can be further enhanced by applying the heterojunction approach. TMCPs can easily be integrated with TMDCs due to the similar atomic structure, aiming for a high-performance broadband optoelectronic device. At the same time, although interlayer exciton-magnon coupling in $MnPSe_3/MoSe_2$ heterostructure has been studied, [196], a vdWH photodetector combining MX_2 and MPX_3 has not yet been reported. Indeed, such a MX_2/MPX_3 vdWH not only can overcome the band gap limitations of

individual van der Waals crystals, but also form a n-p junction, since TMCPs and TMDCs are p-type and n-type materials, respectively.

In this work, we fabricated a broadband, high-performance and self-powered photodetector based on $MoSe_2/FePS_3$ vdWH. The multilayer $FePS_3$ and $MoSe_2$ have a band gap of around 2.0 eV and 1.3 eV, respectively. The photocurrent measurements clearly indicate the formation of a heterojunction with type-II band alignment between n-type $MoSe_2$ and p-type $FePS_3$. It is shown that the photogenerated electrons and holes at the heterojunction are spatially separated between $MoSe_2$ and $FePS_3$ due to the built-in electric field at the n-p junction. Analyzing the figures of merit including the response time, responsivity, external quantum efficiency, specific detectivity and noise equivalent power, we show that the self-powered $MoSe_2/FePS_3$ photodetector with the working range of 350-900 nm exhibits a significant improvement of the performance due to the type-II band alignment. The measured maximum responsivity and EQE are as high as 52 mA W^{-1} and 12 %, respectively. Note that the EQE is about 170 % higher than the best $FePS_3$ based photodetector ever presented. The performance of $MoSe_2/FePS_3$ is also superior to its individual TMDCs constituent and many other vdWH photodetectors.

6.2 Experimental details

Sample preparation:

The $MoSe_2/FePS_3$ photodetectors were fabricated by sequential mechanically exfoliation of $MoSe_2$ and $FePS_3$ flakes using blue tape Nitto SSWT+R. Flakes are transferred on the SiO_2/Si substrates (90 nm thick SiO_2 on heavily doped Si) with the help of a polymer stamp transfer technique within a nitrogen atmosphere in a glove box environment. This technique provides samples with good quality, intact atomic interfaces and low contamination. For electrical measurements and photodetector testing, pre-patterned electrodes with Ti/Au (5/45 nm) on SiO_2/Si substrates were fabricated by standard photolithography and electron beam evaporation processes.

Characterization:

The structural properties of the heterostructure were investigated using micro-Raman spectroscopy. The phonon spectra were measured using a cw frequency-doubled Nd:YAG laser at a wavelength of $\lambda=532$ nm with the maximum laser power limited to 3.2 mW. The spot diameter of the laser on the sample was approximately 3 μm, i.e., much smaller than the heterojunction area. A liquid nitrogen-cooled Si-CCD camera was used to record the phonon

spectra. For the optoelectrical measurements, a Hg-Lamp with a working range of 350 - 2500 nm was aligned with a monochromator for dispersion. The measurements were performed in the wavelength range of 350 - 900 nm. The monochromatic light was coupled into the quartz fiber and focused on samples using an optical microscope. The electrical signal was recorded by a 2410 Keithley device. The light power density at the working wavelength range was calibrated by a power meter with a Si detector. Time-dependent measurements were controlled by a mechanical shutter with the time resolution down to 1 ms. Layer thicknesses were measured by atomic force microscopy using a Bruker Multimode 8 system.

Calculation Details:

Calculations are done by M. Ghorbani-Asl and A. V. Krasheninnikov.

Electronic structure calculations were carried out using density functional theory (DFT) and the projector augmented wave method as implemented in the VASP code [164]. Perdew-Burke-Ernzerhof (PBE) exchange-correlation functional was used for all the simulations [165]. To account for the high correlation effects among d-orbital electrons of iron atoms, an effective Hubbard value (U) of 5.5 eV was considered for Fe atoms within the DFT + U approach. The cut-off energy for the plane-wave basis was set at 600 eV. The Brillouin zone of the system was sampled using $8 \times 8 \times 4$ k-mesh for bulk supercells and $8 \times 8 \times 1$ k-mesh for slab supercells. In order to describe weak van der Waals interactions, the DFT-D2 method with pair approximation has been adopted [166]. The geometry optimization was carried out until the atomic forces were less than 0.01 eV/Å. A vacuum layer of 20 Å perpendicular to the basal plane was introduced to implement the isolated slab condition.

6.3 Results and discussion

6.3.1 Raman results

Figure 6-1 shows the room temperature micro-Raman spectra from multi-layer $MoSe_2$, $FePS_3$ flakes and the $MoSe_2/FePS_3$ heterostructure, respectively. The $MoSe_2$ flakes show the characteristic peak at about 242 cm^{-1} corresponding to the A_{1g} phonon mode. It is an out-of-plane vibration mode, where the Se atoms oscillate in-phase with Mo atoms [167]. Besides the strongest out-of-plane A_{1g} phonon mode, several others vibration modes can be observed in ultra-thin layer $MoSe_2$, i.e., E_{2g}^1 and B_{2g}^1 located at about 287 cm^{-1} and 356 cm^{-1}, respectively, as well as E_{1g} mode at 170 cm^{-1}. These modes become less pronounced as the thickness of $MoSe_2$ increases. The $FePS_3$ flake shows well distinguishable six phonon modes labeled with

P_1-P_6. The phonon modes P_1 and P_2 are related to the Fe atoms, while the phonon modes labeled with P_3-P_6 are assigned to the $(P_2S_6)^{4-}$ bipyramid structures in $FePS_3$ [76, 169]. P_1 and P_2 modes are sensitive to the magnetic coupling between Fe atoms and can be used to determine the Néel temperature in $FePS_3$ [76]. In Figure 6-1, the Raman spectrum of $MoSe_2$/$FePS_3$ shows the A_{1g} mode from $MoSe_2$ along with pronounced P_1, P_5 and A_{1g} (P_6) from $FePS_3$, indicating a successful formation of heterostructure.
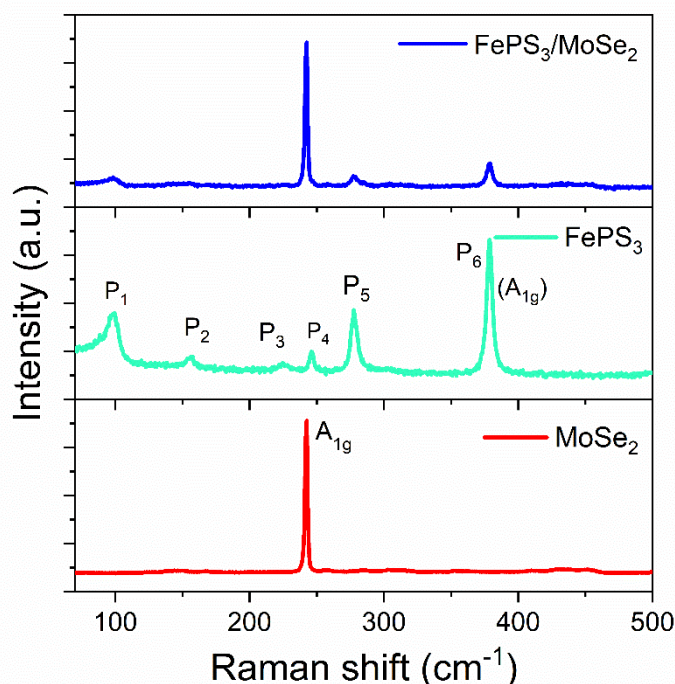
Figure 6-1. Micro-Raman spectra of individual $MoSe_2$ and $FePS_3$ flakes and $MoSe_2$/$FePS_3$ heterostructure.

6.3.2 Photodetector based on $MoSe_2$/$FePS_3$

In this section, we discuss the photodetector performance of the $MoSe_2$/$FePS_3$ vdWH. The schematic of the investigated photodetector is shown in Figure 6-2(a). To prepare the photodetectors, a $MoSe_2$ flake was first transferred onto one of a pair of pre-patterned gold electrodes, then a $FePS_3$ flake was partially placed onto the $MoSe_2$ flake to form a heterojunction and partially on the other electrode to provide an electrical connection. Figure 6-2(b) presents an optical image of a representative device, where the vdWH heterojunction area is marked with the green dotted line. The thicknesses of the $MoSe_2$ and $FePS_3$ flakes are about 48 and 180 nm, respectively, which are measured by atomic force microscopy as shown in Figure 6-2(c).
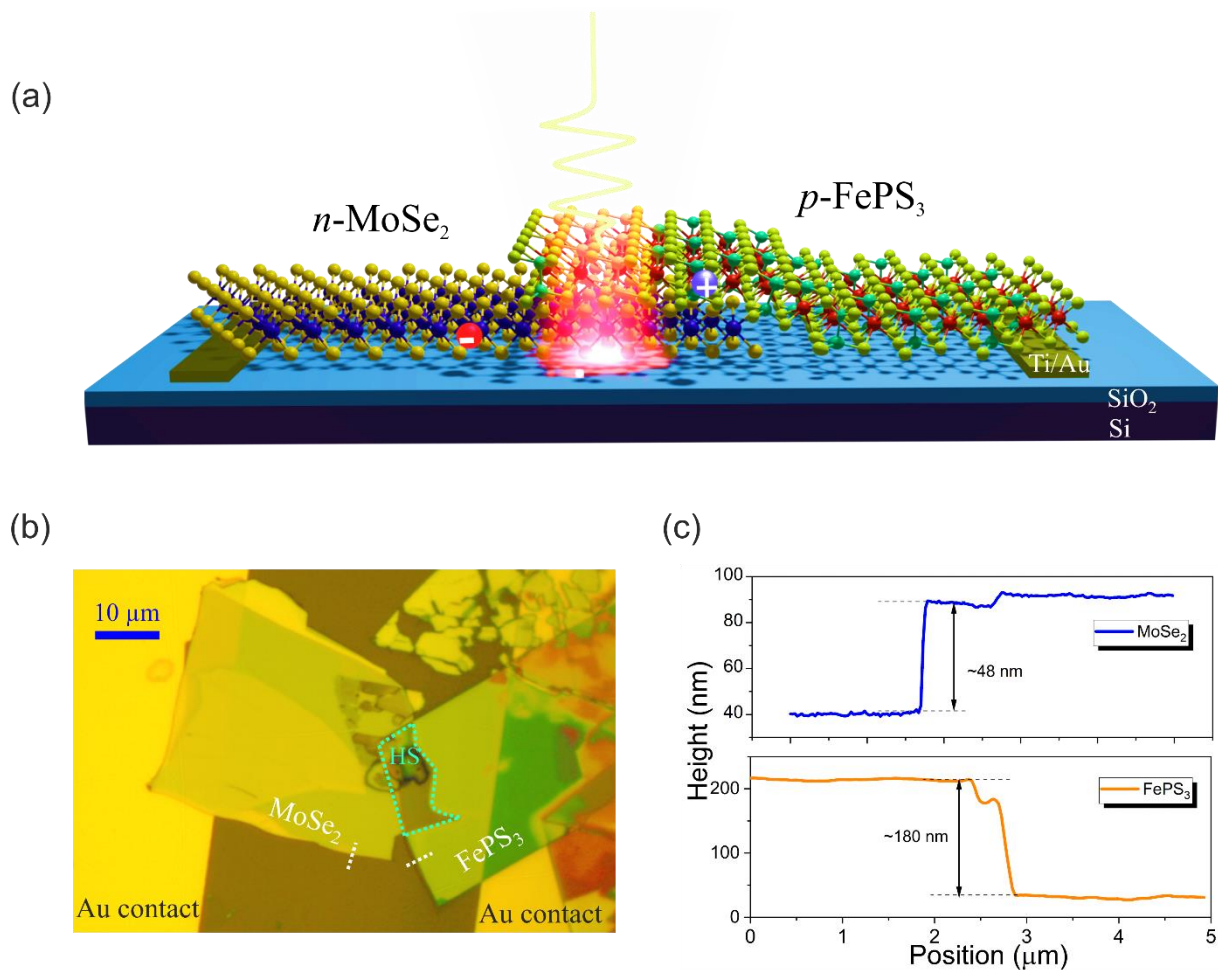
Figure 6-2. (a) Schematic diagram of the MoSe$_2$/FePS$_3$ photodetector. **(b)** Optical image of the MoSe$_2$/FePS$_3$ heterostructure. The scale bar corresponds to 10 μm. **(c)** The height profile along the dashed white lines in the optical image of the sample showing a thickness of 48/180 nm for MoSe$_2$/FePS$_3$.

The typical current-voltage (I-V) analysis of MoSe$_2$/FePS$_3$ under dark and illumination conditions is shown in Figure 6-3. During the measurement, the applied voltage was swept from -2 to 2 V with the positive potential applied to the p-type FePS$_3$ flake. All measurements were performed under ambient conditions. An asymmetrical current flow is clearly observed when the polarity of the bias voltage is altered under dark conditions. The ratio of the forward to reverse current at 1 V is about 18. In order to clarify the origin of the rectifying behavior of the studied MoSe$_2$/FePS$_3$ heterostructure, we investigated the electrical properties of the individual MoSe$_2$ and FePS$_3$ flakes (see Figure 5-7). The MoSe$_2$ flakes possess nearly ohmic-like contact and n-type conductivity. The FePS$_3$ flakes are p-type semiconductors with an ideal ohmic contact between the flake and the Au contact. This indicates that the formation of a n-p junction is responsible for the rectifying behavior of I-V curves presented in Figure 6-3.

80

In order to quantitatively characterize the MoSe$_2$/FePS$_3$ n-p junction, we use the single-diode equation to fit the dark I-V curve. The fitting curve is represented by a dash-dot orange line (see Figure 6-3). The fitting equation is given as follows:

$$I = I_s \left[e^{\frac{q(V-IR_s)}{\eta k_B T}} - 1 \right] + \frac{V - IR_s}{R_{sh}} \qquad (6\text{-}1)$$

where I_s is the saturation current, q is the electron charge, η is the ideality factor, k$_B$ is the Boltzmann constant and T is the temperature; whereas R_s and R_{sh} are the series and parallel resistances, respectively. The ideality factor of 2.7 obtained from the fitting indicates that the generation/recombination process dominates at the interface of the heterojunction [197]. The reason for $\eta > 2$, which is reported to be a common feature for many wide bandgap heterojunction diodes [198, 199], could be related to the non-linear I-V characteristic of MoSe$_2$ that induces a nonhomogeneous recombination current in the heterojunction. Moreover, I_s, R_s and R_{sh} are found to be 4.0 pA, 3.7×10^8 Ω, and 7.6×10^9 Ω, respectively.

In addition, the significant enhancement of photocurrent under monochromatic lights at the wavelengths of 400, 500, 600, 700 and 878 nm is observed, which is attributed to the photogeneration of free carriers in the MoSe$_2$/FePS$_3$ heterojunction. The working spectral range is consistent with the absorption region of MoSe$_2$ and FePS$_3$ (blue area), as shown in Figure 6-4.
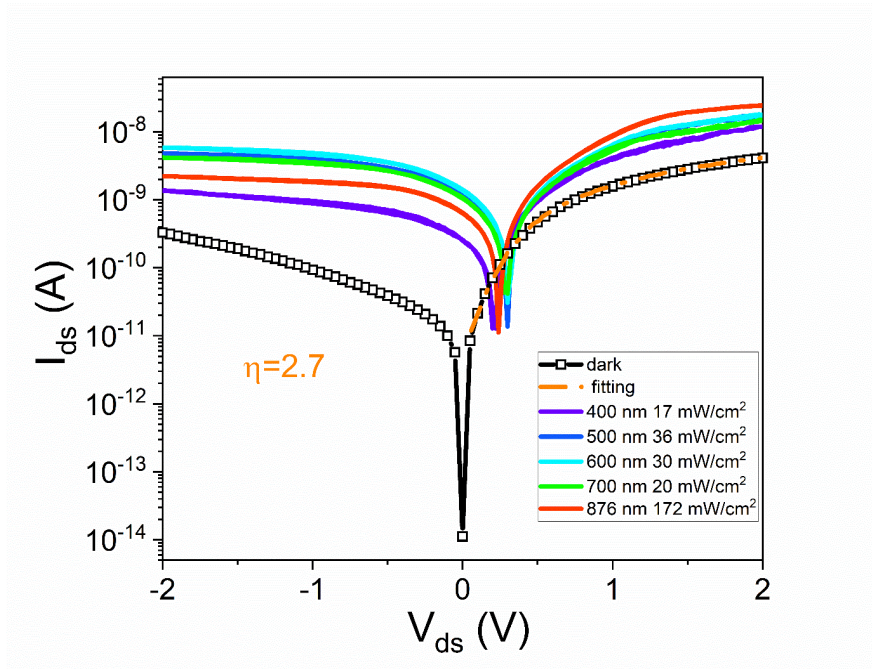
Figure 6-3. Current-voltage (I-V) curves of the MoSe$_2$/FePS$_3$ heterojunction under dark and illumination conditions. The fitting result of the dark I-V curve by using a single-diode equation is represented by the dash-dot orange line.
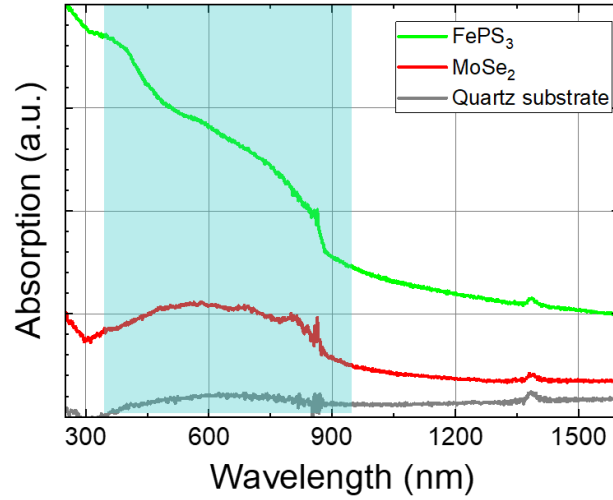
Figure 6-4. UV-vis-near infrared absorption spectra of $MoSe_2$, $FePS_3$ and the quartz substrate. The absorption spectra of exfoliated $MoSe_2$ and $FePS_3$ flakes with different thickness on quartz substrates are determined by UV-vis-near infrared spectroscopy measurement.

Figure 6-5(a) shows the time-resolved on-off switching behaviors of the $MoSe_2/FePS_3$ photodetector under the incident light 450, 600 and 757 nm without applying any external bias voltage. The results with applying a bias voltage of 1 V are shown in Figure 6-5(b). A sharp increase and fast stabilization of the current is observed when light is shone on the heterojunction. The rectangular wave shape of photocurrent ($I_{ph}=I_{light}$ -I_{dark}) can be well maintained after many on-off cycles, indicating good stability and reproducibility of our devices. The photocurrent on/off ratios at zero bias voltage are as high as 15, 29 and 20 under pulsed illumination at 450, 600 and 757 nm, respectively. Moreover, the rise and delay times are estimated to be 0.6 s by counting the response times from 10% to 90% of the stable generated photocurrent under illumination off/on states and vice versa. These superior features manifest the effective generation and separation of electron-hole pairs in the heterojunction area. In addition, we performed the photocurrent measurement by varying the incident illumination power. The incident power intensity decreases from 91% to 12% of the initial power as shown in Figure 6-5(a). It is noteworthy that the response rise and decay times, being independent of the incident power density, remain at 0.6 s along with a rectangular wave shape of photocurrent.

Figure 6-5(c) shows the photocurrent (I_{ph}) as a function of the input optical power with a log-log scale without and with the bias voltage of 1 V at 600 nm illumination. To determine the detector performance, the experimental results were fitted by the power law $I_{ph} \propto P^a$. The

deduced a values are 0.95 at zero bias and 0.92 at 1 V bias, implying the following facts: (i) a sub-linear dependence of the photogeneration of electron-hole pairs on the illumination power; (ii) the balance between the light absorption and the generation/collection of carriers over the measured range of incident light power, since there is no saturation of I_{ph} [200]; (iii) due to a equals to 1 for an ideal trap-free photodetector [201], $a = 0.95$ at 0 V bias in our devices suggests that there are trapping states at the MoSe$_2$/FePS$_3$ interface. Note that the smaller a at 1 V bias compared to at 0 V bias implies that more traps are filled with carriers.

Responsivity (R) and external quantum efficiency (EQE), which determine the efficiency of a detector responding to optical signals, are critical parameters for a photodetector. R can be calculated with the equation $R = \frac{I_{ph}}{P \times A}$, where P is the incident light intensity and A is the effective illumination area which is defined as the overlapped area of the heterojunction (100 μm^2 here). EQE is calculated using $EQE = R \times \frac{hc}{e\lambda} = \frac{R}{\lambda} \times 1240$, where λ is the incident light wavelength, h is the Planck constant, c is the speed of light in vacuum, and e is the elementary charge. Figure 6-5(d) presents the calculated R and EQE values with a monotonically decreasing trend with increasing incident power at zero bias. The maximum R and EQE at 600 nm are determined to be 40.2 mA W^{-1} and 8.3%. The reason for the decreasing trend is due to the limited concentration of photogenerated carriers at high excitation power. More specifically, as more photogenerated hole-electron pairs are produced with increasing incident power, a higher proportion of photogenerated hole-electron pairs tend to recombine at the trapping states before being collected by electrodes. The effective photogenerated carriers and the photocurrent do not increase accordingly, resulting in a decrease of R and EQE.

Figure 6-5(e) exhibits the evaluated R and EQE of the MoSe$_2$/FePS$_3$ photodetector in the range of 400-900 nm at zero bias. The maximum R_{max} and EQE$_{max}$ are respectively estimated to be 52 mA W^{-1} and 12 % at the wavelength of 522 nm (2.38 eV), under which both MoSe$_2$ and FePS$_3$ absorb lights (see Figure 6-4) and contribute photogenerated carriers. It is noteworthy that this R$_{max}$ is much higher than previously reported FePS$_3$-single (12 mAW^{-1}) [79] or MoSe$_2$-single (13 mAW^{-1}) [202] photodetectors with applying external voltage listed in **Table 6.1**. Additionally, the responsivity is also higher or comparable with other TMDCs based heterojunction photodetectors in the self-powered mode, like 5.5 mAW^{-1} for GaSe/MoSe$_2$ [203], 29 mAW^{-1} for MoS$_2$/WS$_2$ [10] and 89 mAW^{-1} for Graphene/MoS$_2$ [204]. This superior feature is attributed to the efficient light absorption and holes-electrons separation in the MoSe$_2$/FePS$_3$ heterojunction.

To further quantify the performance of the MoSe₂/FePS₃ photodetector, the key figure of merit, noise equivalent power (NEP) is introduced, indicating the minimum illumination power that delivers a unity signal-to-noise ratio at 1 Hz bandwidth. It can be evaluated according to:

$$NEP = \frac{\overline{I_n^2}^{1/2}}{R} \qquad (6\text{-}2)$$

where R is photoresponsivity and $\overline{I_n^2}^{1/2}$ is the root mean square of the total noise current [205]. Two fundamental sources of noise for the MoSe₂/FePS₃ photodetector are Johnson noise (I_{jn}) and shot noise (I_{sn}). Johnson noise is calculated as $I_{jn}{}^2 = \frac{4k_BT}{R_{sh}}\Delta f$, where k_B is the Boltzmann constant, T is the absolute temperature, Δf is the bandwidth and R_{sh} is the shunt resistance of the photodiode. Shot noise is determined as $I_{sn}{}^2 = 2qI_d\Delta f$, where I_d is the photodetector dark current. Then, the specific detectivity (D^*) can be deduced as:

$$D^* = \frac{(A_0\Delta f)^{1/2}}{NEP} = R(A\frac{4k_BT}{R_{sh}}\Delta f + 2AqI_d\Delta f)^{1/2} \qquad (6\text{-}3)$$

where A is the heterojunction area and R is the responsivity of a photodetector with the unit of AW⁻¹. The calculated NEP and D^* of photodetector at zero bias is presented in Figure 6-5(f). The maximum D^* is found to be 1.4×10^{10} cm Hz$^{1/2}$W⁻¹ at the wavelength of 522 nm, which is comparable to 2.2×10^{10} cm Hz$^{1/2}$W⁻¹ for Graphene/MoS₂ [204] and larger than many other TMDCs based photodetectors, for example, 2.1×10^9 cm Hz$^{1/2}$W⁻¹ for black phosphours/MoS₂ [206], 3.3×10^8 Hz$^{1/2}$W⁻¹ for CuO/MoS₂ [207], 1.1×10^{10} cm Hz$^{1/2}$W⁻¹ for MoS₂ [208]. An as low as possible NEP value is desirable for an efficient and sensitive photodetector. The ultralow NEP value of 6.2×10^{-14} WHz$^{-1/2}$ is obtained at 522 nm which is lower than many other van der Waals photodetectors, like 2.4×10^{-13} WHz$^{-1/2}$ for black arsenic phosphorus photodetector [209], $10^{-13}\sim10^{-14}$ WHz$^{-1/2}$ for p-GaSe/n-MoS₂ [210]. It is noteworthy that the stable NEP and D^* values in 500-800 nm, without dramatic change, are favorable factors for the practical application of MoSe₂/FePS₃ photodetectors.
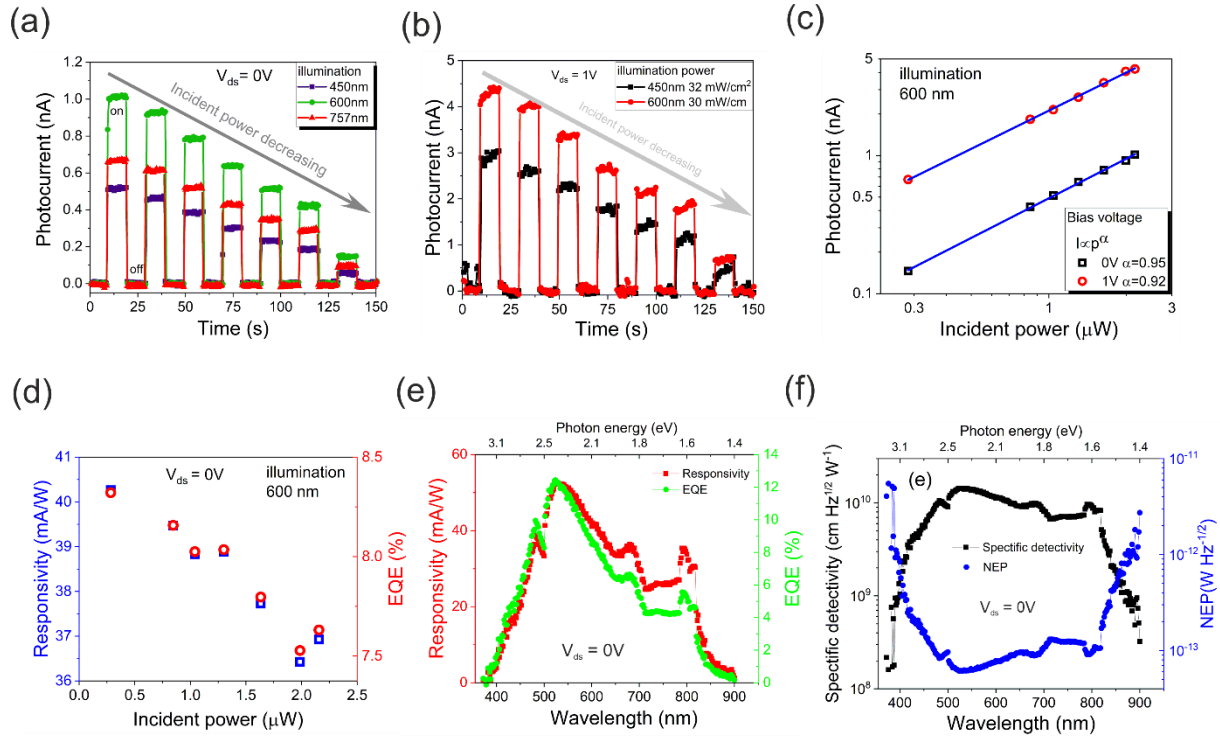
Figure 6-5. (a, b) Time-dependent photocurrent of the MoSe$_2$/FePS$_3$ photodetector at zero bias (i.e., photovoltaic mode) and with applying a bias voltage of 1 V. The initial incident power intensity of 450 nm @32 mW/cm^2, 600 nm @30 mW/cm^2 and 757 nm @33 mW/cm^2 decreased from 91% to 12%. **(c)** The power law fitting for the plot of photocurrent versus incident light power at an applied bias of 1 V and zero bias at 600 nm. **(d)** Incident power dependent responsivity and EQE of photodetector at zero bias at 600 nm. **(e)** Responsivity and EQE spectra measured at zero bias. **(f)** Specific detectivity (*D**) and noise equivalent power (NEP) spectra at zero bias.

Table 6.1 The performance comparison between our MoSe$_2$/FePS$_3$ heterojunction-based photodetector and other devices in literature.

Materials	Bias voltage (V)	λ (nm)	R (mA W^{-1})	D* (cm Hz$^{1/2}$ W^{-1})	Ref
MoSe$_2$/FePS$_3$	V$_g$=0 V, V$_d$=0 V	522	52	1.4×10^{10}	our work
FePS$_3$	V$_d$=0.06 V, V$_g$=0 V	254	12	NA	[79]
MoSe$_2$	V$_d$=10 V, V$_g$=0 V	532	13	NA	[202]
Gr/MoSe$_2$	V$_g$=0 V, V$_d$=0 V	600	89	2.2×10^{10}	[204]
MoS$_2$/WS$_2$	V$_g$=0 V, V$_d$=0 V	532	29	NA	[10]
GaSe/MoSe$_2$	V$_g$=0 V, V$_d$=0 V	white light	5.5	NA	[203]

6.3.3 Carrier transfer mechanism in MoSe$_2$/FePS$_3$

Figure 6-6 shows the measured photocurrent spectra of the MoSe$_2$/FePS$_3$ heterostructure at the photovoltaic mode and the individual MoSe$_2$ (red area) flake under a bias voltage of 1 V. The spectrum of MoSe$_2$ is normalized by overlapping with the spectrum of MoSe$_2$/FePS$_3$. In both measurements, the same illumination power was used. We have also tested an individual FePS$_3$ flake under a 1 V bias, but the photocurrent was very low (see Figure 6-7). Then by subtracting the MoSe$_2$ signal from that of the heterojunction, the spectrum of FePS$_3$ is obtained and shown as the green area in Figure 6-6. Based on the photocurrent spectra of MoSe$_2$/FePS$_3$ heterostructure, we can conclude: i) it is a type-II band alignment since the detector working spectra are limited by the photon absorption of narrow bandgap materials, MoSe$_2$ here. For type-I heterostructure photodetector, there is no photoresponse for the photon energy range which is smaller than the bandgap of wide bandgap materials [211]; ii) based on Tauc's law the optical bandgaps of multilayer thick MoSe$_2$ and FePS$_3$ are respectively estimated to be 1.3 and 2.0 eV [212, 213] as shown in Figure 6-8; (Details: Near the absorption edge, the absorption coefficient of a semiconductor is given by $a(\lambda) = A \frac{(hv - E_g^{opt})^n}{hv}$, where A is the material-dependent effective Richardson constant, E_g^{opt} is the optical bandgap, hv is the photon energy and $n = 2$ for indirect transitions. By assuming that near the absorption edge the photocurrent I_{ph} is proportional to the absorption coefficient a, we get $(I_{ph}hv)^{\frac{1}{2}} \propto (hv - E_g^{opt})$ [213]. From the $(I_{ph}hv)^{\frac{1}{2}} - hv$ plot, the band gap is extrapolated as the outlined in Figure 6-8 where the intercepts give 1.3 and 2.0 eV for multilayer MoSe$_2$ and FePS$_3$, respectively.) iii) high efficiency of charge transfer in the MoSe$_2$-FePS$_3$ interface. It is manifested by the observation of significant photocurrent generation of FePS$_3$ in the vdWH, as well as a self-driven mode for MoSe$_2$/FePS$_3$ as a photodetector, considering that none of these features is observed in individual MoSe$_2$ and FePS$_3$ photodetector devices (Figure 6-7 and 6-9);
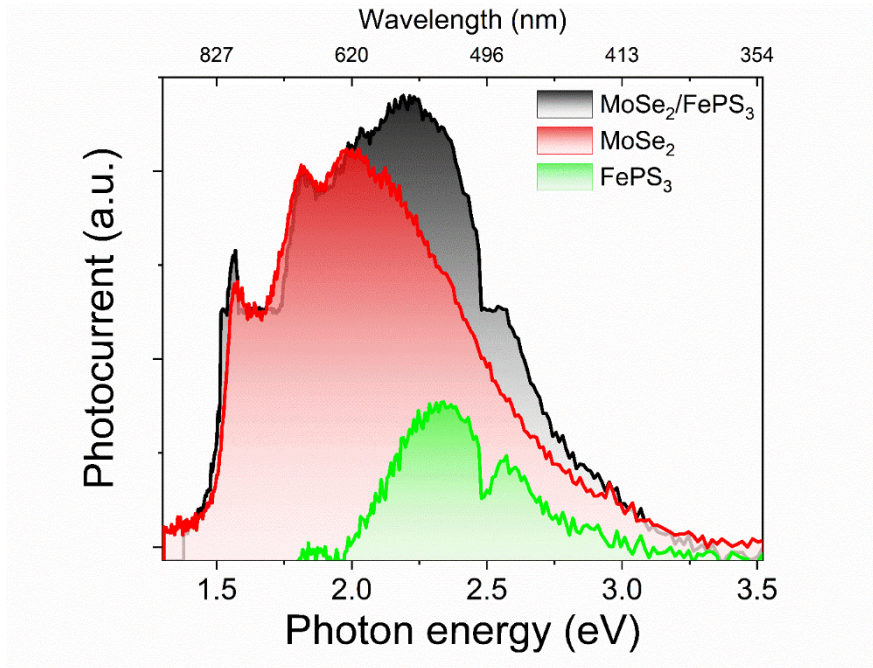
Figure 6-6. Photocurrent spectrum of $MoSe_2/FePS_3$ measured at the photovoltaic mode; Spectrum of individual $MoSe_2$ (red area) at 1 V bias is normalized by overlapping with the spectrum of $MoSe_2/FePS_3$ at the absorption starting point around 1.5 eV; Spectrum of individual $FePS_3$ is obtained by subtracting the $MoSe_2$ signal from that of the heterojunction.
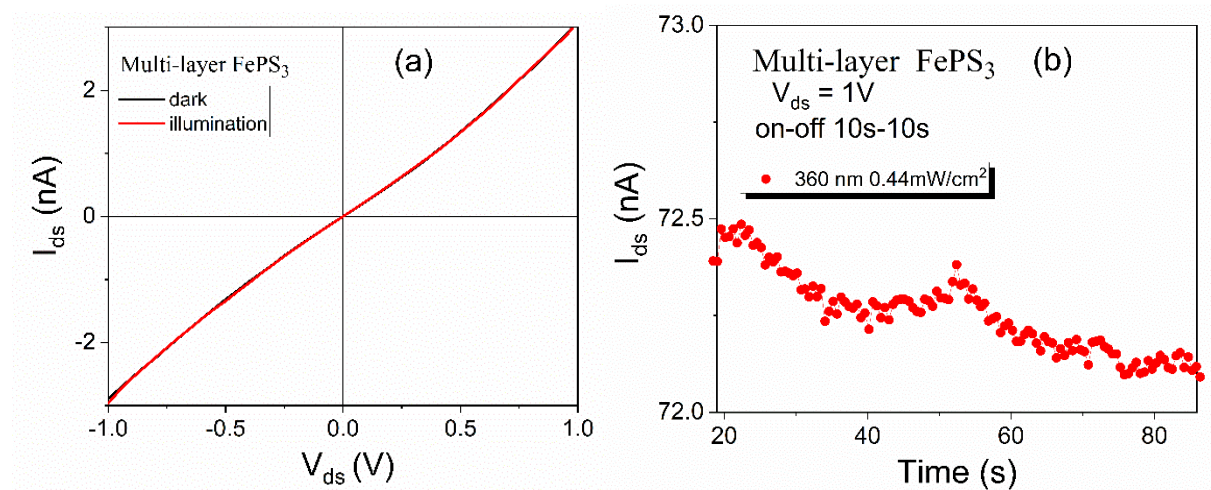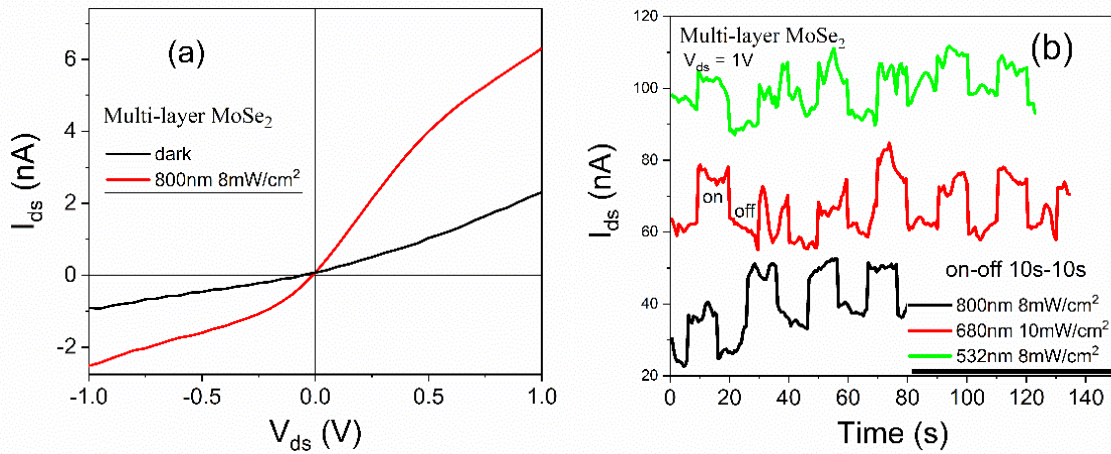

Figure 6-7. (a) Current-voltage (I-V) curves of multi-layer $FePS_3$ under dark and illumination conditions. **(b)** Time-resolved current-time measurement of multilayer $FePS_3$ with 360 nm illumination at V_{ds} =1 V. No significant photocurrent is generated.
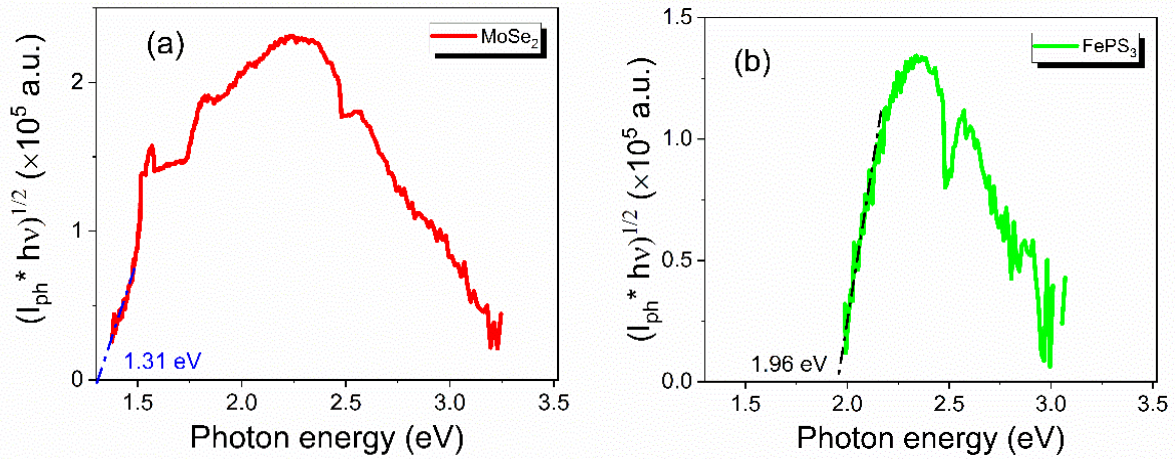
Figure 6-8. (a, b) Plot of $(I_{ph}hv)^{\frac{1}{2}}$ as a function of the photon energy for multi-layer MoSe$_2$ and FePS$_3$, the dashed lines are the Tauc extrapolations of the absorption edge, where the intercepts give 1.3 and 2.0 eV for multilayer MoSe$_2$ and FePS$_3$, respectively.

Figure 6-9. (a) Current-voltage (I-V) curves of multi-layer MoSe$_2$ under dark and illumination conditions. (b) Time-resolved current-time measurement of multilayer MoSe$_2$ with 532 nm, 680 nm and 800 nm illumination at V$_{ds}$ =1 V. The poor rectangular wave shape of current under illumination manifests the lower efficient of separation and transportion of photogenerated electrons and holes in single multilayer MoSe$_2$ with applied bias.

Figure 6-10(a) and (b) shows the calculated electronic band structure and density of states of bulk MoSe$_2$ and bulk FePS$_3$ at the DFT/PBE and LDA+U levels, respectively. Our calculations indicate indirect band gaps of 0.88 eV and 2.27 eV for MoSe$_2$ and FePS$_3$, respectively. The calculated bandgaps are smaller than our experimentally observed values, which is due to the fact that the generalized gradient approximation and local density approximation usually underestimate the bandgap. Figure 6-10(c) shows that the calculated VBM and CBM values for multilayer MoSe$_2$ and FePS$_3$. Note that the materials are considered to be intrinsic.
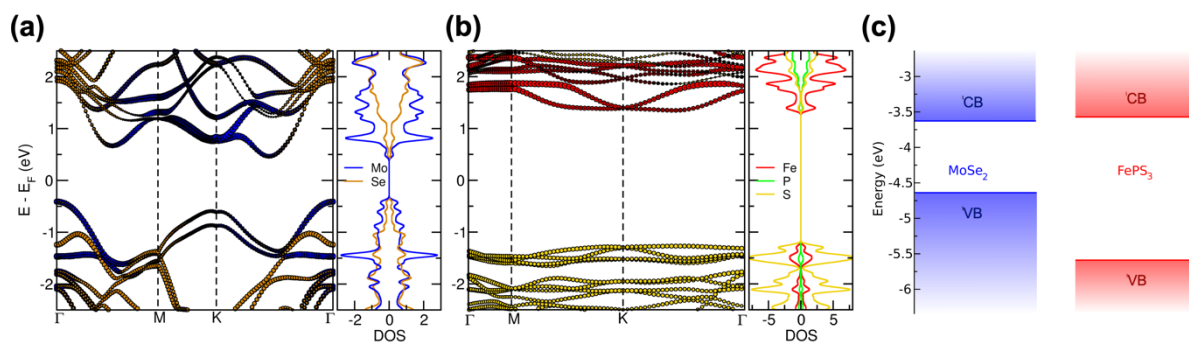
Figure 6-10. (a, b) Electronic band structure and density of states (DOS) of bulk $MoSe_2$ and bulk $FePS_3$ calculated at the PBE and LDA+U levels, respectively. **(c)** Calculated band-alignment for multilayer (4ML) $MoSe_2$/ (5ML) $FePS_3$.

In addition, ultraviolet photoelectron spectroscopy (UPS) measurements were performed on exfoliated $MoSe_2$ and $FePS_3$ flakes with different thicknesses to obtain the work function (Φ) and the valence band maximum (VBM) of multilayer $MoSe_2$ and $FePS_3$. Figure 6-11(a) and (b) present the experimental results, where the intercepts of the kinetic-energy-axis near the secondary electron cut-off edge and the Fermi edge correspond to the Φ and VBM, respectively. The Φ and the VBM of multilayer $MoSe_2$ are determined to be 3.5 and 20.3 eV, and the Φ and the VBM of multilayer $FePS_3$ are 4.1 and 20.6 eV. The bandgaps of multilayer $MoSe_2$ and $FePS_3$ are estimated to be 1.3 and 2.0 eV, respectively, based on the photoresponse measurements (see Figure 6-8).

The schematic of band alignment for the multilayer $MoSe_2/FePS_3$ heterostructure is depicted in Figure 6-11(c). The before-contact state of $MoSe_2/FePS_3$ is deduced from the UPS result. The single $MoSe_2$ and $FePS_3$ flakes possess *n*-type and *p*-type conductivity (see Figure 5-7), respectively, which is consistent with other reports [79, 174]. After contact, multilayer $MoSe_2/FePS_3$ possesses a type-II band alignment as shown in the right panel of Figure 6-11(c). Photogenerated holes in $MoSe_2$ drift to $FePS_3$ while photogenerated electrons drift from $FePS_3$ to $MoSe_2$ due to the built-in electric field. The formation of the n-p junction and its type-II band alignment explain the high performances and the self-driven nature in our $MoSe_2/FePS_3$ vdWHs photodetector. Note that the band alignment for monolayer $MoSe_2/FePS_3$ is a type-I [214].
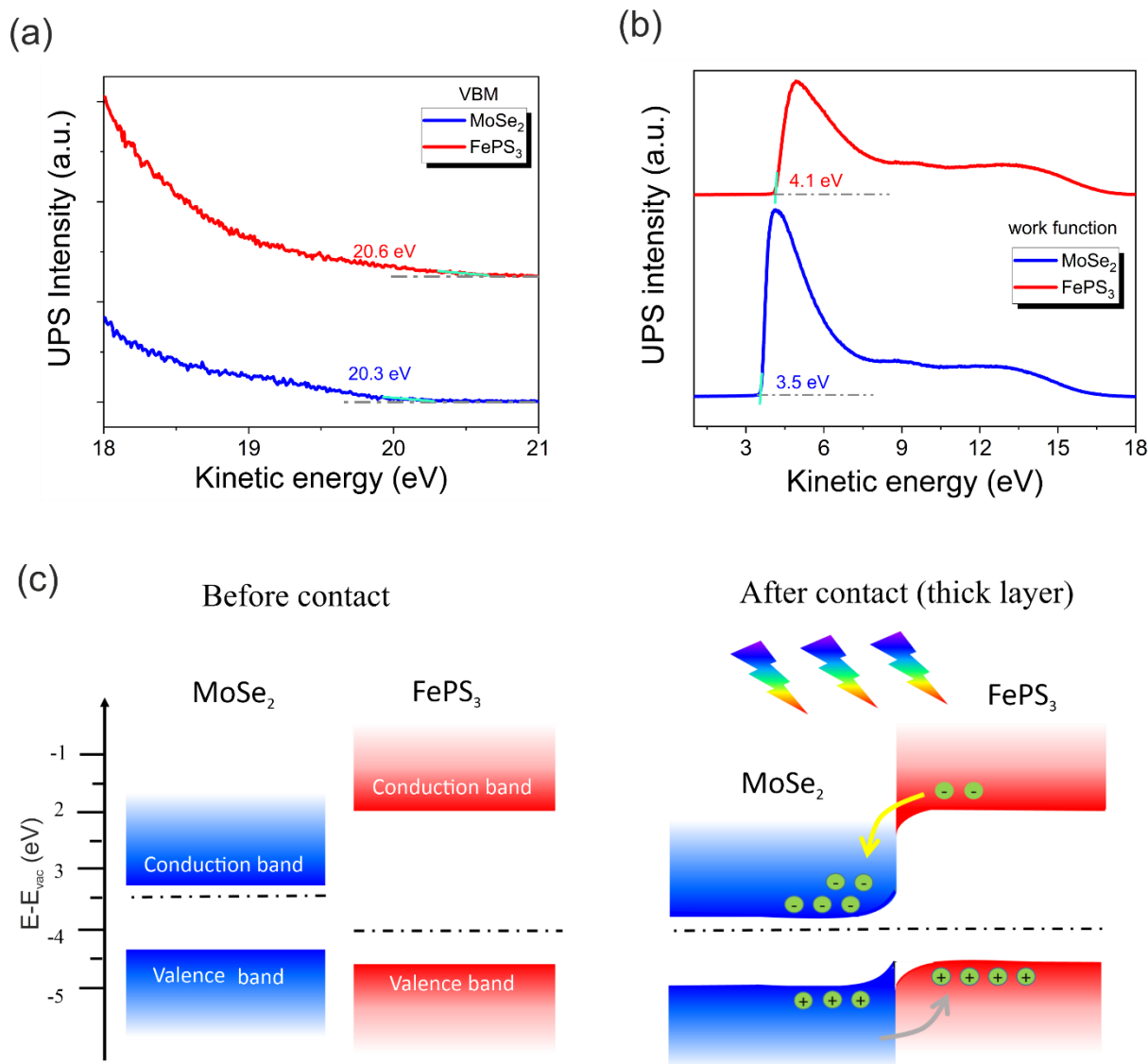
Figure 6-11. (a, b) UPS spectra of $MoSe_2$ and $FePS_3$. Kinetic-energy-axis near the secondary electron cut-off edge and the Fermi Edge correspond to the Φ and VBM, respectively. **(c)** Straddling Type II configuration for multilayer $MoSe_2/FePS_3$; The charge transfer processes is represented with arrows under illumination condition.

6.3.4 Thickness dependent $MoSe_2/FePS_3$ photodetectors

A series of $MoSe_2/FePS_3$ photodetectors with different thicknesses were fabricated and measured in order to gain a quantitative and comprehensive analysis about their optoelectronic properties. Figure 6-12 shows their calculated responsivity in mAW^{-1} at 532 nm at zero bias. It demonstrates a decrease trend of responsivity from 51 mA W^{-1} to 0.047 mA W^{-1} as the thickness of $MoSe_2/FePS_3$ decreases from 48/180 nm to 6/11 nm. This is mainly due to decreased absorption of $MoSe_2/FePS_3$ with decreasing the thicknesses of its constitution layers. Consequently, it decreases the concentration of photogenerated carriers and leads to a decreased

photoresponsivity. Moreover, by comparing device #2 and #3 we conclude that $MoSe_2$ plays a major role in determining the photoresponsivity contribution in the $MoSe_2/FePS_3$ photodetector. Additionally, a certain thickness of heterojunction is required for the strong built-in electric field in $MoSe_2/FePS_3$, which is the prerequisite for high efficiency hole/electron separation and high sensitivity photodetector. Since $MoSe_2$ (n-type) and $FePS_3$ (p-type) are not intentionally doped in our case, there is a high chance that the depletion region is not built completely when the thickness of $MoSe_2/FePS_3$ goes down to a few layers. It can cause low efficiency of hole/electron separation and may explain the extremely small responsivity value 0.047 mA W^{-1} for device #5.
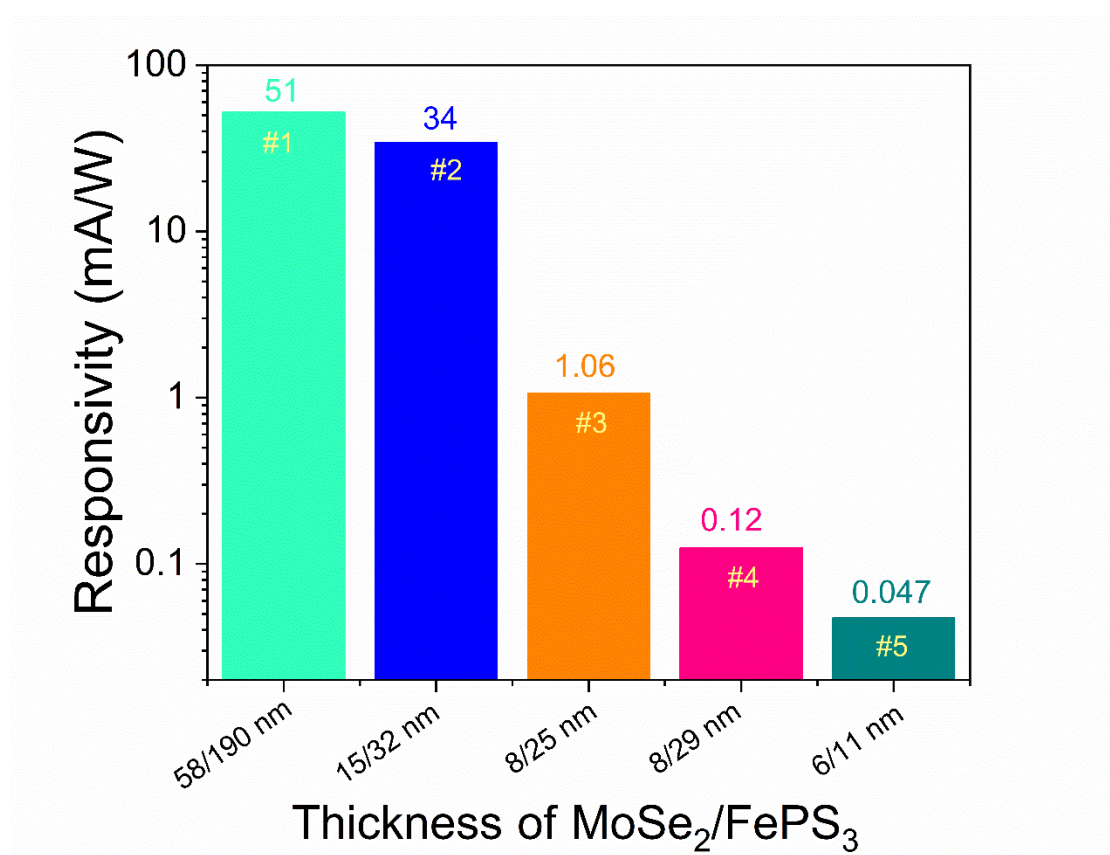
Figure 6-12. Thickness dependent responsivity of five different $MoSe_2/FePS_3$ photodetectors. All are operated in a photovoltaic mode.

6.4. Conclusions

In summary, we have performed a systematic study about the performance of $MoSe_2/FePS_3$ vdWHs photodetectors operated in the UV-vis-NIR spectral range. The fabricated self-powered multilayer n-p $MoSe_2/FePS_3$ photodetector is highly sensitive in the spectrum range from 350 to 900 nm. The maximum responsivity and external quantum efficiency estimated at 522 nm

and zero bias are as high as 52 mA W^{-1} and 12 %, respectively. The calculated detectivity at the same wavelength is as high as 1.4×10^{10} cm Hz$^{1/2}$ W^{-1}, which is superior to its individual TMDCs constituent and many other vdWH photodetectors. According to UPS measurements and DFT calculations, the excellence performance is owing to the type-II band alignment in the MoSe$_2$/FePS$_3$ vdWH. It implies that in general the proper MX$_2$/ MPX$_3$ vdWH is a sensitive self-driven photodetector from the UV to infrared range.

Chapter 7 Summary and outlook

7.1 Summary

The first part of this thesis focuses on the synthesis of heavily doped GaAs using ion implantation followed by non-equilibrium annealing processes. With this approach, the obtained electron and hole concentrations for GaAs:Te or GaAs:S and GaAs:Zn are as high as 7×10^{19} and 1.1×10^{20} cm^{-3}, respectively, which are well above the equilibrium solid solubility of those dopants in GaAs. The carrier concentrations are three orders of magnitude higher than the critical carrier concentration at room-temperature (1.6×10^{16} cm^{-3}) required for the insulator-metal transition (IMT) in GaAs. Thus, all heavily doped GaAs layers show metallic behaviour, as confirmed by temperature dependent resistance measurements. Importantly, Rutherford backscattering spectrometry and Raman spectroscopy results indicate that the heavily doped GaAs is well recrystallized after sub-second annealing.

In contrast to heavily doped Si or Ge, GaAs has a higher electron mobility, which makes heavily n-doped GaAs desirable for plasmonic applications. In this study, the plasma frequency of GaAs can be tuned from 1400 to 2700 cm^{-1} by increasing the electron concentration from 7.7×10^{18} to 7.6×10^{19} cm^{-3}. Numerically modeling with COMSOL based on n^{++} GaAs/intrinsic GaAs is built to study the plasmonic properties of GaAs. It is evident from the electric field distribution that there are two surface plasmon resonances. The first is originating from the electrical field enhancement at the n^{++} GaAs/air interfaces, while the second one is at the n^{++} GaAs/substrate interfaces. The simulation results suggest that n^{++} GaAs is promising for highly sensitivity plasmonic application in the mid-infrared range.

In addition, the n^{++} GaAs at low temperature and at low magnetic field (< 0.3 T) shows the negative magnetoresistance, which is due to the weak localization. By fitting the magneresistance with the Hikami-Larkin-Nagaoka (HLN) model, the phase coherence length ($l_{\emptyset}$) and spin-orbit length at 3 K are as large as 540 and 48 nm, respectively. $l_{\emptyset}$ is substantially longer than previously reported values in other semiconductors. This suggests that heavily doped GaAs could be a potential material for quantum devices and spintronic applications.

The second part of this thesis is about van der Waals heterostructure of MoSe$_2$/FePS$_3$. It is shown that the 1ML MoSe$_2$/FePS$_3$ shows a type-I band alignment, as verified by DFT calculations and photoluminescence (PL) measurements. 1ML MoSe$_2$ has a direct bandgap of 1.5 eV, while FePS$_3$ shows a quasi-direct bandgap of 2.2 eV. Consequently, during laser

excitation, the *p*-type FePS$_3$ donates carriers into MoSe$_2$. This results in a 20-fold enhancement of PL emission from the MoSe$_2$ monolayer. In addition, at low temperature (4 K), a significant enhancement of the trion emission with the trion/exciton intensity ratio increasing from 0.44 to 20 in MoSe$_2$/FePS$_3$ has been observed. Moreover, both the exciton emission in a single MoSe$_2$ monolayer and the trion emission in MoSe$_2$/FePS$_3$ depend on the chirality of the excitation light. This suggests that MoSe$_2$/FePS$_3$ with type-I band alignment is a promising candidate for valleytronic applications.

The band alignment of MoSe$_2$/FePS$_3$ can change from type-I to type-II by increasing the thickness of MoSe$_2$ from monolayer to multilayer. As the film thickness increases, MoSe$_2$ becomes an indirect band gap semiconductor and the band gap is reduced to 1.3 eV, which changes the band alignment between MoSe$_2$ and FePS$_3$. A built-in electric field can form in the multilayer MoSe$_2$/FePS$_3$ heterojunction since MoSe$_2$ is n-type semiconductor while FePS$_3$ is p-type. Such that, MoSe$_2$/FePS$_3$ can be used as an excellent candidate for a photodetector operating in a photovoltaic mode. In this study, the MoSe$_2$/FePS$_3$ photodetector is highly sensitive in the spectrum range from 350 to 900 nm. The maximum responsivity and external quantum efficiency at 522 nm and zero bias are as high as 52 mA W^{-1} and 12 %, respectively. The calculated detectivity for the same wavelength is as high as 1.4×10^{10} cm Hz$^{1/2}$ W^{-1}, which is superior to its individual TMDCs constituent and many other vdWH photodetectors.

7.2 Outlook

The COMSOL simulations presented in chapter 4 show that heavily doped GaAs has two surface plasma resonances. For plasmonic applications it is necessary to fabricate real antenna devices based on GaAs. Figure 7-1(a) shows the optical image of a GaAs antenna fabricated by electron beam lithography (EBL) patterning and reactive ion etching. This structure presents a dimer antenna with a 300 nm gap. The electric field in the gap can be significantly enhanced, which can increase the detection sensitivity. Figure 7-1(b) shows the SEM image of GaAs antenna covered with HSQ. GaAs samples with antennas will be investigated in a future study, and the parameters can be further optimized in order to get sharp edges of GaAs antennas.
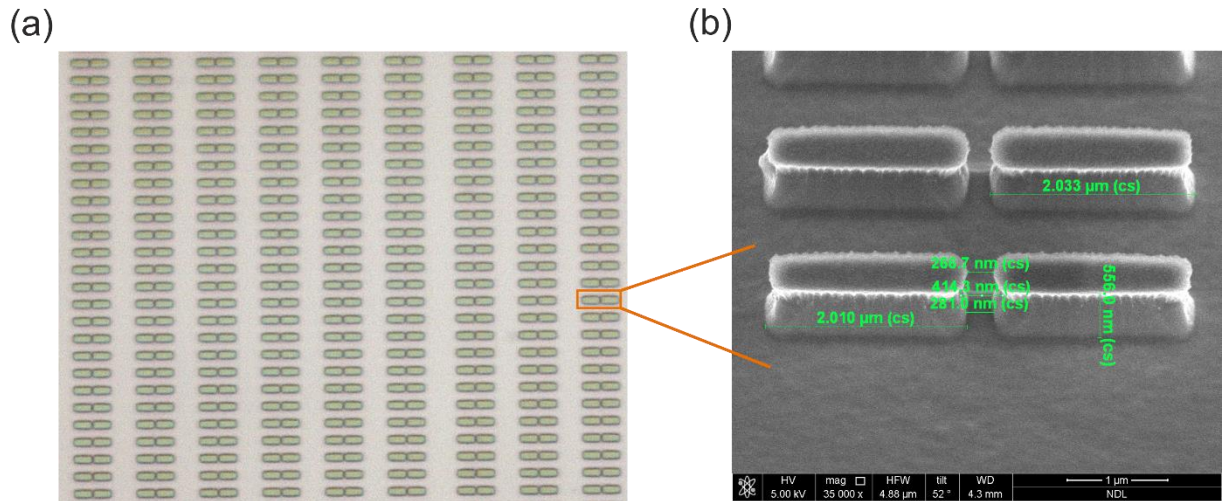
Figure 7-1. (a) Optical image of GaAs antennas after EBL patterning. **(b)** SEM image of GaAs antenna coved with HSQ after reactive etching.

For the heterostructure $MoSe_2/FePS_3$, the interlayer exciton and spin-valley dynamics can be studied by time-resolved PL measurements. The lifetime of excitons and trions can also be obtained by this method. This can provide the information about the decay mechanism in $MoSe_2$ and manifest how $FePS_3$ modifies the emission properties of $MoSe_2$. This will be important information for device application and fundamental research.

References

[1] K.F. Mak, K. He, C. Lee, G.H. Lee, J. Hone, T.F. Heinz, J. Shan, *Nat. Mater.* **12** (2013) 207-211.

[2] A. Splendiani, L. Sun, Y. Zhang, T. Li, J. Kim, C.-Y. Chim, G. Galli, F. Wang, *Nano Lett.* **10** (2010) 1271-1275.

[3] K.F. Mak, C. Lee, J. Hone, J. Shan, T.F. Heinz, *Phys. Rev. Lett.* **105** (2010) 136805.

[4] W. Zhao, Z. Ghorannevis, L. Chu, M. Toh, C. Kloc, P.-H. Tan, G. Eda, *ACS Nano* **7** (2013) 791-797.

[5] Y. Liu, N.O. Weiss, X. Duan, H.-C. Cheng, Y. Huang, X. Duan, *Nat. Rev. Mater.* **1** (2016) 16042.

[6] F. Xia, H. Wang, D. Xiao, M. Dubey, A. Ramasubramaniam, *Nat. Photonics* **8** (2014) 899-907.

[7] K. Novoselov, o.A. Mishchenko, o.A. Carvalho, A.C. Neto, *Science* **353** (2016).

[8] M.M. Furchi, F. Höller, L. Dobusch, D.K. Polyushkin, S. Schuler, T. Mueller, *npj 2D Mater. Appl.* **2** (2018) 3.

[9] F. Withers, O. Del Pozo-Zamudio, A. Mishchenko, A. Rooney, A. Gholinia, K. Watanabe, T. Taniguchi, S. Haigh, A. Geim, A. Tartakovskii, *Nat. Mater.* **14** (2015) 301-306.

[10] W. Wu, Q. Zhang, X. Zhou, L. Li, J. Su, F. Wang, T. Zhai, *Nano Energy* **51** (2018) 45-53.

[11] A. Boltasseva, H.A. Atwater, *Science* **331** (2011) 290-291.

[12] K.L. Kelly, E. Coronado, L.L. Zhao, G.C. Schatz, *J. Phys. Chem. B* **107** (2003), 668-677

[13] K. Yamagiwa, M. Shibuta, A. Nakajima, *ACS Nano* **14** (2020) 2044-2052.

[14] M. Rycenga, C.M. Cobley, J. Zeng, W. Li, C.H. Moran, Q. Zhang, D. Qin, Y. Xia, *Chem. Rev.* **111** (2011) 3669-3712.

[15] C.R. Yonzon, D.A. Stuart, X. Zhang, A.D. McFarland, C.L. Haynes, R.P. Van Duyne, *Talanta* **67** (2005) 438-448.

[16] A.J. Haes, L. Chang, W.L. Klein, R.P. Van Duyne, *J. Am. Chem. Soc.* **127** (2005) 2264-2271.

[17] W. Zhu, K.B. Crozier, *Nat. Commun.* **5** (2014) 3783.

[18] G.P. Kumar, *J. Nanophotonics* **6** (2012) 064503.

[19] S. Law, L. Yu, A. Rosenberg, D. Wasserman, *Nano Lett.* **13** (2013) 4569-4574.

[20] J.-M. Nam, C.S. Thaxton, C.A. Mirkin, *Science* **301** (2003) 1884-1886.

[21] M. Fehrenbacher, S. Winnerl, H. Schneider, J. Döring, S.C. Kehr, L.M. Eng, Y. Huo, O.G. Schmidt, K. Yao, Y. Liu, *Nano Lett.* **15** (2015) 1057-1061.

[22] S. Law, V. Podolskiy, D. Wasserman, *Nanophotonics* **2** (2013) 103-130.

[23] G.V. Naik, V.M. Shalaev, A. Boltasseva, *Adv. Mater.* **25** (2013) 3264-3294.

[24] L. Novotny, *Am. J. Phys.* **78** (2010) 1199-1202.

[25] X. Yang, Z. Sun, T. Low, H. Hu, X. Guo, F.J. García de Abajo, P. Avouris, Q. Dai, *Adv. Mater.* **30** (2018) 1704896.

[26] P.R. West, S. Ishii, G.V. Naik, N.K. Emani, V.M. Shalaev, A. Boltasseva, *Laser Photonics Rev.* **4** (2010) 795-808.

[27] J.C. Ginn, R.L. Jarecki Jr, E.A. Shaner, P.S. Davids, *J. Appl. Phys.* **110** (2011) 043110.

[28] L. Baldassarre, E. Sakat, J. Frigerio, A. Samarelli, K. Gallacher, E. Calandrini, G. Isella, D.J. Paul, M. Ortolani, P. Biagioni, *Nano Lett.* **15** (2015) 7225-7231.

[29] S. Law, D. Adams, A. Taylor, D. Wasserman, *Opt. Express* **20** (2012) 12155-12165.

[30] J. Neave, P. Dobson, J. Harris, P. Dawson, B. Joyce, *Appl. Phys. A* **32** (1983) 195-200.

[31] W. Walukiewicz, *Physica B Condens. Matter.* 302 (2001) 123-134.

[32] E.F. Schubert, Doping in III-V semiconductors, E. Fred Schubert, 2015.

[33] W. Walukiewicz, *Appl. Phys. Lett.* **54** (1989) 2094-2096.

[34] G. Baraff, M. Schlüter, *Phys. Rev. Lett.* **55** (1985) 1327.

[35] W. Walukiewicz, *J. Vac. Sci. Technol. B* **5** (1987) 1062-1067.

[36] S. Zhang, J.E. Northrup, *Phys. Rev. Lett.* **67** (1991) 2339.

[37] T. Yamada, E. Tokumitsu, K. Saito, T. Akatsuka, M. Miyauchi, M. Konagai, K. Takahashi, *J. Cryst. Growth.* **95** (1989) 145-149.

[38] S. Prucnal, F. Liu, M. Voelskow, L. Vines, L. Rebohle, D. Lang, Y. Berencén, S. Andric, R. Boettger, M. Helm, *Sci. Rep.* **6** (2016) 27643.

[39] M. Wang, A. Debernardi, Y. Berencén, R. Heller, C. Xu, Y. Yuan, Y. Xie, R. Böttger, L. Rebohle, W. Skorupa, *Phys. Rev. Appl.* **11** (2019) 054039.

[40] S. Zhou, F. Liu, S. Prucnal, K. Gao, M. Khalid, C. Baehtz, M. Posselt, W. Skorupa, M. Helm, *Sci. Rep.* **5** (2015) 8329.

[41] S. Prucnal, M.O. Liedke, X. Wang, M. Butterling, M. Posselt, J. Knoch, H. Windgassen, E. Hirschmann, Y. Berencén, L. Rebohle, *New J. Phys.* **22** (2020) 123036.

[42] D. Hurle, Proc. 6th Int. Symp. on GaAs and Related Compounds, *Inst. Phys. Conf. Series*, 33a, 1977.

[43] D. Hurle, *J. Appl. Phys.* **85** (1999) 6957-7022.

[44] J. Gebauer, E. Weber, N. Jäger, K. Urban, P. Ebert, *Appl. Phys. Lett.* **82** (2003) 2059-2061.

[45] J. Gebauer, R. Krause-Rehberg, C. Domke, P. Ebert, K. Urban, *Phys. Rev. Lett.* **78** (1997) 3334.

[46] J. Gebauer, R. Krause-Rehberg, S. Eichler, M. Luysberg, H. Sohn, E. Weber, *Appl. Phys. Lett.* **71** (1997) 638-640.

[47] J.E. Northrup, S. Zhang, *Phys. Rev. B* **47** (1993) 6791.

[48] A. Ferreira da Silva, I. Pepe, B.E. Sernelius, C. Persson, R. Ahuja, J. de Souza, Y. Suzuki, Y. Yang, *J. Appl. Phys.* **95** (2004) 2532-2535.

[49] N.F. Mott, *Rev. Mod. Phys.* **40** (1968) 677.

[50] M. Benzaquen, D. Walsh, K. Mazuruk, *Phys. Rev. B* **36** (1987) 4748.

[51] E. Burstein, *Phys. Rev.* **93** (1954) 632.

[52] J. Duan, M. Wang, L. Vines, R. Böttger, M. Helm, Y.J. Zeng, S. Zhou, S. Prucnal, *Phys. Status Solidi A* **216** (2019) 1800618.

[53] H.D. Chen, M.S. Feng, P.A. Chen, K.C. Lin, J.W. Wu, *Jpn. J. Appl. Phys* **33** (1994) 1920.

[54] M.K. Hudait, P. Modak, S. Hardikar, S. Krupanidhi, *J. Appl. Phys.* **82** (1997) 4931-4937.

[55] J. De-Sheng, Y. Makita, K. Ploog, H. Queisser, *J. Appl. Phys.* **53** (1982) 999-1006.

[56] P.A. Lee, T. Ramakrishnan, *Rev. Mod. Phys.* **57** (1985) 287.

[57] D. Saha, P. Misra, R. Ajimsha, M. Joshi, L. Kukreja, *Appl. Phys. Lett.* 105 (2014) 212102.

[58] E. Abrahams, 50 years of Anderson Localization, world scientific, 2010.

[59] M. Brahlek, N. Koirala, N. Bansal, S. Oh, *Solid State Commun.* **215** (2015) 54-62.

[60] S. Hikami, A.I. Larkin, Y. Nagaoka, *Prog. Theor. Phys.* **63** (1980) 707-710.

[61] A. Gilbertson, A. Newaz, W.-J. Chang, R. Bashir, S. Solin, L. Cohen, *Appl. Phys. Lett.* **95** (2009) 012113.

[62] J. Monsterleet, B. Capoen, G. Biskupski, *J. Phys. Condens. Matter.* **9** (1997) 8657.

[63] P. Newton, R. Mansell, S. Holmes, M. Myronov, C. Barnes, *Appl. Phys. Lett.* 110 (2017) 062101.

[64] E.M. Likovich, K.J. Russell, E.W. Petersen, V. Narayanamurti, *Phys. Rev. B* 80 (2009) 245318.

[65] V. Renard, I. Gornyi, O. Tkachenko, V. Tkachenko, Z. Kvon, E. Olshanetsky, A. Toropov, J.-C. Portal, *Phys. Rev. B* **72** (2005) 075313.

[66] J. Xu, M.K. Ma, M. Sultanov, Z.-L. Xiao, Y.-L. Wang, D. Jin, Y.-Y. Lyu, W. Zhang, L.N. Pfeiffer, K.W. West, *Nat. Commun.* **10** (2019) 287.

[67] M. Chhowalla, H.S. Shin, G. Eda, L.-J. Li, K.P. Loh, H. Zhang, *Nat. Chem.* **5** (2013) 263-275.

[68] J.D. Benck, T.R. Hellstern, J. Kibsgaard, P. Chakthranont, T.F. Jaramillo, *ACS Catal.* **4** (2014) 3957-3971.

[69] F. Bussolotti, H. Kawai, Z.E. Ooi, V. Chellappan, D. Thian, A.L.C. Pang, K.E.J. Goh, *Nano Futures* **2** (2018) 032001.

[70] K. Kośmider, J.W. González, J. Fernández-Rossier, *Phys. Rev. B* **88** (2013) 245436.

[71] Y. Cheng, Z. Zhu, M. Tahir, U. Schwingenschlögl, , *EPL (Europhysics Letters)* **102** (2013) 57001.

[72] G.-B. Liu, W.-Y. Shan, Y. Yao, W. Yao, D. Xiao, *Phys. Rev. B* **88** (2013) 085433.

[73] J.R. Schaibley, H. Yu, G. Clark, P. Rivera, J.S. Ross, K.L. Seyler, W. Yao, X. Xu, *Nat. Rev. Mater.*1 (2016) 16055.

[74] T. Olsen, S. Latini, F. Rasmussen, K.S. Thygesen, *Phys. Rev. Lett.* **116** (2016) 056401.

[75] J.S. Ross, S. Wu, H. Yu, N.J. Ghimire, A.M. Jones, G. Aivazian, J. Yan, D.G. Mandrus, D. Xiao, W. Yao, *Nat. Commun.* **4** (2013) 1474.

[76] J.-U. Lee, S. Lee, J.H. Ryoo, S. Kang, T.Y. Kim, P. Kim, C.-H. Park, J.-G. Park, H. Cheong, *Nano Lett.* **16** (2016) 7433-7438.

[77] R. Samal, G. Sanyal, B. Chakraborty, C.S. Rout, *J. Mater. Chem. A* **9** (2021) 2560-2591

[78] K.-z. Du, X.-z. Wang, Y. Liu, P. Hu, M.I.B. Utama, C.K. Gan, Q. Xiong, C. Kloc, *ACS Nano*. **10** (2016) 1738-1743.

[79] Y. Gao, S. Lei, T. Kang, L. Fei, C.-L. Mak, J. Yuan, M. Zhang, S. Li, Q. Bao, Z. Zeng, *Nanotechnology*. **29** (2018) 244001.

[80] J. Chu, F. Wang, L. Yin, L. Lei, C. Yan, F. Wang, Y. Wen, Z. Wang, C. Jiang, L. Feng, *Adv. Funct. Mater.* **27** (2017) 1701342.

[81] R. Kumar, R.N. Jenjeti, M.P. Austeria, S. Sampath, *J. Mater. Chem. C* **7** (2019) 324-329.

[82] X. Zhang, X. Zhao, D. Wu, Y. Jing, Z. Zhou, *Adv. Sci.* **3** (2016) 1600062.

[83] P. Joy, S. Vasudevan, *Phys. Rev. B* **46** (1992) 5425.

[84] K. Kim, S.Y. Lim, J.-U. Lee, S. Lee, T.Y. Kim, K. Park, G.S. Jeon, C.-H. Park, J.-G. Park, H. Cheong, *Nat. Commun.* 10 (2019) 354.

[85] Y.-J. Sun, Q.-H. Tan, X.-L. Liu, Y.-F. Gao, J. Zhang, *J. Phys. Chem*. **10** (2019) 3087-3093.

[86] A. McCreary, J.R. Simpson, T.T. Mai, R.D. McMichael, J.E. Douglas, N. Butch, C. Dennis, R.V. Aguilar, A.R.H. Walker, *Phys. Rev. B* **101** (2020) 064416.

[87] A.K. Geim, I.V. Grigorieva, *Nature* **499** (2013) 419-425.

[88] P. Rivera, J.R. Schaibley, A.M. Jones, J.S. Ross, S. Wu, G. Aivazian, P. Klement, K. Seyler, G. Clark, N.J. Ghimire, *Nat. Commun.* **6** (2015) 6242.

[89] P. Nagler, G. Plechinger, M.V. Ballottin, A. Mitioglu, S. Meier, N. Paradiso, C. Strunk, A. Chernikov, P.C. Christianen, C. Schüller, *2D Mater.* **4** (2017) 025112.

[90] M. Huang, S. Li, Z. Zhang, X. Xiong, X. Li, Y. Wu, *Nat. Nanotechnol.* **12** (2017) 1148-1154.

[91] S.J. Liang, B. Cheng, X. Cui, F. Miao, *Adv. Mater.* **32** (2020) 1903800.

[92] Z.I. Alferov, *Rev. Mod. Phys.* **73** (2001) 767.

[93] H. Kroemer, *Rev. Mod. Phys.* **73** (2001) 783.

[94] W. Zheng, B. Zheng, Y. Jiang, C. Yan, S. Chen, Y. Liu, X. Sun, C. Zhu, Z. Qi, T. Yang, *Nano Lett.* **19** (2019) 7217-7225.

[95] T. Yamaoka, H.E. Lim, S. Koirala, X. Wang, K. Shinokita, M. Maruyama, S. Okada, Y. Miyauchi, K. Matsuda, *Adv. Funct. Mater.* **28** (2018) 1801021.

[96] H. Cai, J. Kang, H. Sahin, B. Chen, A. Suslu, K. Wu, F. Peeters, X. Meng, S. Tongay, *Nanotechnology*. **27** (2016) 065203.

[97] B. Miller, A. Steinhoff, B. Pano, J. Klein, F. Jahnke, A. Holleitner, U. Wurstbauer, *Nano Lett.* **17** (2017) 5229-5237.

[98] P. Rivera, H. Yu, K.L. Seyler, N.P. Wilson, W. Yao, X. Xu, *Nat. Nanotechnol.* **13** (2018) 1004-1015.

[99] Y. Jiang, S. Chen, W. Zheng, B. Zheng, A. Pan, *Light Sci. Appl.* **10** (2021) 72.

[100] J.F. Ziegler, M.D. Ziegler, J.P. Biersack, *Nucl. Instrum. Methods Phys. Res. B* **268** (2010) 1818-1823.

[101] L. Rebohle, S. Prucnal, D. Reichel, Flash Lamp Annealing/From Basics to Applications, (2019).

[102] O. Philips'Gloeilampenfabrieken, *Philips Res. Rep.* **13** (1958) 1-9.

[103] D. Koon, C. Knickerbocker, *Rev. Sci. Instrum.* **63** (1992) 207-210.

[104] S.M. Sze, Semiconductor devices: physics and technology, John wiley & sons, 2008.

[105] G. Rietveld, C.V. Koijmans, L.C. Henderson, M.J. Hall, S. Harmon, P. Warnecke, B. Schumacher, *IEEE Trans Instrum Meas.* **52** (2003) 449-453.

[106] A.L. Patrick, T. Ramakrishnan, *Rev. Mod. Phys.* **57** (1985) 287-337.

[107] A. Kawabata, *J. Phys. Soc. Japan.* **49** (1980) 628-637.

[108] Q.-y. Ye, B. Shklovskii, A. Zrenner, F. Koch, K. Ploog, *Phys. Rev. B*. **41** (1990) 8477.

[109] J. Hansen, R. Taboryski, P. Lindelof, *Phys. Rev. B*. **47** (1993) 16040.

[110] B. Sernelius, K.-F. Berggren, *Phys. Rev. B* **19** (1979) 6390.

[111] C. Wolfe, G. Stillman, *Appl. Phys. Lett.* **27** (1975) 564-567.

[112] D. Deppe, N. Holonyak Jr, J. Baker, *Appl. Phys. Lett.* **52** (1988) 129-131.

[113] D. Hurle, *J. Phys. Chem. Solids* **40** (1979) 627-637.

[114] D. Szmyd, P. Porro, A. Majerfeld, S. Lagomarsino, *J. Appl. Phys.* **68** (1990) 2367-2375.

[115] D. Andrews, R. Heckingbottom, G. Davies, *J. Appl. Phys.* **54** (1983) 4421-4425.

[116] T. Haynes, W. Chu, T. Aselage, S. Picraux, *Appl. Phys. Lett.* **49** (1986) 666-668.

[117] I. Zardo, S. Conesa-Boj, F. Peiro, J. Morante, J. Arbiol, E. Uccelli, G. Abstreiter, A.F. i Morral, *Phys. Rev. B* **80** (2009) 245324.

[118] J. Steele, P. Puech, R.A. Lewis, *J. Appl. Phys.* **120** (2016) 055701.

[119] A. Mlayah, R. Carles, G. Landa, E. Bedel, A. Muñoz-Yagüe, *J. Appl. Phys.* **69** (1991) 4064-4070.

[120] W. Limmer, M. Glunk, S. Mascheck, A. Koeder, D. Klarer, W. Schoch, K. Thonke, R. Sauer, A. Waag, *Phys. Rev. B* **66** (2002) 205209.

[121] G. Irmer, M. Wenzel, J. Monecke, *Phys. Rev. B* **56** (1997) 9524.

[122] N.I. Goktas, E.M. Fiordaliso, R. LaPierre, *Nanotechnology* **29** (2018) 234001.

[123] M. Cada, D. Blazek, J. Pistora, K. Postava, P. Siroky, *Opt. Mater. Express* **5** (2015) 340-352.

[124] J. Steele, R. Lewis, M. Henini, O. Lemine, D. Fan, Y.I. Mazur, V. Dorogan, P. Grant, S.-Q. Yu, G. Salamo, *Opt. Express* **22** (2014) 11680-11689.

[125] C. Sönnichsen, T. Franzl, T. Wilk, G. von Plessen, J. Feldmann, O. Wilson, P. Mulvaney, *Phys. Rev. Lett.* **88** (2002) 077402.

[126] C. Sönnichsen, T. Franzl, T. Wilk, G. Von Plessen, J. Feldmann, *New J. Phys.* **4** (2002) 93.

[127] W. Lum, H. Wieder, *J. Appl. Phys.* **49** (1978) 6187-6188.

[128] H. Casey Jr, D. Sell, K. Wecht, *J. Appl. Phys.* **46** (1975) 250-257.

[129] I.P. Jacques, J. Pankove, Optical processes in semiconductors, by Prentice-Hall, New Jersey 92 (1971).

[130] J. Kundrotas, A. Čerškus, G. Valušis, M. Lachab, S. Khanna, P. Harrison, E. Linfield, *J. Appl. Phys.* **103** (2008) 123108.

[131] J. Kundrotas, A. Čerškus, S. Ašmontas, G. Valušis, B. Sherliker, M. Halsall, M. Steer, E. Johannessen, P. Harrison, *Phys. Rev. B* **72** (2005) 235322.

[132] J.I. Climente, C. Segarra, F. Rajadell, J. Planelles, *J. Appl. Phys.* **119** (2016) 125705.

[133] F. El-Mellouhi, N. Mousseau, *Phys. Rev. B* **71** (2005) 125207.

[134] T. Saso, T. Kasuya, *J. Phys. Soc. Japan.* **48** (1980) 1566-1575.

[135] O. Tufte, E. Stelzer, *Phys. Rev.* **139** (1965) A265.

[136] A. Chiquito, A. Lanfredi, E. Leite, *J. Phys. D. Appl. Phys.* **41** (2008) 045106.

[137] I. Mező, A. Dil, *J. Number Theory* **130** (2010) 360-369.

[138] Y.S. Kim, M. Brahlek, N. Bansal, E. Edrey, G.A. Kapilevich, K. Iida, M. Tanimura, Y. Horibe, S.-W. Cheong, S. Oh, *Phys. Rev. B* **84** (2011) 073109.

[139] A. Druzhinin, I. Ostrovskii, Y. Khoverko, N. Shcherban, A. Lukianchenko, *J. Magn. Magn. Mater.* **473** (2019) 331-334.

[140] M. Abramowitz, I.A. Stegun, R.H. Romer, *Am. J. Phys.* **56** (1988) 958.

[141] S. Thomas, D. Kim, S. Chung, T. Grant, Z. Fisk, J. Xia, *Phys. Rev. B* **94** (2016) 205114.

[142] S. Koester, K. Ismail, K. Lee, J. Chu, *Phys. Rev. B* **54** (1996) 10604.

[143] K. Premasiri, S.K. Radha, S. Sucharitakul, U.R. Kumar, R. Sankar, F.-C. Chou, Y.-T. Chen, X.P. Gao, *Nano Lett.* **18** (2018) 4403-4408.

[144] D. Liang, X.P. Gao, Strong tuning of Rashba spin–orbit interaction in single InAs nanowires, *Nano Lett.* **12** (2012) 3263-3267.

[145] D. Liang, M.R. Sakr, X.P. Gao, *Nano Lett.* **9** (2009) 1709-1712.

[146] R. Dzhioev, K. Kavokin, V. Korenev, M. Lazarev, B.Y. Meltser, M. Stepanova, B. Zakharchenya, D. Gammon, D. Katzer, *Phys. Rev. B* **66** (2002) 245204.

[147] R.J. Elliott, *Phys. Rev.* **96** (1954) 266.

[148] J. Kikkawa, D. Awschalom, *Phys. Rev. Lett.* **80** (1998) 4313.

[149] A.M. Jones, H. Yu, N.J. Ghimire, S. Wu, G. Aivazian, J.S. Ross, B. Zhao, J. Yan, D.G. Mandrus, D. Xiao, *Nat. Nanotechnol.* **8** (2013) 634-638.

[150] A. Singh, G. Moody, K. Tran, M.E. Scott, V. Overbeck, G. Berghäuser, J. Schaibley, E.J. Seifert, D. Pleskot, N.M. Gabor, *Phys. Rev. B* **93** (2016) 041401.

[151] K.F. Mak, K. He, J. Shan, T.F. Heinz, *Nat. Nanotechnol.* **7** (2012) 494-498.

[152] F. Ceballos, M.Z. Bellus, H.-Y. Chiu, H. Zhao, *ACS Nano* **8** (2014) 12717-12724.

[153] X. Hong, J. Kim, S.-F. Shi, Y. Zhang, C. Jin, Y. Sun, S. Tongay, J. Wu, Y. Zhang, F. Wang, *Nat. Nanotechnol.* **9** (2014) 682-686.

[154] Y. Yu, S. Hu, L. Su, L. Huang, Y. Liu, Z. Jin, A.A. Purezky, D.B. Geohegan, K.W. Kim, Y. Zhang, *Nano Lett.* **15** (2015) 486-491.

[155] M.-H. Chiu, M.-Y. Li, W. Zhang, W.-T. Hsu, W.-H. Chang, M. Terrones, H. Terrones, L.-J. Li, *ACS Nano* **8** (2014) 9649-9656.

[156] T. Roy, M. Tosun, X. Cao, H. Fang, D.-H. Lien, P. Zhao, Y.-Z. Chen, Y.-L. Chueh, J. Guo, A. Javey, *ACS Nano.* **9** (2015) 2071-2079.

[157] F. Ceballos, M.Z. Bellus, H.-Y. Chiu, H. Zhao, *Nanoscale* **7** (2015) 17523-17528.

[158] W.-T. Hsu, Z.-A. Zhao, L.-J. Li, C.-H. Chen, M.-H. Chiu, P.-S. Chang, Y.-C. Chou, W.-H. Chang, *ACS Nano* **8** (2014) 2951-2958.

[159] M.Z. Bellus, M. Li, S.D. Lane, F. Ceballos, Q. Cui, X.C. Zeng, H. Zhao, *Nanoscale Horiz.* **2** (2017) 31-36.

[160] Y.H. Zhou, Z.B. Zhang, P. Xu, H. Zhang, B. Wang, *Nanoscale Res. Lett.* **14** (2019) 364.

[161] J.J. Carmiggelt, M. Borst, T. van der Sar, *Sci. Rep.* **10** (2020) 1-7.

[162] G.D. Shepard, J.V. Ardelean, O.A. Ajayi, D. Rhodes, X. Zhu, J.C. Hone, S. Strauf, *ACS Nano* **11** (2017) 11550-11558.

[163] M. Velický, P.S. Toth, *Appl. Mater. Today* **8** (2017) 68-103.

[164] G. Kresse, J. Hafner, *Phys. Rev. B* **47** (1993) 558.

[165] J.P. Perdew, K. Burke, M. Ernzerhof, *Phys. Rev. Lett.* **77** (1996) 3865.

[166] S. Grimme, *J. Comput. Chem.* **27** (2006) 1787-1799.

[167] P. Tonndorf, R. Schmidt, P. Böttger, X. Zhang, J. Börner, A. Liebig, M. Albrecht, C. Kloc, O. Gordan, D.R. Zahn, *Opt. Express* **21** (2013) 4908-4916.

[168] D. Nam, J.-U. Lee, H. Cheong, *Sci. Rep.* **5** (2015) 17113.

[169] X. Wang, K. Du, Y.Y.F. Liu, P. Hu, J. Zhang, Q. Zhang, M.H.S. Owen, X. Lu, C.K. Gan, P. Sengupta, *2D Mater.* **3** (2016) 031009.

[170] T. Björkman, A. Gulans, A.V. Krasheninnikov, R.M. Nieminen, *Phys. Rev. Lett.* **108** (2012) 235502.

[171] Z. Cheng, T.A. Shifa, F. Wang, Y. Gao, P. He, K. Zhang, C. Jiang, Q. Liu, J. He, *Adv. Mater.* **30** (2018) 1707433.

[172] J. Wierzbowski, J. Klein, F. Sigger, C. Straubinger, M. Kremser, T. Taniguchi, K. Watanabe, U. Wurstbauer, A.W. Holleitner, M. Kaniber, *Sci. Rep.* **7** (2017) 12383.

[173] B. Zheng, W. Zheng, Y. Jiang, S. Chen, D. Li, C. Ma, X. Wang, W. Huang, X. Zhang, H. Liu, *J. Am. Chem. Soc.* **141** (2019) 11754-11758.

[174] X. Wang, Y. Gong, G. Shi, W.L. Chow, K. Keyshar, G. Ye, R. Vajtai, J. Lou, Z. Liu, E. Ringe, *ACS Nano* **8** (2014) 5125-5131.

[175] D. Sercombe, S. Schwarz, O. Del Pozo-Zamudio, F. Liu, B. Robinson, E. Chekhovich, I. Tartakovskii, O. Kolosov, A. Tartakovskii, *Sci. Rep.* **3** (2013) 3489.

[176] W. Zheng, B. Zheng, C. Yan, Y. Liu, X. Sun, Z. Qi, T. Yang, Y. Jiang, W. Huang, P. Fan, *Adv. Sci.* **6** (2019) 1802204.

[177] X. Zong, H. Hu, G. Ouyang, J. Wang, R. Shi, L. Zhang, Q. Zeng, C. Zhu, S. Chen, C. Cheng, *Light Sci. Appl.* **9** (2020) 114.

[178] R. Cheng, D. Li, H. Zhou, C. Wang, A. Yin, S. Jiang, Y. Liu, Y. Chen, Y. Huang, X. Duan, *Nano Lett.* **14** (2014) 5590-5597.

[179] M. Van der Donck, F. Peeters, *Phys. Rev. B* **98** (2018) 115104.

[180] K. Dolui, I. Rungger, S. Sanvito, *Phys. Rev. B* **87** (2013) 165402.

[181] A. Singh, A.K. Singh, *Phys. Rev. B* **99** (2019) 121201.

[182] H.-P. Komsa, J. Kotakoski, S. Kurasch, O. Lehtinen, U. Kaiser, A.V. Krasheninnikov, *Phys. Rev. Lett.* **109** (2012) 035503.

[183] J. Siviniant, D. Scalbert, A. Kavokin, D. Coquillat, J. Lascaray, *Phys. Rev. B* **59** (1999) 1602.

[184] N. Peimyoo, W. Yang, J. Shang, X. Shen, Y. Wang, T. Yu, *ACS Nano* **8** (2014) 11320-11329.

[185] R. Suzuki, M. Sakano, Y. Zhang, R. Akashi, D. Morikawa, A. Harasawa, K. Yaji, K. Kuroda, K. Miyamoto, T. Okuda, *Nat. Nanotechnol.* **9** (2014) 611.

[186] T. Cao, G. Wang, W. Han, H. Ye, C. Zhu, J. Shi, Q. Niu, P. Tan, E. Wang, B. Liu, *Nat. Commun.* **3** (2012) 887.

[187] H. Zeng, J. Dai, W. Yao, D. Xiao, X. Cui, *Nat. nanotechnol.* **7** (2012) 490-493.

[188] D. Zhang, Y. Liu, M. He, A. Zhang, S. Chen, Q. Tong, L. Huang, Z. Zhou, W. Zheng, M. Chen, *Nat. Nanotechnol.* **11** (2020) 4442.

[189] R. Mas-Balleste, C. Gomez-Navarro, J. Gomez-Herrero, F. Zamora, *Nanoscale* **3** (2011) 20-30.

[190] K. Kim, S.Y. Lim, J. Kim, J.-U. Lee, S. Lee, P. Kim, K. Park, S. Son, C.-H. Park, J.-G. Park, *2D Mater.* **6** (2019) 041001.

[191] E.C. Ahn, 2D materials for spintronic devices, *npj 2D Mater. Appl.* **4** (2020) 17.

[192] H. Li, S. Ruan, Y.J. Zeng, *Adv. Mater.* **31** (2019) 1900065.

[193] F. Wang, T.A. Shifa, P. Yu, P. He, Y. Liu, F. Wang, Z. Wang, X. Zhan, X. Lou, F. Xia, *Adv. Funct. Mater.* **28** (2018) 1802151.

[194] M. Birowska, P.E.F. Junior, J. Fabian, J. Kunstmann, arXiv preprint arXiv:2009.05030, (2020).

[195] M. Ramos, F. Carrascoso, R. Frisenda, P. Gant, S. Mañas-Valero, D.L. Esteras, J.J. Baldoví, E. Coronado, A. Castellanos-Gomez, M.R. Calvo, *npj 2D Mater. Appl.* **5** (2021) 19.

[196] M. Onga, Y. Sugita, T. Ideue, Y. Nakagawa, R. Suzuki, Y. Motome, Y. Iwasa, *Nano Lett.* **20** (2020) 4625-4630.

[197] S.M. Sze, K.K. Ng, Physics of semiconductor devices, John wiley & sons, 2006.

[198] O. Breitenstein, P. Altermatt, K. Ramspeck, A. Schenk, *Proceedings of the 21st European photovoltaic solar energy conference*, Citeseer, 2006, pp. 625-628.

[199] M. Brötzmann, U. Vetter, H. Hofsäss, *J. Appl. Phys.* **106** (2009) 063704.

[200] H.S. Lee, J. Ahn, W. Shim, S. Im, D.K. Hwang, *Appl. Phys. Lett.* **113** (2018) 163102.

[201] Q. Zhao, W. Wang, F. Carrascoso-Plana, W. Jie, T. Wang, A. Castellanos-Gomez, R. Frisenda, *Mater. Horiz.* **7** (2020) 252-262.

[202] J. Xia, X. Huang, L.-Z. Liu, M. Wang, L. Wang, B. Huang, D.-D. Zhu, J.-J. Li, C.-Z. Gu, X.-M. Meng, *Nanoscale* **6** (2014) 8949-8955.

[203] X. Li, M.-W. Lin, J. Lin, B. Huang, A.A. Puretzky, C. Ma, K. Wang, W. Zhou, S.T. Pantelides, M. Chi, *Adv. Sci.* **2** (2016) e1501882.

[204] B. Liu, C. Zhao, X. Chen, L. Zhang, Y. Li, H. Yan, Y. Zhang, *Superlattices. Microstruct.* **130** (2019) 87-92.

[205] X. Chen, F. Ren, S. Gu, J. Ye, *Photonics. Res.* **7** (2019) 381-415.

[206] L. Ye, H. Li, Z. Chen, J. Xu, *ACS Photonics* **3** (2016) 692-699.

[207] K. Zhang, M. Peng, W. Wu, J. Guo, G. Gao, Y. Liu, J. Kou, R. Wen, Y. Lei, A. Yu, *Mater. Horiz.* **4** (2017) 274-280.

[208] R. Kumar, A. Sharma, M. Kaur, S. Husale, *Adv. Opt. Mater.* **5** (2017) 1700009.

[209] M. Long, A. Gao, P. Wang, H. Xia, C. Ott, C. Pan, Y. Fu, E. Liu, X. Chen, W. Lu, *Sci. Adv.* **3** (2017) e1700589.

[210] A. Islam, J. Lee, P.X.-L. Feng, *ACS Photonics* **5** (2018) 2693-2700.

[211] L. Meng, Y. Li, B. Yao, Z. Ding, G. Yang, R. Liu, R. Deng, L. Liu, *J. Appl. Phys.* **120** (2016) 235306.

[212] J. Tauc, R. Grigorovici, A. Vancu, *Phys. Status Solidi B* **15** (1966) 627-637.

[213] J. Quereda, T.S. Ghiasi, F.A. van Zwol, C.H. van der Wal, B.J. van Wees, *2D Mater.* **5** (2017) 015004.

[214] J. Duan, P. Chava, M. Ghorbani-Asl, D. Erb, L. Hu, A.V. Krasheninnikov, H. Schneider, L. Rebohle, A. Erbe, M. Helm, Y.J. Zeng, S. Zhou, S. Prucnal, *Adv. Funct. Mater.* (2021) 2104960.

Acknowledgements

Juanmei Duan

Appendix A: Publication list

[1] ***J. M. Duan***, P. Chava, M. Ghorbani-Asl, D. Erb, L. Hu, A. V. Krasheninnikov, H. Schneider, L. Rebohle, A. Erbe, M. Helm, Y. J. Zeng, S. Q. Zhou and S. Prucnal, Enhanced trion emission in monolayer MoSe$_2$ by constructing a type-I van der Waals heterostructure, *Adv. Funct. Mater.* 31.40 (2021): 2104960

[2] ***J. M. Duan***, P. Chava, M. Ghorbani-Asl, Y. F. Lu, D. Erb, L. Hu, A. Echresh, L. Rebohle, A. Erbe, A. V. Krasheninnikov, M. Helm, Y. J. Zeng, S. Q. Zhou and S. Prucnal, Self-driven broadband photodetector based on MoSe$_2$/FePS$_3$ van der Waals p-n Type II heterostructures (submitted to *ACS Appl. Mater. Interfaces*)

[3] ***J. M. Duan***, C.A Wang, L. Vines, L. Rebohle, M. Helm, Y. J. Zeng, S. Q. Zhou and S. Prucnal, Increased dephasing length in heavily doped GaAs, *New. J. Phys.* 23.8 (2021): 083034.

[4] ***J. M. Duan***, Q. Liu, W. C. Wu, L. Rebohle, Y. H. Lu, Y. J. Zeng, M. Helm, S. Q. Zhou and S. Prucnal, Mid-infrared plasmonics in heavily doped GaAs (under preparation)

[5] ***J. M. Duan***, M. Wang, L. Vines, R. Böttger, M. Helm, Y. J. Zeng, S. Q. Zhou and S. Prucnal, Formation and Characterization of Shallow Junctions in GaAs Made by Ion Implantation and ms-Range Flash Lamp Annealing, *Phys. Status Solidi A* 216.8 (2019): 1800618.

[6] S. Prucnal, A. Hashemi, M. Ghorbani-Asl, R. Hübner, ***J. M. Duan***, Y. D. Wei, D. Sharma, D. R. T. Zahn, R. Ziegenrücker, U. Kentsch, A. V. Krasheninnikov, M. Helm, S. Q. Zhou, Chlorine doping of MoSe$_2$ flakes by ion implantation, *Nanoscale* 13.11 (2021): 5834-5846.

[7] L. Hu, L. Cao, L. W. Li, ***J. M. Duan***, X.Q. Liao, F.C. Long, J. Zhou, Y.G Xiao, Y. J. Zeng, S. Q. Zhou, Two-dimensional magneto-photoconductivity in non-van der Waals manganese selenide, *Mater. Horiz.* 8.4 (2021): 1286-1296.

[8] C. A. Wang, H. B. Zhang, K. Deepak, C. Chen, A. Foucht, ***J. M. Duan***, D. Hilliard, U. Kentsch, D. Y. Chen, M. Zeng, X.S. Gao, Y-J. Zeng, M. Helm, W. Prellier, and S. Q. Zhou, Tuning the metal-insulator transition in epitaxial SrVO$_3$ films by uniaxial strain, *Phys. Rev. Materials* 3.11 (2019): 115001.

[9] S. Prucnal, J. Zuk, R. Hübner, ***J. M. Duan***, M.Wang, K. Pyszniak, A. Drozdziel, M. Turek and S. Q. Zhou, Electron Concentration Limit in Ge Doped by Ion Implantation and Flash Lamp Annealing, *Materials* 13.6 (2020): 1408.

Appendix B: Curriculum Vitae

Personal data

Name: Juanmei Duan

Date of birth: 21. Feb. 1992

Place of birth: Shaanxi, China

Family status: single

Education

Sep. 2010 - Jul. 2014	Bachelor of Engineering
	Xi'an University of Architecture and Technology, China
Sep. 2013 - Jul. 2016	Master of Science
	Shanghai University, China
Oct. 2016 - Mar. 2020	Ph.D. student
	Helmholtz-Zentrum Dresden-Rossendorf, Germany
	Technische Universität Dresden, Germany

Teaching

Apr. 2020 - Jul. 2021	Teaching assistant
	Technische Universität Dresden, Germany
	Lecture: Laboratory of Fundamental Physics

Erklärung

Hiermit versichere ich, dass ich die vorliegende Arbeit ohne unzulässige Hilfe Dritter und ohne Benutzung anderer als der angegebenen Hilfsmittel angefertigt habe; die aus fremden Quellen direkt oder indirekt übernommenen Gedanken sind als solche kenntlich gemacht. Die Arbeit wurde bisher weder im Inland noch im Ausland in gleicher oder ähnlicher Form einer anderen Prüfungsbehörde vorgelegt.

Diese Dissertation wurde angefertigt im

Helmholtz-Zentrum Dresden-Rossendorf

Institut für Ionenstrahlphysik und Materialforschung

Bautzner Landstr. 400, 01328 Dresden

Die wissenschaftliche Betreuung der Arbeit erfolgte durch Prof. Dr. Manfred Helm.

Ich versichere, an keiner Institution, auch nicht im Ausland, jemals den Antrag auf Erüffnung eines Promotionsverfahrens gestellt zu haben.

Ich erkenne die Promotionsordnung der Fakultät Mathematik und Naturwissenschaften der Technischen Universität Dresden an.

Juanmei Duan

02/08/2020